



Skolkovo Institute of Science and Technology

PHOTON CORRELATIONS OF OPTICALLY TRAPPED POLARITON  
CONDENSATE

*Doctoral Thesis*

by

STEPAN BARYSHEV

DOCTORAL PROGRAM IN PHYSICS

Supervisor  
Professor Pavlos Lagoudakis  
Co-Supervisor  
Dr. Anton Zasedatelev

Moscow - 2022

© Baryshev Stepan 2022

I hereby declare that the work presented in this thesis was carried out by myself at Skolkovo Institute of Science and Technology, Moscow, except where due acknowledgement is made, and has not been submitted for any other degree.

Candidate (Stepan Baryshev)

Supervisor (Prof. Pavlos Lagoudakis)

Co-Supervisor (Dr. Anton Zasedatelev)

## Abstract

Monatomic linear carbon chains, stabilized by gold nanoparticles attached to their ends and deposited on a solid substrate, were studied. Spectral features of straight chains containing from 8 to 24 atoms were observed. Low-temperature PL spectra revealed characteristic triplet fine structures that repeat themselves for carbon chains of different lengths. The triplet is invariably composed of a sharp intense peak accompanied by two broader satellites situated 15 and 40 meV below the main peak, interpreted as resonances for an edge-state neutral exciton and, positively and negatively charged trions, respectively. The time-resolved PL shows that the radiative lifetime of the observed quasiparticles is about 1 ns, and it increases with the increase of the length of the chain.

At high temperatures a nonradiative exciton decay channel appears due to the thermal hopping of carriers between parallel carbon chains. Whilst structural traits of the structure would suggest the quantum nature the emission, no visible photon antibunchings were observed during the investigation of the second-order coherence function. However, the laid groundwork has allowed for full polarization tomography of photon correlations in a spinor trapped exciton-polariton condensates. Conducted measurements revealed condensate pseudospin mean-field dynamics spanning from stochastic switching between linear polarization components, limit cycles, and stable fixed points and their intrinsic relation to the condensate photon statistics. During experiments we optically harness the cavity birefringence, polariton interactions, and the optical orientation of an incoherent exciton reservoir to engineer photon statistics with precise control. The results shown in this dissertation demonstrate a smooth transition from a highly coherent to a super-thermal state of the condensate polarization components.

Looking further into photon statistical properties, the Hong-Ou-Mandel effect in optically trapped polariton condensate was studied in the trap ground state. The magnitude of the HOM effect for a circularly polarized condensate above threshold was revealed to be significantly lower compared to what is known for a single mode classical coherent light source. The two photon interference appeared to be affecting the intensity correlation function of the light with super-bunched photon statistics more strongly than the correlation function of the light with Poissonian photon statistics. Moreover, in the limit cycle regime of condensate pseudospin precession, the revival of the Hong-Ou-Mandel effect was shown.

# Publications

## Main author

1. S. Baryshev, A. Zasedatelev, H. Sigurdsson, I. Gnusov, J. D. Töpfer, A. Askitopoulos, and P. G. Lagoudakis, “Engineering photon statistics in a spinor polariton condensate,” *Phys. Rev. Lett.*, vol. 128, p. 087402, Feb 2022

## Co-author

1. I. Gnusov, H. Sigurdsson, J. Töpfer, S. Baryshev, S. Alyatkin, and P. Lagoudakis, “All-optical linear-polarization engineering in single and coupled exciton-polariton condensates,” *Phys. Rev. Applied*, vol. 16, p. 034014, Sep 2021
2. S. Kutrovsкая, S. Demirchyan, A. Osipov, S. Baryshev, A. Zasedatelev, P. Lagoudakis, and A. Kavokin, “Exciton energy spectra in polyne chains,” *Phys. Rev. Research*, vol. 3, p. 013071, Jan 2021
3. S. Kutrovsкая, A. Osipov, S. Baryshev, A. Zasedatelev, V. Samyshkin, S. Demirchyan, O. Pulci, D. Grassano, L. Gontrani, R. R. Hartmann, M. E. Portnoi, A. Kucherik, P. G. Lagoudakis, and A. Kavokin, “Excitonic fine structure in emission of linear carbon chains,” *Nano Letters*, vol. 20, no. 9, pp. 6502–6509, 2020. PMID: 32787174
4. S. Kutrovsкая, S. Demirchyan, A. Osipov, S. Baryshev, A. Zasedatelev, P. Lagoudakis, and A. Kavokin, “Exciton radiative lifetime in a monoatomic carbon chain,” *New Journal of Physics*, vol. 23, p. 033007, mar 2021
5. I. Gnusov, H. Sigurdsson, S. Baryshev, A. Askitopoulos, and P. G. Lagoudakis, “Pseudo-spin destabilization in optically confined exciton-polariton condensates,” in *Frontiers in Optics / Laser Science*, p. FTu2D.4, Optica Publishing Group, 2020
6. I. Gnusov, H. Sigurdsson, S. Baryshev, T. Ermatov, A. Askitopoulos, and P. G. Lagoudakis, “Optical orientation, polarization pinning, and depolarization dy-

namics in optically confined polariton condensates,” *Phys. Rev. B*, vol. 102,  
p. 125419, Sep 2020

*Dedicated to my parents.*

I would like to thank following people without whom I would not have been able to finish my PhD. Anton Baranikov, Timur Yagafarov and Timur Ermatov who were pioneering senior students in this laboratory, who with their guiding light corrected my course as a student. Thank you to Ivan Gnusov with whom we conducted variety of experiments and shared good time on our experimental setup. Kirill Sitnik with whom we spent days and nights in the laboratory perfecting our measurements and stressing about every bump on our road to PhD. Anton Putintsev who was always open to any scientific discussion and finishing opened snacks. To Sergey Alyatkin for his wise advises about the experimental techniques and discussion of the physics we observed, as well as for timely injections of coffee into my bloodstream. Alexis Askitopoulos for the discussion and advises on the experiments. Anton Zasedatelev who kick started my work in the laboratory giving maxim knowledge within limited time we worked together, while remaining patient with my missteps. Special thanks to Tamsin Cookson for her patience and great expertise while working with me on the setup and especially when reading through this thesis and correcting errors. To every member of our groups in Skoltech and Southampton for the discussion and help throughout my PhD and the moments we shared outside the working hours. Great thank you to Pavlos Lagoudakis without whom none of this would be possible for the opportunity to work in such a great laboratory with brilliant people. To my parents, my mom who supported me along this journey with her worldly wisdom, and my dad who was a listener for my scientific rants. To my beloved Viktoria who was understanding and supportive throughout this time. Without you this would not be possible and without you i would not be able to pursue to dream of a scientist.

---

## Glossary

**AOM** Acousto optic modulator  
**BEC** Bose Einstein condensate  
**BS** Beam splitter  
**CW** Continuous wave  
**DBR** Distributed Bragg reflector  
**HBT** Hanbury Brwon and Twiss  
**HOM** Hong Ou and Mandel  
**HWP** Half waveplate  
**FWHM** Full width at half maximum  
**LPB** Lower polariton branch  
**PBS** Polarizing beam splitter  
**PL** Photoluminescence  
**QW** Quantum well  
**QWP** Quarter waveplate  
**SLM** Spatial light modulator  
**TCSPC** Time-correlated single photon counting  
**TRPL** Time-resolved photoluminescence  
**UPB** Upper polariton branch  
**VCSEL** Vertical-cavity surface-emitting laser

# Contents

<b>1</b>	<b>Introduction</b>	<b>13</b>
<b>2</b>	<b>TCSPC of linear carbon chains emission</b>	<b>18</b>
2.1	TCSPC technique . . . . .	19
2.2	Polyynes chains sample . . . . .	20
2.3	Spectral and temporal characteristics . . . . .	22
2.3.1	Conclusion . . . . .	26
<b>3</b>	<b>Polaritons In Semiconductor Microcavities</b>	<b>28</b>
3.1	Coupling of light and matter . . . . .	29
3.1.1	DBR . . . . .	29
3.1.2	Cavity . . . . .	30
3.1.3	Excitons in quantum wells . . . . .	32
3.1.4	Strong coupling and exciton-polaritons . . . . .	34
3.2	Condensation of exciton-polaritons . . . . .	38
3.2.1	Mechanism of polariton condensation . . . . .	39
3.2.2	Confinement of polariton condensates . . . . .	40
3.2.3	Polarization of polariton condensate . . . . .	41
3.3	Experimental methods . . . . .	43
3.3.1	Sample . . . . .	44
3.3.2	Experimental setup . . . . .	44
3.3.3	Integrating polarimetry . . . . .	48
<b>4</b>	<b>Hanbury Brown and Twiss effect</b>	<b>50</b>
4.1	Theory of optical coherence . . . . .	51
4.1.1	Semiclassical theory . . . . .	51
4.1.2	Non-classical photon statistics . . . . .	53
4.2	Second-order correlation of condensate . . . . .	54
4.2.1	Hanbury-Brown and Twiss interferometry of trapped polariton condensate . . . . .	57
4.2.2	Pseudospin projection photon bunching . . . . .	59
4.2.3	Self-induced Larmor precession . . . . .	63
4.2.4	Polarization switching and pinning . . . . .	67
4.2.5	Dynamical mean field equations . . . . .	69
4.2.6	Influence of residual ellipticity . . . . .	73
4.2.7	Single mode laser vs Polariton condensate . . . . .	74
4.2.8	Effect of the trap geometry . . . . .	74

4.2.9	The correlation function decay curve . . . . .	75
4.2.10	Conclusion . . . . .	78
<b>5</b>	<b>Hong-Ou-Mandel effect</b>	<b>79</b>
5.1	Theory of Hong-Ou-Mandel effect . . . . .	80
5.1.1	Beam splitter action . . . . .	80
5.1.2	Two-photon interference . . . . .	81
5.1.3	HOM of non-classical and classical light . . . . .	82
5.2	Experimental results . . . . .	83
5.2.1	Laser HOM effect . . . . .	84
5.2.2	Condensate HOM effect . . . . .	87
5.2.3	Conclusion . . . . .	93
<b>6</b>	<b>Concluding Remarks And Future Perspectives</b>	<b>94</b>
	<b>Bibliography</b>	<b>96</b>

# List of Figures

2-1	TCSPC resolution . . . . .	20
2-2	Deposition of nanoparticle stabilized carbon chains . . . . .	23
2-3	PL spectra of the deposited polyynes of different lengths . . . . .	24
2-4	Time-resolved photoluminescence (TRPL) data. . . . .	25
2-5	Time-resolved photoluminescence (TRPL) data and theoretical modeling comparison. . . . .	26
3-1	Periodically patterned two-dimensional layers for use as a dielectric mirror . . . . .	30
3-2	Photonic cavity formed by parallel alignment of two DBR mirrors. . . . .	31
3-3	Strong coupling of photon and QW exciton modes . . . . .	35
3-4	Exciton-polariton condensation . . . . .	37
3-5	Sample . . . . .	45
3-6	General setup scheme . . . . .	46
3-7	Schematic of Stokes polarimeter . . . . .	48
4-1	Schematic of Hanbury Brown and Twiss interferometer . . . . .	58
4-2	Schematic of HBT experiment . . . . .	59
4-3	Polarization resolved correlation functions . . . . .	61
4-4	Power dependence of correlation functions . . . . .	63
4-5	Photon statistics vs Pump ellipticity . . . . .	65
4-6	Larmor precessions . . . . .	66
4-7	Larmor precessions vs Pump Power . . . . .	67
4-8	Time series polarization switching . . . . .	68
4-9	HBT of $g_{H,H}^{(2)}(\tau)$ , $g_{V,V}^{(2)}(\tau)$ and $g_{H,V}^{(2)}(\tau)$ . . . . .	69
4-10	Photon statistics and DOP . . . . .	69
4-11	Residual ellipticity influence on statistics . . . . .	73
4-12	Laser vs Condensate HBT . . . . .	74
4-13	Trap parameters affecting photon statistics . . . . .	76
4-14	Fit function for polariton condensate . . . . .	77
5-1	Schematic of Hong-Ou-Mandel interferometer . . . . .	85
5-2	HOM for independent lasers . . . . .	85
5-3	Condensate HOM dip and relation to phase coherence . . . . .	88
5-4	HOM for condensate in different traps . . . . .	90
5-5	HOM with superbunched light . . . . .	90
5-6	HOM of precessing light . . . . .	91

5-7 The periodicity of HOM revival . . . . . 92

# Chapter 1

## Introduction

In the twenty-first century, the physical and chemical research communities were paying close attention to several low-dimensional crystal forms made of carbon. The electronic properties that are displayed by nanodiamonds, fullerenes, carbon nanotubes, and graphene, make them promising for a large range of applications in nano-electronics and photonics (8). Realizing ideal one-dimensional crystals, monatomic chains of sp-carbon, is one of the most difficult objectives for nano-fabrication technology. However, the traces of two stable allotropes of sp-carbon (polyynes and cumulene) have been found in nature: in meteorite craters, interstellar dust, natural graphite, and diamond mines (9; 10; 11). It appeared to be challenging to extract freestanding carbon chains from natural sources because of the high chemical reactivity of linear acetylenic carbon and its low stability at ambient temperature and atmospheric pressure. Numerous attempts to artificially create polyyne chains have had little to no success. Since one-dimensional atomic chains are typically unstable in vacuum, their synthesis appears to be a tough problem as Landau theorem (12) states that fluctuations obstruct the growth of perfect one-dimensional crystals. It was shown that stabilization may be achieved by the use of heavy anchor atomic groups (13). One-dimensional carbon crystals are expected to exhibit unique mechanical, optical, and electronic properties (14). According to recent theoretical works (15), one-dimensional carbon chains could form the most robust of all known crystals. Moreover, the mono-atomic carbon chain is seen to be one of the candidates to observe features commonly present for quantum emitters, such as sub-Poissonian

photon statistics of the emitted light.

Photon statistics is of central importance in laser physics and quantum optics, and serves as an essential toolbox for the characterization of optical sources ranging from pure single-photon sources to super-thermal highly fluctuating light sources. The photon distribution width in a laser defines its noise properties, whose understanding is at the heart of many applications such as laser cooling (16), precise interferometry (17), and optical communications, to name but a few (18). Alongside semiconductor optical microcavities in the weak (19) and strong-coupling regime (20), particle statistics of heavily correlated many-body systems such as atomic (21) and photonic Bose-Einstein condensates (22) retains strong interest.

While an ideal laser obeys the Poisson photon distribution, practical devices usually suffer from excessive noise that broadens the distribution and affects phase stability. Mode competition is one detrimental effect generating excessive, so-called, super-Poisson noise in conventional semiconductor microcavity lasers (23; 24; 25). On the other hand, stochastic mode switching allows for the study of the intriguing phenomena of chaos in photonic systems (26) and opens the door for new optoelectronic applications, such as, ghost imaging (27) and multi-photon microscopy (28) with super-bunched light. Additionally, mode beating enables low-energy ultrafast optical communications (29). The intrinsic linear mode-coupling usually dominates over nonlinear effects in conventional microlasers, however, in semiconductor structures with strong light-matter interactions, this may not be the case.

Exciton-polaritons (here on polaritons) are bosonic quasiparticles originating from strong light-matter coupling of excitons with photons in semiconductor microcavities (30). They can undergo power-driven Bose-Einstein condensation (31) into a spinor order parameter corresponding to the right-hand and left-hand circular polarization of the emitted light like, in a conventional semiconductor spin-laser (32). The complex order parameter cannot be directly observed in a photoluminescence (PL) experiment, however resolving PL in polarization bases gives access to the components of the condensate pseudospin (Stokes) vector (33), providing the orientation and the degree of polarization, which will be discussed in Section 3.2.3. Besides its fundamental importance, the spin degree of freedom is particularly attractive

for applications as a spintronic device (34). The exciton component makes the polariton Bose gas inherently nonlinear due to pair-particle interactions, permitting experimental observation of quantum correlations (35; 36) and superfluidity (37; 38). Particle number fluctuations and statistics are intimately connected to the linewidth of polariton condensates, playing an essential role in understanding the fundamental limits of their coherence properties (39). Today, polariton condensates offer unprecedented all-optical control to build large interacting nonlinear networks (40), and devices ranging from amplifiers (41; 42), transistors (43; 44; 45), tunnelling diodes (46), routers (47; 48; 49), phase-controlled interferometers (50), topological insulators (51), switches (52; 53; 54) to volatile memory elements (55). For polariton condensates under resonant excitation, it has been shown, that the coherence time reaches up to  $\sim$ ns in the optical-parametric-oscillation regime (56). However, under non-resonant excitation and in the presence of an incoherent exciton reservoir, the coherence time is limited to  $\sim 10 - 100$  ps (57; 58; 59; 60). The presence of an exciton reservoir causes depolarisation (61), which was evidenced through spinor dephasing in second-order photon correlation measurements (62). With the possibility of non-trivial photon statistics at hand, the exploration of two photon interference as an effect for optically trapped polariton condensates was not yet conducted.

The effects of two photon interference are most pronounced for the non-classical, quantum light sources. The magnitude of Hong-Ou-Mandel (HOM) effect is highest for a variety of the single photon sources, yielding high degree of photon antibunching. Originally observed through the process of spontaneous parametric down conversion (SPDC) (63; 64), the effect was later shown for quantum dots (65), nitrogen-vacancy centers in diamonds (66), and trapped ions (67) and molecules (68). Having a light source which ensures a high purity of photon indistinguishability is absolutely crucial for many of the current applications of the HOM effect, such as, precision measurements (69; 70), quantum state analysis (71), quantum communications (72; 73), quantum state engineering (74), quantum computation (75; 76; 77) to have the light source which ensures high purity of the photon indistinguishability. At the same time, the indistinguishability measurements the imperfect single photon sources conducted (78), demonstrating the limitations induced by noise and ways

to account for unwanted errors in applications. Moreover, a trace of effect under discussion is present even for classical light sources such as, for example, the laser.

This thesis begins with an investigation into chains of sp-carbon by photon counting in the time resolved photoluminescence. The spectral resolution of the setup allowed for observation of lifetime decays of emission from chains with particular numbers of atoms. Next, the theory and concepts of polariton condensation will be presented, in particular the configuration of optically trapped polariton condensation, where the condensate is spatially separated from the exciton reservoir, extending the coherence time to over two orders of magnitude ( $\sim 1$  ns) compared to the polariton lifetime ( $\tau_p = 6.5$  ps). Such a long coherence time allowed for study of spinor dynamics of the condensate, which is free from transient dynamics under continuous wave nonresonant optical excitation, in contrast to short pulsed experiments (62). Applying polarization resolved photon correlation tomography and precise spectroscopy, enabled the unravelling of complex spinor condensate dynamics and the connection to photon statistics. Through engineering of the photon statistics of the spinor condensate, demonstration of the crossover from super-thermal photon distribution to a highly coherent state will be shown. At the variety of the photon statistical regimes, the observation of the Hong-Ou-Mandel effect was done for the trapped polariton condensates in the ground state. The observations revealed the different visibility of the effect when compared to what is known for the classical light source, laser.

**Chapter 1 - Introduction** The introduction into the research topics is given and the actuality of the conducted research is reflected.

**Chapter 2 - TCSPC of linear carbon chains emission** The first results of carbon mono-chains lifetime dynamics and presence of fine spectral structure at liquid helium temperature.

**Chapter 3 - Polaritons In Semiconductor Microcavities** The general theory of the polaritons and polariton condensates, as well as present our experimental technique of characterization of polariton condensate.

**Chapter 4 - Hanbury Brown and Twiss effect** In this chapter, we go in-depth on the photon statistics of the polariton condensate and show the non-trivial dynamics of its spinor. We present the means of controlling the emitted photon statistics by the variety of ways.

**Chapter 5 - Hong Ou and Mandel effect** We present the experimental observations of Hong-Ou-Mandel effect for the trapped polariton condensate and give possible explanations of the observed behaviors.

**Chapter 6 - Conclusion** Finally, we discuss our key obtained results and the express ideas for future improvements.

# Chapter 2

## TCSPC of linear carbon chains emission

Nowadays, it goes without saying that, new materials bring the attention of the scientific community. For the longest time, the only known structures made up of carbon atoms were coal, graphite and diamonds. The discovery of fullerenes in 1985 (79; 80), carbon nanotubes in 1993 (81) and graphene in 2004 (82), caused the methods of artificial synthesis evolved rapidly. However, it was not until 1969 (9), that linear carbon chains were discovered in graphite gneiss. The two types of chains: polyynes, which has alternating single and triple electronic bonds, and cumulenes, which has consistent double bonds between neighbouring atoms, were shown to be a direct band-gap semiconductor and a metal, respectively (83; 84). Recently, our collaborators managed to synthesize such polyynes carbon chains and we were able to study their spectral and temporal properties.

In this chapter, we are going to discuss the technique of time-correlated single photon counting (TCSPC) in Section 2.1 and its application for the study of exciton lifetimes in carbon chain-gold nanoparticle complexes in Section 2.3. The description of the sample under investigation will be given in Section 2.2. The first investigation of the temporal characteristics for polyynes chains, and through the experimental investigation the existence of trions was shown at cryogenic temperatures.

## 2.1 TCSPC technique

Time-correlated single photon counting (TCSPC) was used as a technique since 1960s where it has been exploited for the measurement of excited nuclear states (85; 86). It was an innovative way to measure a weak signal from a sample, and derive its radiative decay time. This ensured it became an essential tool in the fields of photonics and material sciences.

The basic principle of a TCSPC experimental set up is as follows: the sample is irradiated with a short laser pulse, and then the time between the excitation pulse, and the a photon emitted from the sample is measured on the detector at some later time,  $t_d$ . By recording the delays  $t_d$  between the trigger pulse and the detection event for enough events we can accumulate a characteristic histogram. The photoluminescence decay time,  $t_{decay}$ , can be extracted from such histogram. The intensity of the photoluminescence is chosen so that the detector is triggered by a single photon. We rely on the probability distribution of the photon emission process, and thus on the distribution of events of photon detection. As a result a histogram with the number of detection events versus time can be plotted, similar to what is shown in Figure 2-5. Typical fluorescence for commonly used fluorophores last from hundreds of picoseconds to tens of nanoseconds. In order to recover not only fluorescence lifetimes, but also the decay shape, which is done by multi-exponential fitting of the decays, one must be able to temporally resolve the recorded signal at least to such an extent, that the decay is represented by some tens of samples.

Typically, the time resolution for recording an analog signal is limited by the bandwidth of the detector, which for an avalanche photodiode or APD is typically limited to 50ps. The instrument response function (IRF) of such devices cannot be shorter than a single electron response (SER). The IRF reflects how a infinitely short signal is seen by the instrument, and SER is the actual detector output pulse for a single photoelectron created through the process of effective photon absorption and amplification through an avalanche process within the detector. The full width at half maximum (FWHM) of a SER pulse is dependent on the detector structure, but is typically on the scale of ns, which is very long compared to the width of

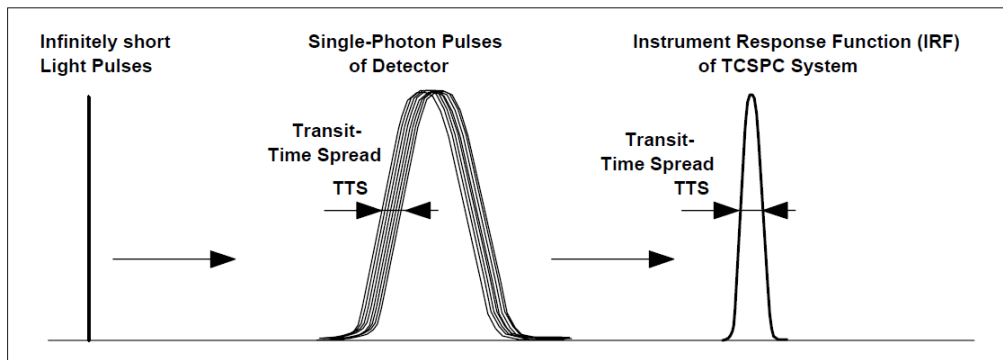


Figure 2-1: Response of detector to infinitely short light pulses and IRF of TCSPC system. Adopted from (87).

the excitation laser pulse. However, time resolution for TCSPC is much better than nanoseconds, because the effective instances of photon arrival are derived from arrival times of detection pulses and these times can be measured with higher accuracy, compared to the width of the SER. The IRF of the whole TCSPC system, and not just the detector, is thus limited to, so called, transit time spread (TTS), as schematically shown in Figure 2-1. The effect of TTS in APDs can be explained as different conditions for the build-up of the carrier avalanche and different avalanche transit times due to different depth of absorption from photon to photon. The typical IRF of the TCSPC system that was used for the investigation of decay curves discussed in this chapter and following correlation measurements in chapters 4 and 5, is  $100ps$ . The APDs may be referred to as a single photon avalanche diodes, or SPADs, when used as a photon-counters in, so-called, Geiger mode. In this mode, a photon can trigger an avalanche of electrons of various magnitude, however, only the fact that the avalanche was caused is important, as it indicates the event of photon detection.

## 2.2 Polyynes chains sample

The samples, provided by the group of Dr. Stella Kutrovszkaya from Stoletov Vladimir state university, were linear carbon chains with gold nanoparticles of  $\approx 10nm$  or  $\approx 100nm$  attached at both ends of the chain, deposited on top of cover glass films. The size of the nanoparticles were estimated by TEM images and near infrared transparency spectra (not shown). The sample was synthesized

with the laser ablation from liquid (LAL) method (88). The laser processing resulted in the formation of polyynes threads (89). The stabilisation of linear carbon chains was achieved by adding spherical gold nanoparticles of nanoscale sizes to the solution (90; 91). The methodology of fabrication of such nanoparticles has been developed in the past, with pioneering reports found in Refs. (92; 93). The fabrication process of carbon monochain samples is a sophisticated process and not the main topic of this thesis, thus only a few details are given here. However, thorough explanations are given in the supplementary material of Ref (4) where information on dynamical light scattering and carbon chains with visibly attached gold nanoparticle TEM images are presented.

The folding of chains, and formation of kinks occurs predominantly at the single bonds, we observe spectral resonances from the straight chains, containing even numbers of carbon atoms ranging from 8 to 24, which can be seen from the broad peaks in 2-3(a). Typically, these are straight parts of longer linear chains attached by both ends to golden nanoparticles. Thus, kinks separate each linear chain into several straight parts. It is important to note also that if nanoparticles at the opposite ends of a carbon chain are of different sizes, the difference of their work functions, results in the charging of the carbon-nanoparticle complex that acquires a stationary dipole moment. The mentioned work function is formally known as an energy required to remove an electron from a solid to a point in the vacuum immediately outside the solid surface. For the gold particles, the energy can vary in the range from 5.10 to 5.47 eV, and also can be dependent on the cluster or, in the case of used samples, on the particle (94; 95). The theoretical approach to describe the change of work function would be to correlate the properties of the metal clusters to the properties of bulk. The idea is that the gold nanoparticle is a bulk material perturbed by its surface and its size, approaching the bulk properties with increasing particle size (94; 96), and with the particle of size of  $\approx 10nm$  having almost 30% of its atoms on the surface (97). The difference in work function between different surfaces is known to cause a non-uniform electrostatic potential in the vacuum within the vacuum chambers. This dipole polarisation provides a tool for the chain ordering via an applied voltage (98) during deposition. The chains deposited were intentionally

ordered by passing the solution through a stationary electric field, as demonstrated in Figure 2-2(a). Figure 2-2(b), in the green highlighted area, shows the TEM image of the central part of the bundle of parallel carbon chains of the length exceeding  $\approx 40nm$ . Gold nanoparticles remained outside the frame of the image in this figure. The previous studies showed that an ensemble of carbon chains in a bundle forms a kind of one-dimensional van der Waals crystal, where the distance between neighboring chains exceeds the inter-atomic distance in a single chain by a factor of 3.6 (98). We note that only about one half of carbon bundles have gold nanoparticles of significantly different sizes at their ends. These bundles are dipole polarized due to the difference of the work function of gold nanoparticles. It was shown, and will be discussed later, that these structures are hosts to positively and negatively charged trions that manifest themselves in the low-temperature PL spectra. The other half of carbon-metal nanostructures are formed with gold nanoparticles of the same size. These are not polarized and not aligned by the electric field and mostly host electrically neutral excitons, seen in Figure 2-2(b) in the red highlighted areas. The difference between the two regimes is of stark contrast and clearly observed from the TEM image.

## 2.3 Spectral and temporal characteristics

To understand these structures better the spectral and temporal characteristics were measured. Initially, the PL spectra of the deposited polyynes shown in the Figure 2-3 was obtained. The absorption spectra for similar structures has been studied before (99), so excitation was performed quasi-resonantly, with a femtosecond laser at wavelengths between 370 and 390 *nm*. As it can be seen from the Figure 2-3(a) there are several distinct lines contributing to the integrated spectra. These different peaks are due to contributions in the integrated PL from carbon chains of different lengths. Here, it is possible to claim that most contribution is coming from the chains of 8 - 18 atoms length (88). It was observed, that with the increasing length of the chain, optical transitions shift to lower energies, as was theoretically predicted, (99; 88). The energy gap between the highest occupied

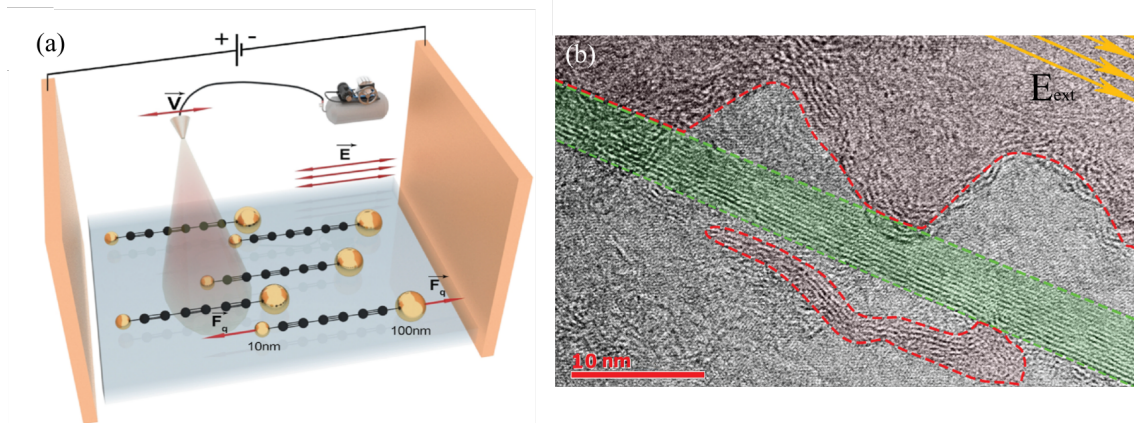


Figure 2-2: (a) Schematic illustration of the deposition method which produces aligned carbon chains which are stabilised by gold nanoparticles at either end of their chain. Due to the difference in work functions of gold nanoparticles attached to the ends of a carbon chain, the connected structure becomes dipole polarised. The external electric field orients the polarized chains, so that over a half of them appear to be aligned when deposited on a substrate by sputtering. (b) High resolution TEM image of bundles of carbon chains. In the green region chains appear to be co-aligned with the applied external electric field  $E_{ext}$ , while in the red they are oriented semi-randomly. Adopted from Ref. (4).

molecular orbit (HOMO) and the lower unoccupied molecular orbit (LUMO) decreases with chain length and shows a trend toward a finite gap of 0.48 eV with increasing length of the carbon chains (88). However, as the temperature reaches 4K, a distinct fine splitting in the PL spectra is observed, clearly demonstrated in Figure 2-3(b). Such a characteristic splitting can be seen for the 10, 12 and 14 atoms chains. The full width at half-maximum was determined as 3meV for the narrowest and most dominant peak, and 15 and 25 meV for the peaks at lower energies. It should be noted here, that lower energy peaks of these triplets are less obviously stand out within the spectrum, and thus FWHM is defined with a bigger error. Whilst there were many possible explanations for the above tripling of the state, the prediction for the emergence of charged exciton complexes has prevailed. Metal nanoparticles can support carbon chains with additional carriers, and from theoretical modeling (3) based on the experimental observation, it was shown that the tripling is due to the presence of a neutral exciting, and a positive and a negative trion.

The temporal characteristics were measured at both cryogenic and room temper-

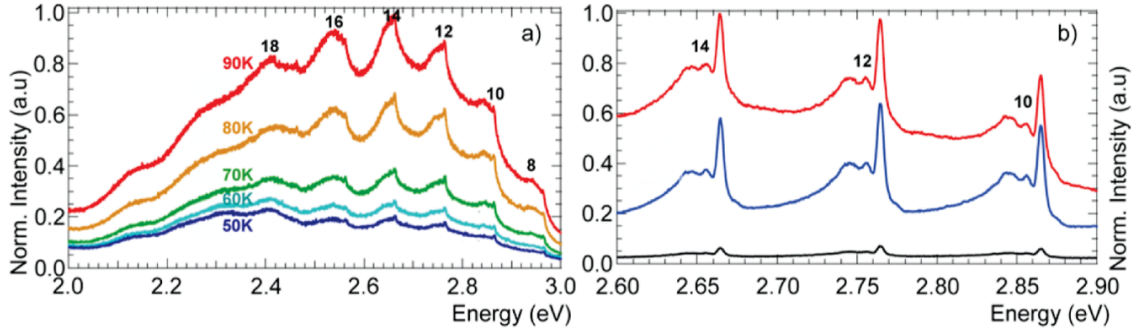


Figure 2-3: (a) Spectra taken at temperatures from 90 to 50  $K$ . The laser excitation wavelength is 390 nm, with intensity of 5  $mW$  and acquisition time of 10  $s$ . (b) PL spectra taken at 4  $K$ . Red, blue, and black curves correspond to the excitation wavelengths of 390, 380, and 370  $nm$ , respectively. The acquisition time 40  $s$ .

atures, using time-resolved photoluminescence (TRPL), a TCSPC technique which is spectrally resolved, as shown in Figure 2-5. Spectral band selection was achieved with a variable liquid crystal spectral filter (VariSpec), and is presented in the insets in Figure 2-5(a,c), with color coding. The high-temperature spectra show double-exponential behavior, this reflects the interplay between nonradiative (due to carrier thermal hopping between the neighboring chains) and radiative channels of the exciton decay. On the other hand, low temperature TRPL exhibits a mono-exponential decay with times of the order of  $1ns$ , which is similar to the excitonic lifetimes of the carbon nanotubes (100; 101). The lifetime is increased for the longer polyene chains and can be explained as behavior of dipole transition matrix elements. With the measured time-resolved optical characteristics of excitons in carbon chains and its found property to be dependent on the band-gap of the chain and the lengths of straight parts of the chains, it can be practically applied as tool for fine tuning of the radiative properties of such structures. The detailed exciton modeling with in-depth explanation of the observed features in the emission spectra can be found in Ref. (3) and the theoretical description of the radiative decays of excitons in kinked chains can be found in Ref. (5). The calculation within the developed model showed that excitons in the polyene chains are characterized by the radiative lifetimes of the order of 1 ns, that nicely agrees with the experimental data. Having obtained, within the framework of the model, the correct order of magnitude for the radiative lifetime for the experimentally observed lengths, the next step was to study the dependence

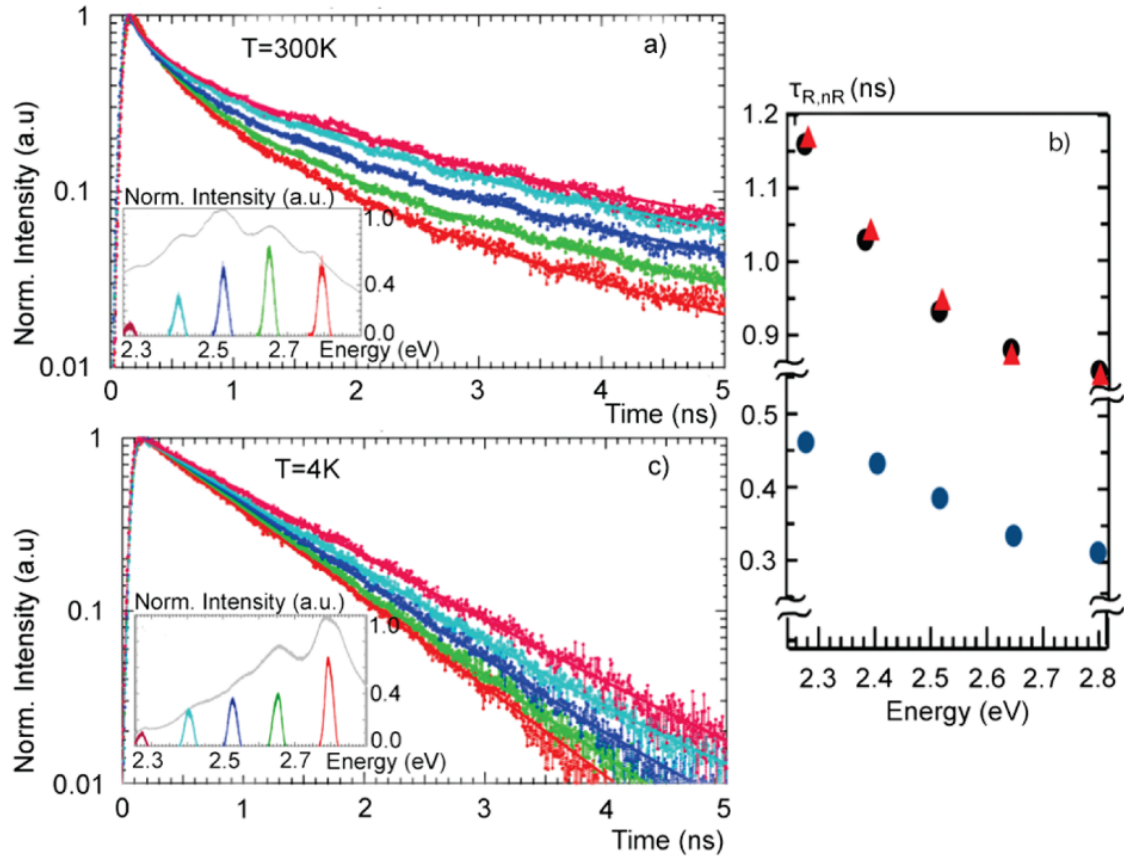


Figure 2-4: (a, c) TRPL signal acquired at the room temperature and at 4 K, respectively. The insets show the spectral bands that correspond to the TRPL curves of parts a and c, respectively. The colors match shows the extracted decay times of the TRPL signal taken at room temperature and cryogenic, respectively. (b) Red and black points correspond to the deduced radiative decay time at the room temperature (red) and helium temperature (black). The blue points show the nonradiative decay times, extracted from the room temperature TRPL curves in (a).

of the radiative lifetime on the band gap width. For that purpose the chain length parameter was fixed, and a plot of the calculated exciton lifetime as a function of the band gap value, which depends on the number of atoms in the linear parts of polyyne chain between kinks in our experiments, was done. The derivation of the master equation of the developed model was done by our collaborators, here we only present results in Figure 2-5, which shows a dependence of the exciton radiative lifetime on the band gap for the chains of different length, and how it matches with the experimentally obtained dynamics.

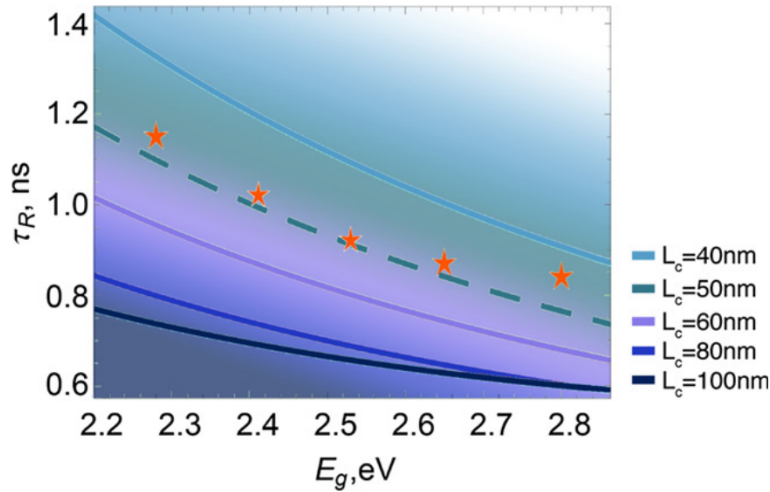


Figure 2-5: The radiative decay time of excitons versus the band gap energy for different fixed distances between NPs  $L_c = 40 \text{ nm}$ ,  $60 \text{ nm}$ ,  $80 \text{ nm}$ ,  $100 \text{ nm}$  respectively. Stars display the experimental data. The best fit is achieved at chain length  $L_c = 50 \text{ nm}$  (shown by the dotted line). Adopted from Ref. (5)

### 2.3.1 Conclusion

To conclude this section, it should be underlined, that the triplet fine structure, which is very well seen at cryogenic temperatures is essentially independent of the length of the chain, while the absolute energies of the transitions increase for the shorter chains. We show that the sharp peaks emerging at low temperatures in the PL spectra of gold-stabilized carbon chains are indicative of the exciton and trion transitions based on the edge electronic states in the chains. The time-resolved optical response of excitons in carbon chains is found to be dependent on the band-gap of the chain, and it is the lengths of the straight parts of the chains that provides a control tool for fine tuning of the radiative properties of carbon chains. Moreover, the observation of radiatively active excitons in these one dimensional carbon chains is of a great fundamental interest. These observations demonstrate a high potentiality of synthesized polyynes chains for optoelectronic applications, especially in search of nanolasing devices and single photon emitters. Since it might be possible to observe singular energy transitions from a gold NP - carbon monochain complex, the photon statistics is expected to have sub-Poissonian distribution, bringing prove for the emitter to be of quantum nature. In order to investigate such possible features, measurements of second order coherence function would be the next logical step to

look into.

The topic of second-order correlation functions is the main focus of this thesis. The study of second-order coherence is fundamental to the classification of light sources and is a useful measurement to determine light source photon noise and its photon statistical properties. Therefore, in the following chapters an investigation into the photon statistics of another light source with exceptional properties, that of an optically trapped polariton condensate, will be undertaken.

# Chapter 3

## Polaritons In Semiconductor Microcavities

An optical cavity is an optical resonator, created with a set of mirrors to facilitate the confinement of light, and a standing wave within the cavity. In this thesis, the physics observed within the microcavity is discussed, which are typically on order of micrometers wide. By choosing a proper intra-cavity material, such as quantum wells (QW), and placing it at the anti-nodes of cavity standing wave, it is possible to reach the strong coupling regime between the confined cavity mode and QW excitons. In this regime, a new quasi-particle, known as an exciton-polariton emerges. This particle, a short-lived mixture of light and matter, combines properties from both particles: it has a light effective mass from the photon, whilst inheriting strong nonlinearities from the exciton part - in short, it is the ideal hybrid.

In this chapter, we are going to discuss the fundamental physics behind the process of light matter coupling in microcavities, and the specifics of the microcavity used in this work for polarities condensation. We are going to succinctly discuss the mechanism of polariton condensation, including the excitation methods, and the polarisation properties. Then, the sample used throughout the experiments in this thesis will be described. Finally, the experimental techniques used to create an optically trapped polariton condensate will be explained.

## 3.1 Coupling of light and matter

Depending on the technological application there have been developed various geometries of microresonators, such as micropillar cavities, microtoroid resonators and photonic crystal cavities. The most common microcavity, however, is the planar cavity comprising two parallel flat mirrors. Typically, the mirrors of these Fabry-Perrot-type cavities are either formed by highly reflective metallic surfaces, or by distributed Bragg reflectors (DBRs), i.e. periodically patterned two-dimensional dielectric or semiconductor layers of alternating refractive index. While in the former case the cavity modal field vanishes almost completely at the metallic surface, in the latter case the electric field has a substantial penetration depth into the Bragg mirror.

### 3.1.1 DBR

One of the key features of microcavity design is that the reflectivity properties of the DBR structures can be changed by either varying the number of reflector layers, or the refractive index difference between the periodically alternating materials. An example of a DBR structure is shown in Figure 3-1(a), containing pairs of alternating layers (shown in purple and blue) of different refractive index. The incident light will be partially reflected, and partially transmitted through the structure. How much of the light would be reflected or transmitted depends on range of parameters such as the light's frequency  $\omega$  and its polarisation, the material of DBR's, its characteristic sizes, and the angle of incidence (102). The DBR's refractive index profile is schematically shown in Figure 3-1(b), it is a periodic structure of alternating layers made of materials of different refractive indices. Layers are designed to have a thickness  $d_i$  that equals a quarter wavelength of incoming light, i.e.  $d_i = \lambda_0/4n_i$  with  $i = 1, 2$ . The wavelength  $\lambda_0$  corresponds to the light frequency  $\omega_0 = 2\pi c/\lambda_0$ , for which the DBR structure is created, where  $n_1, n_2$  are the refractive indices of the DBR materials. When light is incident to the DBR structure, constructive interference occurs, due to the design thickness, resulting in huge reflectivity for a certain light frequency  $\omega_0$ . The reflectivity spectrum of such a structure contains a

stopband centred around  $\omega_0$  as depicted in Figure 3-1(c). The width of this stopband  $\Omega_{SB}$  is determined by the refractive index composition (102) as follows,

$$\Omega_{SB} = \frac{8c |n_1 - n_2|}{\lambda_0(n_1 + n_2)}, \quad (3.1)$$

clearly as the contrast between the  $n_1$  and  $n_2$  gets bigger,  $\Omega_{SB}$  increases as well.

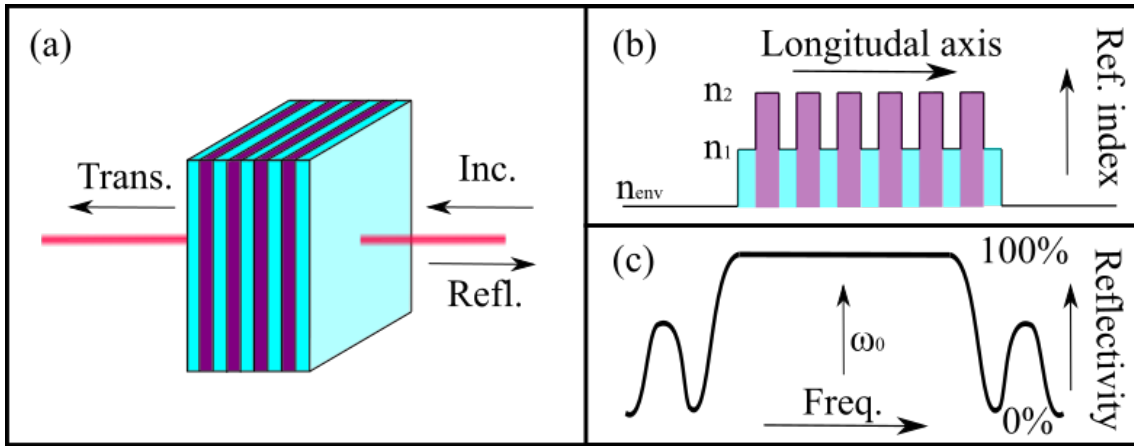


Figure 3-1: (a) Scheme of the DBR with refractive index profile shown in (b). (c) Reflectivity spectrum for light under normal incidence onto the structure.

### 3.1.2 Cavity

A microcavity can be engineered by adding an extra layer within the DBR structure, as shown in Figure 3-2(a), where thickness and refractive index of the cavity layer are labeled as  $d_c$  and  $n_c$ . This extra layer works as an anomaly, a defect inside a perfectly periodic structure. This effectively results in a new (confined) photonic mode. The condition for resonance of the confined Fabry-Pérot modes can be written as

$$\omega_j = j \frac{\pi c}{n_c d_c}, j \in \mathbb{N}^+. \quad (3.2)$$

Here lets assume that the light incidence is normal, absorption is negligible and the reflectivity of the DBR structure is high.

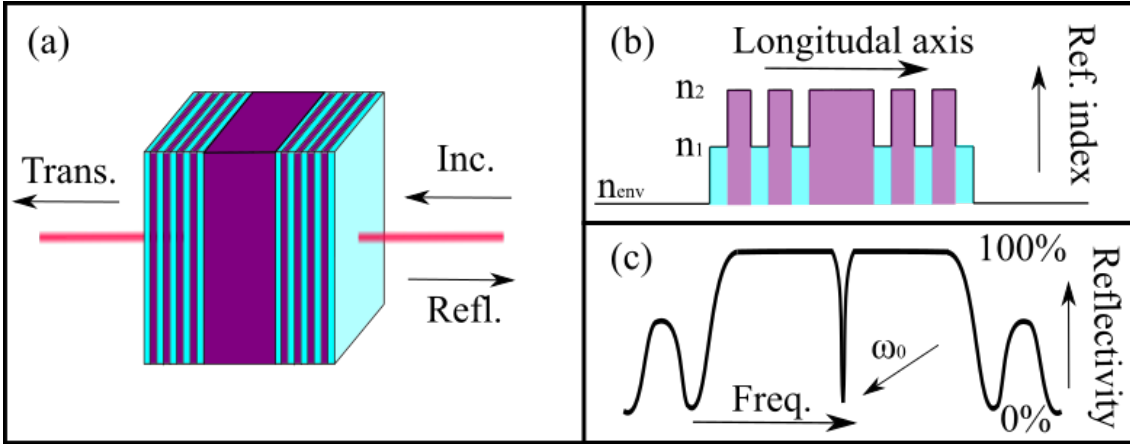


Figure 3-2: (a) Scheme of the microcavity structure with refractive index profile shown in (b). The cavity mode with frequency  $\omega_0$  placed within the DBR stopband results in a modification in the reflectivity spectrum depicted in (c).

The free spectral range (FSR)  $\Delta\omega$ , is an important characteristic of any resonator, and can be given as follows

$$\Delta\omega = \frac{\pi c}{n_c d_c}. \quad (3.3)$$

In the case of thin resonators, which microcavities are, the FSR  $\Delta\omega$  is usually much bigger than the stopband width  $\Omega_{SB}$  of the reflectors. Thus, giving us effectively only one longitudinal mode that can exist within the microcavity.

The reflectivity spectrum of such a microcavity under normal incidence is schematically depicted in Figure 3-2(c). Here, lets once again, assume that light is at normal incidence to the cavity. The mode with frequency  $\omega_c$  results in diminished reflectivity about this frequency, and is due to resonant tunneling of photons through the structure. For the cavity presented in Figure 3-2, the cavity resonance frequency  $\omega_c$  is in the center of the reflectivity stop band and, this symmetric condition is realised when the cavity thickness  $d_c$  is chosen to be a multiple of a half-wavelength, i.e.  $d_c = j\lambda_0/2n_c$ . Still the mirrors have some losses which cause spectral broadening of the resonant mode as shown in Figure 3-2(c). It is an important characteristic of the

microcavity, and is connected to lifetime  $\tau_c$  of photons inside the cavity. Structural defects and other effects can cause additional channels for photon lifetime relaxation. A resonator with resonance frequency  $\omega_j$  and spectral FWHM  $\delta\omega_j$  is characterised by its quality factor  $Q$  (102), given by

$$Q = \frac{\omega_j}{\delta\omega_j}. \quad (3.4)$$

It serves as a gauge for the proportion between the energy lost during each oscillation cycle, and therefore the energy remaining in the cavity. The cavity photon lifetime  $\tau_c$  and energy loss are related, such that

$$\tau_c = \frac{Q}{\omega_j}. \quad (3.5)$$

Each cavity mode is defined by a wavevector  $\mathbf{k}$ , taking lateral translational invariance of the system into account, that exhibits continuous dispersion in transverse directions ( $x$  and  $y$ ) but is quantized in longitudinal directions ( $z$ ). Denoting the lateral wavevector as  $k_{\parallel}$ , the cavity in-plane dispersion can be approximated as parabolic for small angles of incidence,

$$\omega_{\mathbf{j}}(\mathbf{k}_{\parallel}) = \omega_j \sqrt{1 + \frac{k_{\parallel}^2}{\omega_j^2 n_c^2 / c^2}} \approx \omega_j + \frac{\hbar k_{\parallel}^2}{2m_c}. \quad (3.6)$$

Where  $m_c = \hbar\omega_j n_c^2 / c^2$  the cavity effective photon mass (see reference (103) for the derivation). As such, the effective photon mass in microcavities is very light and typically in the order of  $10^{-5}m_e$ , where  $m_e$  is the free electron mass.

### 3.1.3 Excitons in quantum wells

In crystal solids, excitons are electrically neutral particles, created by the Coulomb interaction of electrons and holes. When an electron in a bulk semiconductor is

excited from the valence band to the conduction band through optical stimulation, an exciton is produced. The particle wavefunction and energy spectra of excitons resemble a bound electron-proton pair, and have a hydrogen atom-like structure (103). For a bulk semiconductor with bandgap energy  $E_g$ , free excitons have the energy dispersion relation

$$E_n^{X,3D}(\mathbf{k}) = E_g - \frac{R_0}{n^2} + \frac{\hbar^2 k^2}{2M_X}, n \in \mathbb{N}^+ \quad (3.7)$$

where  $M_X = m_e^* + m_h^*$  is the sum of the effective electron and hole masses  $m_e^*$  and  $m_h^*$ . The magnitude of the binding energy,  $E_n$ , is defined by the exciton Rydberg energy  $R_0$ , which also serves as a gauge for the quasi-thermal particle's stability. It is dependent on material properties such as the permittivity  $\epsilon$  and reads as

$$R_0 = \frac{2e^4 m_X}{(8\pi)^2 \epsilon^2 \hbar^2}. \quad (3.8)$$

The introduction of the exciton effective mass  $m_X = m_e^* m_h^* / (m_e^* + m_h^*)$  represents the reduced mass of electron and hole. Due to their larger effective mass  $m_X$  and smaller permittivity  $\epsilon$ , wide-bandgap semiconductors such as *ZnO* ( $R_0 \approx 62\text{meV}$ ) or *GaN* ( $R_0 \approx 26\text{meV}$ ) typically have a larger Rydberg energy than, for instance, *GaAs* ( $R_0 \approx 4.2\text{meV}$ ) (103), this means that excitons in wide-bandgap semiconductors can be stable at room-temperature ( $k_B T \approx 25\text{meV}$ ).

An efficient potential well structure for electrons and holes is represented by a quantum well (QW), which is a small layer of semiconductor sandwiched between two alternative semiconductor layers with significantly different conduction valence band energies. The 2D exciton dispersion relation is produced by the longitudinal confinement of electrons and holes within the QW, which results in an additional exciton confinement energy term ( $E_C$ ), such that

$$E_n^{X,2D}(\mathbf{k}_{\parallel}) = E_g + E_c - \frac{R_0}{(n - 1/2)^2} + \frac{\hbar^2 k_{\parallel}^2}{2M_X}, n \in \mathbb{N}^+. \quad (3.9)$$

It's crucial to keep in mind that the ground state binding energy ( $n = 1$ ) of excitons in QWs is 4 times higher than that of the bulk energy spectrum [3.7]. Additionally, the exciton oscillator strength  $f$  in QWs is higher than in bulk due to the enhanced spatial overlap of the electron and hole wavefunctions in confined systems (103). The oscillator strength is a dimensionless quantity that describes the probability of photon absorption and emission as well as the effective coupling between light and the optically active exciton mode. As a result, low-dimensional structures like QWs are the ideal platforms for researching excitonic events at elevated temperatures and with improved optical transitions.

### 3.1.4 Strong coupling and exciton-polaritons

The interplay of photonic and electrical modes within a system is essential for optoelectronic applications and devices. One can incorporate an active medium, in the form of a semiconductor QW structure, into the cavity layer for the proposed planar cavity, which results in optically active and confined excitonic modes. A schematic of the microcavity structure, containing coupled photon and exciton modes, is depicted in Figure 3-3(a) and (b). The coupling strength of cavity photons and QW excitons is characterised by their interaction energy  $\hbar\Omega_R$ , where the Rabi frequency  $\Omega_R$  describes the rate at which energy is exchanged between the photonic and excitonic modes. Assuming normal incidence, Fig 3-3(c) depicts the microcavity reflectivity spectrum of a strongly coupled cavity. Here, the degeneracy between the bare cavity and QW exciton energies is lifted, and two new resonances, split by the Rabi frequency  $\Omega_R$ , appear. The hybridized exciton-polariton modes of the system resemble these resonances. The energy repulsion of two connected resonators can be explained in terms of two linearly coupled harmonic oscillators as detailed in the following. The coupled exciton-photon Hamiltonian  $H$  can be expressed as (102)

$$H = \sum_{k_{\parallel}} E_C(k_{\parallel}) C_{k_{\parallel}}^{\dagger} C_{k_{\parallel}} + \sum_{k_{\parallel}} E_X(k_{\parallel}) X_{k_{\parallel}}^{\dagger} X_{k_{\parallel}} + \frac{\hbar\Omega_R}{2} \sum_{k_{\parallel}} [C_{k_{\parallel}}^{\dagger} X_{k_{\parallel}} + C_{k_{\parallel}} X_{k_{\parallel}}^{\dagger}]. \quad (3.10)$$

where  $E_C(k_{\parallel})$  and  $E_X(k_{\parallel})$  denote the cavity mode and QW exciton mode energy dispersion relations, respectively, with details given in Eqs. 3.6 and 3.9. The first two terms in 3.10 represent the bare cavity and bare exciton energies with photon and exciton field operators  $C_{k_{\parallel}}$  and  $X_{k_{\parallel}}$ , respectively. The third term describes exciton-photon interactions, represented by absorption and emission cycles at frequency  $\Omega_R$ .

Since there is no mixing of inplane wavevectors  $k_{\parallel}$  present in 3.10, the Hamiltonian  $H$  can be split into the sum,  $H = \sum_{k_{\parallel}} H_{k_{\parallel}}$ , where each term  $H_{k_{\parallel}}$  can be written in matrix notation,

$$H_{k_{\parallel}} = \begin{bmatrix} E_C(k_{\parallel}) & \hbar\Omega_R/2 \\ \hbar\Omega_R/2 & E_X(k_{\parallel}) \end{bmatrix}. \quad (3.11)$$

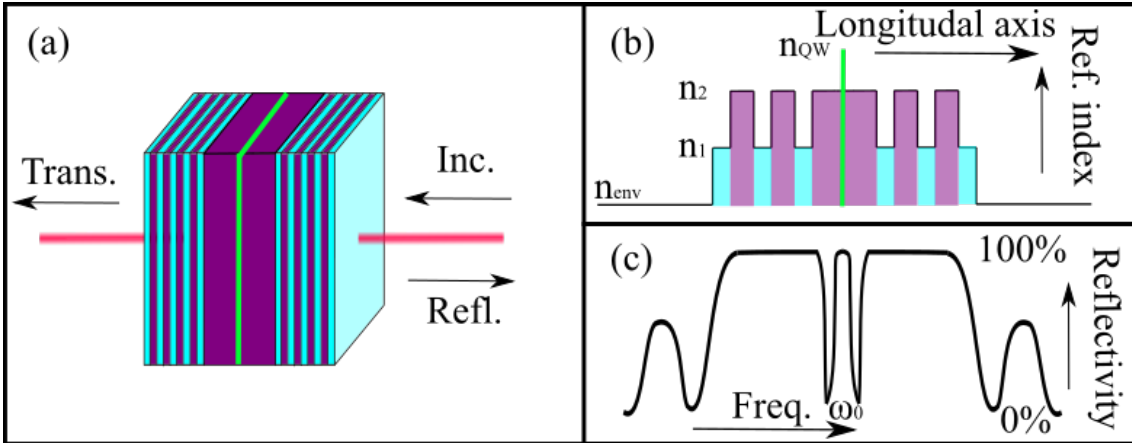


Figure 3-3: Strong coupling of photon and QW exciton modes. (a) Schematic of the microcavity structure with refractive index profile shown in (b). (c) Reflectivity spectrum for normal incidence. Strong coupling of photon mode and excitonic mode result in the formation of two polaritonic resonances, which are split by the Rabi frequency.

Diagonalisation of the Hamiltonian  $H_{k_{\parallel}}$ , then yields the eigenstates: the upper (UPB) and lower (LPB) polariton branches, represented as

$$|LP_{k_{\parallel}}\rangle = c_{k_{\parallel}}|C_{k_{\parallel}}\rangle - \chi_{k_{\parallel}}|X_{k_{\parallel}}\rangle, \quad (3.12)$$

$$|UP_{k_{\parallel}}\rangle = \chi_{k_{\parallel}}|C_{k_{\parallel}}\rangle + c_{k_{\parallel}}|X_{k_{\parallel}}\rangle. \quad (3.13)$$

The mixing coefficients  $c_{k_{\parallel}}$  and  $\chi_{k_{\parallel}}$  denote the so-called, Hopfield coefficients. Their squared norms,  $|c_{k_{\parallel}}|^2$  and  $|\chi_{k_{\parallel}}|^2$ , represent the photonic and excitonic component for each branch, respectively. Furthermore, the dispersion relation for each polariton branch is given by

$$E_{UP,LP}(k_{\parallel}) = \frac{1}{2}[E_C(k_{\parallel}) + E_X(k_{\parallel}) \pm \sqrt{[E_C(k_{\parallel}) - E_X(k_{\parallel})]^2 + \hbar^2\Omega_R^2}]. \quad (3.14)$$

While the uncoupled bare exciton and cavity modes might be in resonance at some inplane wavevector  $k_{\parallel}$ , i.e.  $E_C(k_{\parallel}) = E_X(k_{\parallel})$ , the new eigenstates of the system experience a repulsion, yielding an anti-crossing in the dispersion split by the Rabi energy  $\hbar\Omega_R$ . The spectral repulsion and hybridisation of exciton and cavity modes are schematically illustrated in Figure 3-4. The flatness of the bare exciton energy branch  $E_X(k_{\parallel})$  seems to be dispersion-less because of the heavy effective mass of excitons compared to cavity photons.

The Hopfield coefficients for the lower polariton branch are given by

$$|c_{k_{\parallel}}|^2 = \frac{E_{UP}(k_{\parallel})E_X(k_{\parallel}) - E_{LP}(k_{\parallel})E_C(k_{\parallel})}{[E_C(k_{\parallel}) + E_X(k_{\parallel})]\sqrt{[E_C(k_{\parallel}) - E_X(k_{\parallel})]^2 + \hbar^2\Omega_R^2}} \quad (3.15)$$

$$|\chi_{k_{\parallel}}|^2 = \frac{E_{UP}(k_{\parallel})E_C(k_{\parallel}) - E_{LP}(k_{\parallel})E_X(k_{\parallel})}{[E_C(k_{\parallel}) + E_X(k_{\parallel})]\sqrt{[E_C(k_{\parallel}) - E_X(k_{\parallel})]^2 + \hbar^2\Omega_R^2}} \quad (3.16)$$

The coherent superposition of the exciton mode and bare photonic mode, with mixing parameters defined by 3.12 and 3.15 results in polaritons, which are hybrid quasi-particles. As said above, cavity photons are characterized by a small effective mass  $m_c^* \approx 10^{-5}m_e$  and a short lifetime  $\tau_c \approx 1 - 100\text{ps}$ , stemming from the quality factor of the cavity, while semiconductor excitons, such as in GaAs, have a larger

effective mass  $m_X^* \approx 0.2m_e$  and longer radiative lifetime  $\tau_X \approx 0.1 - 1ns$ . The characteristics of polaritons can be adjusted by varying their respective Hopfield coefficients, which can be achieved by shifting the cavity mode with respect to the exciton. For this purpose, microcavities are often fabricated with a wedge in the thickness of the cavity layer, allowing for experimental access to different exciton-photon detunings,  $\Delta = E_C(0) - E_X(0)$ , and experimental tuning of the polariton Hopfield coefficients. The illustrated energy dispersion in Figure 3-4 represents the case when  $\Delta = 0$ . Regardless of the detuning parameter, for large emission angles the upper (lower) polariton branch will asymptotically tend to the photonic (exciton) mode, which is expressed by its Hopfield coefficient  $|\chi|^2 \rightarrow 1$ . Experimental results presented in this thesis are obtained using a negatively detuned microcavity, as the LP particles with small in-plane wavevector  $k_{\parallel} \approx 0$  have a large photonic component, whilst LP particle at large wavevectors are dominantly excitonic.

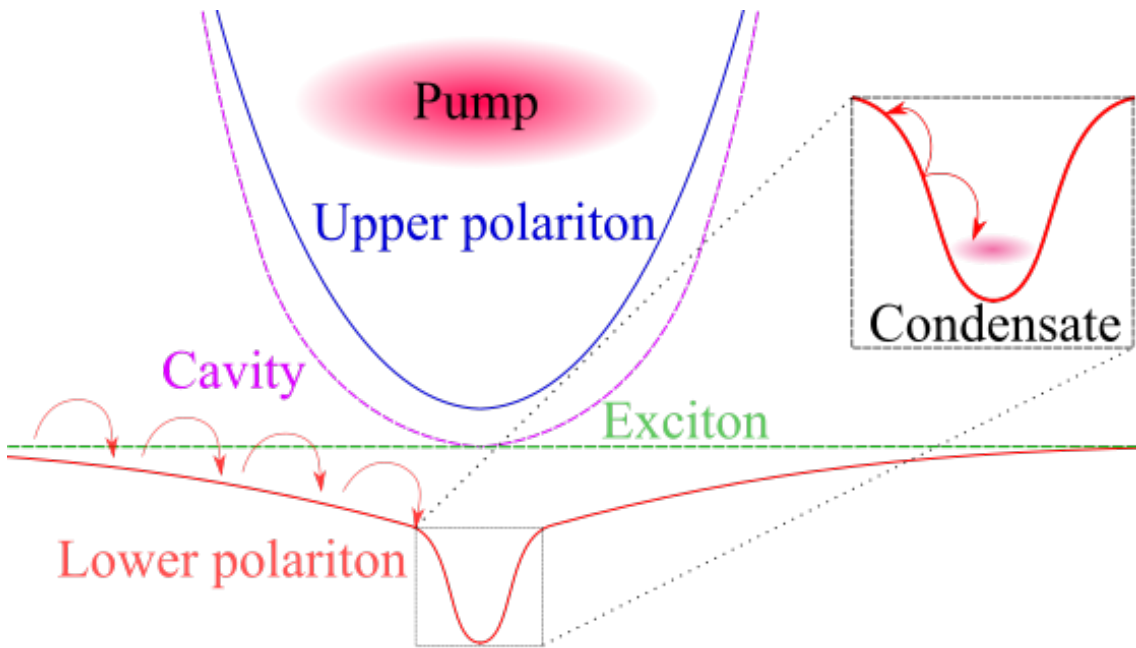


Figure 3-4: The process of polariton condensation. Strong coupling of cavity photonic and excitonic mode get split into two new lower- and upper-polaritonic modes near  $k \approx 0$ . The LP branch polaritons scatter, and dissipate through interactions with phonons down to the bottleneck region of the dispersion curve. The particles then scatter into low energy condensate state through polariton-polariton interactions.

It should be noticed here that by embedding multiple QWs within the micro-

cavity at the anti-nodes of the cavity electric field distribution helps to increase the Rabi splitting  $\Omega_R$  and decreases the exciton density per QW. This is necessary, to improve the stability of cavity polariton, and lower the particle density to avoid the Mott transition, and enable polariton condensation to be possible.

Importantly, the energy level repulsion described in 3.14, occurs however weak the interaction term  $\hbar\Omega_R$  is. The cavity mode and exciton mode, denoted by the terms  $\gamma_c$  and  $\gamma_x$ , will both always have a finite linewidth-broadening dissipation term present in any practical realization. The coherent superposition of exciton and photon mode as in 3.12, can then only occur, when the coupling term is larger than any dephasing mechanism. In other words, the coupled-mode frequency splitting  $\Omega_R$  should be larger than the bare mode linewidths, i.e.  $\Omega_R > \gamma_c, \gamma_x$ . In the strong coupling regime the energy transfer rate  $\Omega_R$  between bare cavity and exciton modes is larger than the particle loss rates. In order to accurately capture the dynamics of a system characterized by a Hamiltonian with large off-diagonal coupling terms in quantum mechanics one must diagonalize the system. The polariton modes are then emerge as the new eigenstates of the system. When the energy transfer rate is slower than the respective exciton and photon decay rates,  $\Omega_R < \gamma_c, \gamma_x$ , the system is said to be weakly coupled. A VCSEL can be represented by a microcavity that operates in the weak coupling regime. If that is the case, perturbative methods can be used to analyze the dynamics of the system.

## 3.2 Condensation of exciton-polaritons

Bose-Einstein condensation (BEC) of ultra cold atomic gases (104; 105), the superfluid phase transition of liquid helium (106; 107), the non-equilibrium phase transition of photons in a laser are some examples of bosonic phase transitions with the emergence of a macroscopically coherent state. General criteria of a bosonic condensate, whether in thermal equilibrium or not, were outlined by Penrose and Onsager (108), and Yang (109). Being bosonic quasi-particles, microcavity polaritons are capable of undergoing bosonic phase transitions, with the emergent macroscopic occupation of a single-particle quantum state. Due to the link between quantum

mechanical wave dynamics and experimental accessibility on a macroscopic scale, such macroscopic quantum phenomena have drawn interest from many different fields in physics and chemistry.

### 3.2.1 Mechanism of polariton condensation

The process condensation of exciton-polaritons happens in the following way. External source creates a population of polaritons, which mostly occupy LP branch of the energy-momentum dispersion in case of our sample. Subsequently, two mechanisms lead polaritons into condensation: exciton-photon scattering and polariton-polariton scattering. The LP branch polaritons scatter and energy dissipate down through interaction with phonons. This persists to the momenta for which exciton and photon energy difference is comparable to the Rabi splitting  $\Omega_R$ , where the photonic fraction of the polariton becomes significant. At this point, scattering rates are reduced due to a decrease in density of states and due to a decrease of the excitonic Hopfield coefficient  $|\chi|^2$ . Moreover, polariton lifetimes are greatly reduced at small momenta due their growing photonic component  $|c|^2$ , generally preventing the polariton gas from reaching thermal equilibrium. The accumulation of excitonic particles figuratively speaking, leads to a bottle neck for the polaritons. From this point the second cooling mechanism dominates, with polaritons interacting with other polaritons in the reservoir, causing some polaritons to scatter to lower energies, closer to  $k = 0$ , and the other polariton to higher moments, as per momentum conservation. In the end, a macroscopic population is created at momenta close to  $k = 0$  through the process of stimulated scattering. The schematic representation of this effect can be seen in Figure 3-4.

Due to the light effective mass of the polaritons,  $m_p \approx 10^{-5}m_e$ , polaritons are looked upon as a good platform to study macroscopic quantum phenomena at elevated temperatures. However, polaritons have been shown to have a short life time of (1 – 100ps) before they decay. Therefore, reaching thermal equilibrium is rarely possible, and for that reason, an out-of-equilibrium macroscopic occupation of the single state is termed "polariton lasing". In recent works, however, long lifetimes of polaritons in high Q-factor microcavities were achieved, observing BEC of optically

trapped polaritons in thermal equilibrium (110). Although there is a debate about the terminology for the coherent source of light created by the mechanisms described above (111; 112; 113), a very good comparison of the photon laser, polariton laser and polariton BEC is given in Reference (114). As such, in this work let us call the coherent many-body state as "polariton condensate". We will discuss this matter in more details in Chapter 4 of this thesis, however, it is reasonable to mention here that the polariton condensate can be excited resonantly or off-resonance, in other words - incoherently. In order to study the second order coherence properties of the condensate with minimal inherited coherence from the excitation source, the off-resonant excitation was utilized throughout the course of this work. The polariton condensates formed in this way have several properties important to this work::

- Long-range spacial coherence across the system above condensation threshold.
- Narrowing of the emission linewidth at threshold, thus increase of temporal  $g^{(1)}$  coherence.
- Spectral blue-shift of the LP branch as well as condensate line with increasing excitation. Evidence of polariton repulsive nonlinear interactions (115).
- Condensation trapping with an optically engineered potential.

### 3.2.2 Confinement of polariton condensates

Incoherent pumping allows for the shaping of potential landscape for the polaritons, and the creation of optical traps through excitonic reservoir. The open-dissipative Gross-Pitaevskii equation for the polariton condensate can be written in the following manner:

$$i\hbar \frac{\delta \Psi_{LP}}{\delta t} = \left[ -\frac{\hbar^2}{2m_{LP}} \nabla_{\perp}^2 + g_c n_R(\mathbf{r}, t) + i\frac{\hbar}{2}(R n_r(\mathbf{R}, t) - \gamma) \right] \Psi_{LP} \quad (3.17)$$

$$\frac{\delta n_R}{\delta t} = -(\gamma_{ex} + R|\Psi_{LP}|^2)n_R(\mathbf{r}, t) + P(\mathbf{r})$$

where  $\Psi_{LP}$  is the condensate wavefunction,  $n_R$  is the reservoir density,  $P(\mathbf{r})$  is the spatially modulated excitation rate,  $\gamma$  and  $\gamma_{ex}$  are the loss rates of polaritons and

reservoir excitons respectively,  $R$  is the stimulated scattering rate with  $g_c$  and  $g_R$  being polariton-polariton and polariton-exciton interactions respectively (116). Even in the simplest case of Gaussian single spot pumping, the condensation can occur near the pumping spot through gain-induced self-trapping (117).

Currently there are a variety of methods for polariton trapping. Some of them are trapping polaritons through its photonic component, for example, using a cavity masking technique (118) or etched micro pillar cavities of controlled diameter (60). In this dissertation however, confinement through the polaritons excitonic reservoir, similarly to Ref. (119) was utilized. By structuring the excitation light beam, an engineered reservoir density distribution  $n_R(\mathbf{r})$  induces a repulsive potential, effectively creating a trap for polaritons. Moreover, it was shown that, polariton interactions in a trapping potential can be significantly enhanced (120). The temporal coherence of such trapped polariton condensates have been studied with the respect of the confining trap size. Furthermore, a comparison of the second order coherence function for a trapped polariton condensate versus a ballistically expanding polariton condensate was performed at phase transition point, i.e. at threshold (121).

### 3.2.3 Polarization of polariton condensate

Polarization of light can be described using a set of values  $S_0$ ,  $S_1$ ,  $S_2$  and  $S_3$  called Stokes parameters. These parameters are commonly combined into a vector, known as the Stokes vector. The vector can be normalized on its  $S_0$  parameter, which represents the total light intensity. Now, the three-dimensional Cartesian space in which normalized Stokes vector can be plotted directly to, is called Poincare sphere. Each axis, of this space, passes through pair of poles, which represent sets of the orthogonal polarisations of light. The length of the Stokes vector, represents the degree of light polarisation, and the trajectory of the vector on Poincare sphere depicts how the polarisation state of light evolves.

The polarisation of polariton condensate allows for access to the condensate spin, since right- and left-circularly polarised photons are coupled almost exclusively to spin-up and spin-down optically active reservoirs, respectively. Accordingly, polariton condensates can be expressed by a spinor order parameter  $\Psi = (\psi_+, \psi_-)^T$

with spin-up and spin-down polaritons ( $\psi_{\pm}$ ) correspond to right- and left-circularly polarised light respectively. The spin physics for the polariton condensate is often described by the pseudospin formalism (122; 33). Where the polarisation of the condensate emitted light directly relates to the polariton spin structure, thus the emission Stokes vector  $\mathbf{S}$  becomes a measure of polariton pseudospin. The particle number of the polariton condensate, and the normalized components of the Stokes vector can be given as follows:

$$\begin{aligned} S_0 &= |\psi_+|^2 + |\psi_-|^2, \\ S_1 &= 2\text{Re}(\psi_+^* \psi_-)/S_0, \\ S_2 &= -2\text{Im}(\psi_-^* \psi_+)/S_0, \\ S_3 &= (|\psi_+|^2 - |\psi_-|^2)/S_0. \end{aligned} \tag{3.18}$$

Although, a great deal of the condensate excitation regimes requires a comprehensive analysis of the physics leading to the formation of polarization, for this thesis, we will focus on the regime where condensation occurs in the groundstate of the optically induced trap, at momenta  $k \approx 0$  and without any higher order trap modes being excited (7). This is the common measurement regime throughout this thesis, unless mentioned otherwise.

It has been observed that depending on the excitation polarization, the incident laser power required for obtaining polariton condensation at the nonlinearity, was different. Moreover, the circularly excited polariton condensates were seen to emit co-circularly polarized light, whilst linearly polarized excitation appears to create condensates with a degree of polarization,  $DOP = \sqrt{S_1^2 + S_2^2 + S_3^2}/S_0 \approx 0$ , right after condensation threshold. The threshold drift can be explained as with purely circularly polarized excitation the same-spin Coulomb interactions dominate over opposite spin interactions (123; 124). A circular polarized excitation beam results in a dominantly spin up, or down, populated reservoir of incoherent excitons, depending on direction of the polarization rotation, which will reach threshold density sooner and undergoes stimulated scattering into a co-circularly polarized condensate (125; 126). The DOP of circularly pumped condensate remains close to unity mainly dictated by the  $S_3$  component, for the range of powers up to  $2P_{th}$ ,

after which opposite circular component appear to influence the polarization, decreasing the value of the  $S_3$  with the degree of linear polarization (DLP) staying  $DLP = \sqrt{S_1^2 + S_2^2} \approx 0$ . Interestingly, the polarization of the condensate emitted light right above threshold when pumped with linear polarization appears to be unpolarized through in the integrated polarimetry measurements, similarly as to below condensation threshold. However, all other signs of condensation, such as linewidth narrowing and blue shift of LPs were shown in this regime. Intensifying the excitation density leads to an increase of the DLP, and emergence of a linear component with determined orientation. The orientation of this component is dependent on the location on the sample. This effect is attributed to a joint effect of sample local birefringence induced in-plane polarization splitting and increasing condensate nonlinearity (33) resulting in condensate pseudospin pinning. The absence of this pinning in the region of lower powers, with  $DOP \approx 0$  is due to low nonlinearity of the condensate because of low occupation, making the polarization weakly pinned.

For the elliptically polarized excitation, the condition of tilted limit cycle regime can be fulfilled. This effect can be viewed as periodic precession of the condensate pseudospin around some effective magnetic, emergent due to structural and pump induced energy splittings in the system, discussed in more detail in 4, which manifests itself as an effective depolarization of the condensate emitted light, when measured with a time resolution less than the cycle period. The pseudospin in this regime undergoes mixture of pump- and self-induced Larmor precessions, overcoming the pinning effect, as was also predicted theoretically (33).

### 3.3 Experimental methods

In order to breath life into the ideas, an experimental setup to characterize the QWs embedded microcavity was built. As time passed, the setup which started from clear optical table, had become more complicated and sophisticated, constantly improving and facilitating more and more capabilities. Here, we will discuss general implemented methods of creating a trapped polariton condensate and its characterization. In chapters 4 and 5 we will go into detail on the HBT and HOM interfer-

ometry, respectively, which was implemented to study the second-order coherence of the polariton condensate and its emission indistinguishability.

### 3.3.1 Sample

The microcavity with embedded QWs sample on which all of the experiments were done was developed in the Sheffield National Center for *III – V* technologies. The substrate is a *GaAs* wafer which supports sets of DBRs, the bottom DBR consists of 26 pairs and the top DBR of 23 pairs of *GaAs* and *AlAs*<sub>0.98</sub>*P*<sub>0.02</sub>. The intracavity layer consists of three pairs of *In*<sub>0.08</sub>*Ga*<sub>0.92</sub>*As* QWs within the *GaAs* spacer located in the anti-nodes of the standing wave, with two more QWs in the top and bottom node. The schematic representation of the sample is shown in Figure 3-5. There is a slight wedge of the intracavity layer allowing for tuning of the cavity photonic mode detuning to the excitonic mode by scanning along the wedged direction of the sample surface. During the experiments, the sample was mounted in a closed-cycle cryostat and cooled down to the temperature of  $T = 4K$ . The specially designed coldfinger mount allowed for the detection from wafer side and from DBR side of the sample.

### 3.3.2 Experimental setup

The scheme of the experimental setup is shown in Figure 3-6(a). The single mode, narrow light continuous wave (CW) Ti:Sapphire laser (M-squared SOLSTIS, later swapped to Matisse-CR) was primarily used for the experiments. Tuned to the wavelength ( $\lambda_{ex}$  783nm), which corresponds to the second Bragg minimum of the cavity band to the high energy edge of the reflectivity stopband, for non-resonant excitation of QW excitons, resulting in the emergence of the upper (UP) and lower (LP) polariton branches. Notably, the transmission of the laser light through the sample on this wavelength is almost non-existent due to the absorption of the light by the *GaAs* substrate, and therefore the necessity of spectral filtering in the transmission path is absent. However, in the reflection path, a lowpass dichroic mirror was used to reflect only the condensate emission. The CW excitation was temporally

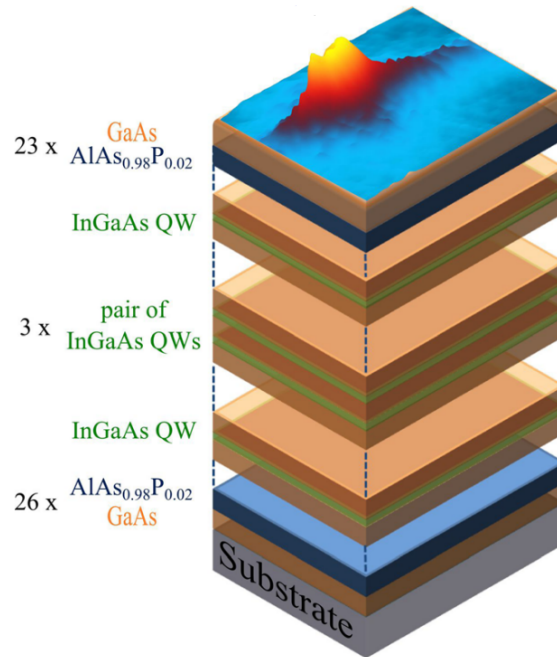


Figure 3-5: Microcavity sample with embedded QWs. Adopted from the (127)

modified by acousto optical modulator (AOM) with square shape pulses working at a 1 kHz frequency with a 10% duty cycle, which was done primarily not to overheat the sample.

As an experimental side note, that might be useful for anyone opting to conduct similar research, I would point out the following nuance. The AOM modulates the signal on macroscopic times if compared to that of TCSPC electronics and detectors. Because of that, when compared to the un-modulated signal, the detectors might get over-saturated with the number of incoming photons, if the beam is not attenuated equally to the modulation duty cycle. Unfortunately, the effect of over-saturation does not visually presents itself during the measurement of the second-order coherence function, and can lead to the false values of accumulated statistics.

The spatial shaping of the excitation beam profile is done by incorporating a spacial light modulator (SLM). An algorithm developed in our lab, and described in Ref (115) allowed for shaping the excitation beam profile into virtually any shape. The laser beam, with transverse Gaussian distribution, is directed to the liquid crystal based matrix of the SLM. An analytically calculated 2D Fourier image, e.g.

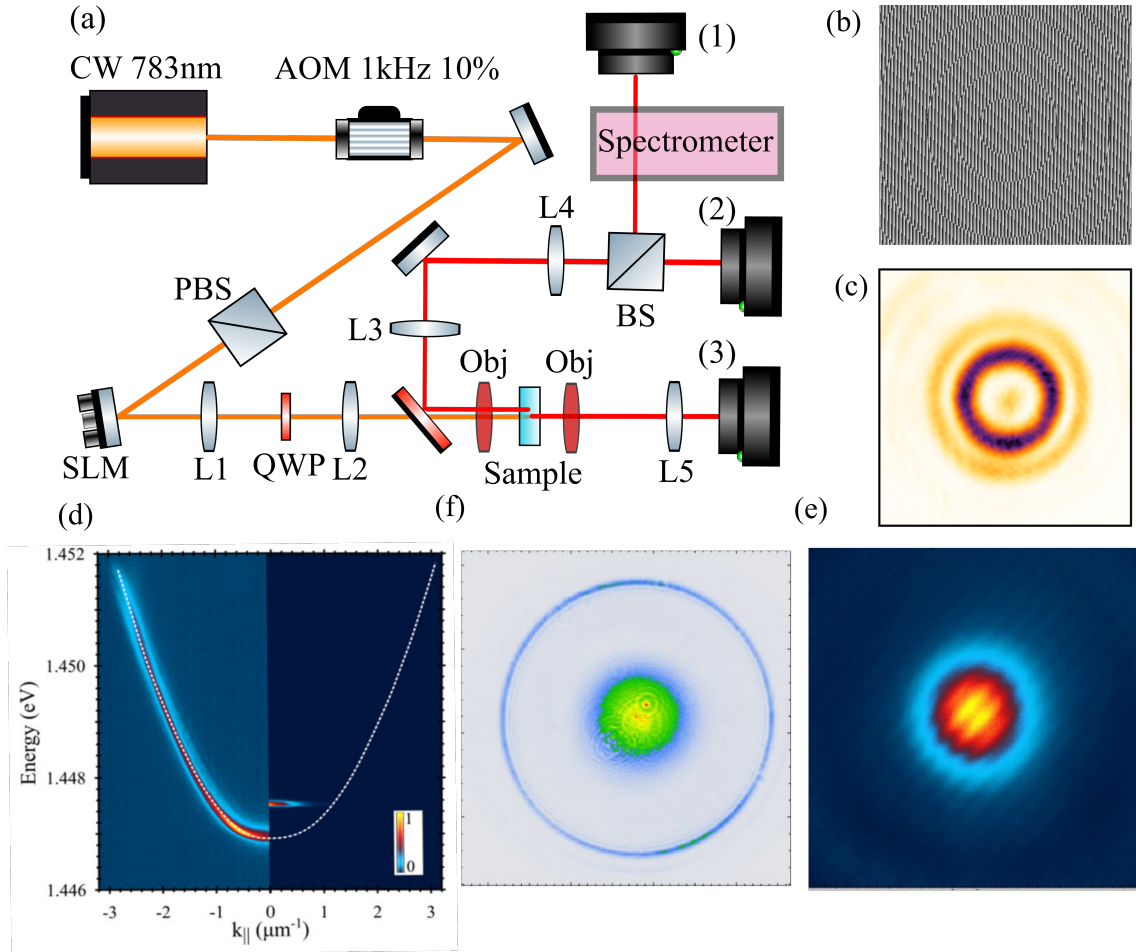


Figure 3-6: (a) General scheme of the experimental setup. The sample is excited with a single mode CW laser. The excitation is temporally modulated with AOM and spatially modulated with SLM. Excitation beam polarization is modulated with QWP. Characterization of polariton condensate dispersion is done on camera (1) and shown in (d). Characterization of momentum space image is done on camera (2) and shown in (f). Characterization of the real space image is done on camera (3) and shown in (e). (b) Example of the calculated hologram applied onto the SLM. (c) Example excitation beam profile forming an annular optical trap. (d) Dispersion image LP branch below condensation threshold (left) and above condensation threshold in optical trap (right). (e) Momentum space image of the condensate in optical trap. (f) Real space image of the condensate in optical trap.

shown in Figure 3-6(b), to create the desired pump profile, such as Figure 3-6(c), is applied onto the SLM and the liquid crystal screen reorders itself to form a hologram. This hologram deflects the beam and forms the desired image in the focal plane of the first lens (L1). By the means of lenses (L1 and L2) and high numerical aperture (NA) microscope objective, the designed pump profile is projected onto the plane in which sample is located inside of the cryostat. The pump profile for optical trapping of the

polariton condensates, for this work, was formed into the annular trap of  $\approx 10\mu m$  in diameter, similar to Figure 3-6(c). Due to a technical requirement, SLM is only able to shape/alter horizontally polarised light, therefore a PBS was installed right before the device, to prevent overheating of the liquid crystal screen. However, as it was discussed in Section 3.2.3 the ability to tune the excitation polarization is essential for the investigation of the condensate and thus, an important piece of the excitation scheme is a quarter waveplate (QWP), which was used to tune the excitation beam polarization ellipticity.

In order to study the polariton condensate in the trap ground state, it is necessary to track the energy-momentum dispersion of the condensate PL, as well as the condensate momentum space image. The momentum-space Fourier image of the trapped condensate is reflected from the sample, transmitted through the optical system with lenses (L3 and L4), and projected on to cameras (1) and (2). For the dispersion imaging, light travels through the high resolution spectrometer, which has spectral resolution of  $\approx 30\mu eV$ , resulting in the images shown in Figure 3-6(d). In this figure, example dispersions of the LP branch when pumped before condensation threshold, (left), and for the case of pumping above condensation threshold in the trapping potential (right), with condensation happening near  $k \approx 0$ . The example momentum space image of trapped condensate can be seen in Figure 3-6(e), with the most of polaritons occupying the center of the momentum space close to  $k \approx 0$ . Real space imaging of the excitation beam profile onto the sample is essential in order to avoid any unnecessary experimental errors, such as, asymmetry of the trapping potential, which can break the system U(1) symmetry (2), or additional excitation spots within the trapping potential due to aberrations or being at an incorrect focal plane, which can lead to polarization imprinting by the excitation beam (61). Furthermore, observation of the condensate formed within the optical trap, after non-linear growth in intensity, is important in order to determine the condensation threshold, which changes depending on excitation pump profile (128). An example of the condensate image above the threshold is presented in 3-6(e). Visible fringes are due to the known effect of optical etaloning.

### 3.3.3 Integrating polarimetry

The Stokes polarimeter, is an experimental setup allowing for the measurement of all Stokes parameters simultaneously, allowing for the extraction of direction and length of the Stokes vector  $\mathbf{S} = (S_1, S_2, S_3)$ . The parameters correspond to the horizontal-vertical ( $S_1$ ), diagonal-antidiagonal ( $S_2$ ), and right-, left-hand circular ( $S_3$ ) polarization of the emitted cavity light of the condensate PL. With four detectors, and division of the incoming PL with beam splitters, followed by pre-aligned polarization optics as shown in Figure 3-7 the direction and length of Stokes vector as well as its trajectory, can be plotted, given that the Stokes parameters are calculated as follows

$$\begin{aligned} S_1 &= \frac{I_H - I_V}{I_H + I_V} = \frac{I_1 - I_2}{I_1 + I_2}, \\ S_2 &= \frac{I_D - I_A}{I_D + I_A} = \frac{4I_3 - (I_1 + I_2)}{I_1 + I_2}, \\ S_3 &= \frac{I_{\sigma^+} - I_{\sigma^-}}{I_{\sigma^+} + I_{\sigma^-}} = \frac{4I_4 - (I_1 + I_2)}{I_1 + I_2}. \end{aligned} \quad (3.19)$$

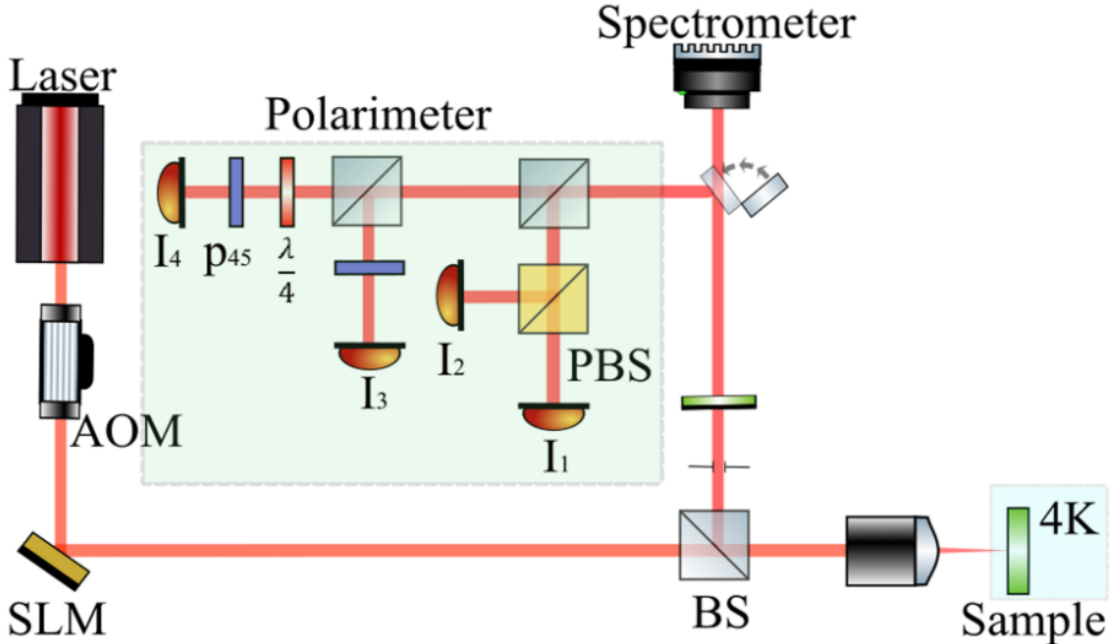


Figure 3-7: Schematic of the experimental setup and polarimeter. AOM, SLM, PBS, and BS stand for acousto-optic modulator, spatial light modulator, polarizing, and nonpolarized beamsplitter, respectively.  $p_{45}$  is a linear polarizer with the axis rotated  $45^\circ$  with the respect to the horizontal axis. Adopted from Ref. (7)

Here,  $I_{H,V,D,A,\sigma(\pm)}$  correspond to the derivable intensity for each of the polarization poles of the Poincare sphere, and  $I_{1,2,3,4}$  denote the light intensity signal recorded with each detector marked on the Figure 3-7. This polarimeter was carefully calibrated with a laser tuned to the emission line of the polariton condensate to account for any spectral-related technical errors. As the condensate PL intensity, especially below condensation threshold is quite low, a set of lock-in amplifiers was used to enhance the signal-to-noise ratio. Normally, the temporal resolution of the detection scheme of this design is limited by the detector rise and dead times. But in this case, lock-ins were the most constraining element due to 100ms integration time.

The integrated polarization maps of condensate PL measured by my colleague with this polarimeter showed several distinct regimes of the polariton condensate behavior, and how the condensate degree of polarization (DOP) depends on the excitation power and excitation polarization (7).

*Here I note that the I was not the primary investigator for optically trapped condensate integrated polarimetry, and that the polarimeter was developed by my colleague and co-author.*

# Chapter 4

## Hanbury Brown and Twiss effect

Experiments conducted by Robert Hanbury Brown and Richard Quintin Twiss in 1956 (129; 130), as well as, development of a new class of light emitters by Arthur Leonard Schawlow and Charles Townes(131), sparked an interest for photon statistics in the scientific community. The classical interpretation was sufficient to describe the statistical properties of conventional light sources, as well as for coherent light(132; 133). However, with the development of quantum-mechanical theory(134; 135), a new type of light source was predicted. Rapid development of experimental techniques brought different regimes of photon statistics which can be found from various light sources: bunched, random, and anti-bunched.

In this chapter, a brief theoretical introduction into the formation second-order coherence formulas will be given in both the frameworks of semiclassical and quantum theories of light. Following this, an overview of the existing work which has been done on the photon statistics and correlation measurements in polariton condensates in a variety of structures, will be given. Finally, the experimental methodology used to measure the photon statistics from optically trapped polariton condensates and their spinor dynamics will be shown, and the results discussed.

## 4.1 Theory of optical coherence

### 4.1.1 Semiclassical theory

To discuss statistical properties of the light sources, a suitable approach would be the use of the semiclassical theory of light, in which we treat light fields classically, but interaction of photons with detectors in a quantum sense (136). In the framework of this theory, light is represented by a random complex analytic signal  $V(x)$ , where  $x$  is a space-time coordinate  $(\mathbf{r}, t)$ . The optical intensity is given by  $I(x) = |V(x)|^2$ , and so, the fluctuations of light are characterized by  $V(x)$  and its stochasticity (137). Lets introduce important descriptors of light at the point  $x$ , probability density  $P(I)$ , mean value  $\langle I \rangle$ , and variance  $Var(I)$ . Two correlation functions can characterise the fluctuations at space-time coordinates  $x_1$  and  $x_2$

$$\begin{aligned} G^{(1)}(x_1, x_2) &= \langle V^*(x_1)V(x_2) \rangle, \\ G^{(2)}(x_1, x_2) &= \langle I(x_1)I(x_2) \rangle. \end{aligned} \tag{4.1}$$

However, these amplitude and intensity correlation functions usually are presented in the following normalised form, and commonly called the degrees of first- and second-order coherence functions

$$\begin{aligned} g^{(1)}(x_1, x_2) &= G^{(1)}(x_1, x_2) / \sqrt{[\langle I(x_1) \rangle \langle I(x_2) \rangle]}, \\ g^{(2)}(x_1, x_2) &= G^{(2)}(x_1, x_2) / [\langle I(x_1) \rangle \langle I(x_2) \rangle]. \end{aligned} \tag{4.2}$$

The degrees of coherence, in the frame work of semiclassical theory, are required to satisfy the following inequalities:

$$\begin{aligned} 0 &\leq |g^{(1)}(x_1, x_2)| \leq 1, \\ g^{(2)}(x_1, x_2) &\geq 1, \\ g^{(2)}(x_1, x_2) &\leq [g^{(2)}(x_1, x_1)g^{(2)}(x_2, x_2)]^{1/2}. \end{aligned} \tag{4.3}$$

If we consider the probability of photoelectron registration after a photon is absorbed at the detector, in an increment of an area  $\Delta A$ , and time increment  $\Delta T$ , around time-space point  $x$ , it would be described as  $\eta G^{(1)}(x, x) \Delta A \Delta T = \eta \langle I(x) \rangle \Delta A \Delta T$  (138),

where  $\eta$  represent the detector quantum efficiency. Furthermore, the probability of a two photo event joint detection at points  $x_1$  and  $x_2$  would be described as  $\eta^2 G^{(2)}(x, x)(\Delta A \Delta T)^2$ . Then the  $g^{(2)}(x_1, x_2)$ , as the normalized intensity correlation function, represents the probability of joint photoevent detection in point  $x_1$  and  $x_2$ , normalised by the marginal probabilities of a single event occurring in either  $x_1$  or  $x_2$ . The  $x_1$  and  $x_2$  being space-time points, function  $g^{(2)}(\mathbf{r}_1, \mathbf{t}, \mathbf{r}_2, \mathbf{t} + \tau)$  can be measured with the two photodetectors in places  $\mathbf{r}_1$  and  $\mathbf{r}_2$  with the  $\tau$  delayed coincidence counting of photoelectrons.

The mean photon number, and the variance, can be calculated through relations derived by L. Mandel (139) and B. Saleh (137) and expressed through  $g^{(1)}$  and  $g^{(2)}$  in the following order:

$$\begin{aligned} \langle n \rangle &= \eta \int_D G^{(1)}(x, x) dx, \\ \text{Var}(n) &= \langle n \rangle + \langle n \rangle^2 [g^{(2)}(x, x) - 1]. \end{aligned} \quad (4.4)$$

The probability distribution of photon detection for the classical coherent light if given by a Poissonian distribution with the following equation:

$$p(n) = \frac{\langle n \rangle^n \exp(-\langle n \rangle)}{n!}, \quad (4.5)$$

with fluctuation variance equal to mean photon number  $\text{Var}(n) = \langle n \rangle$ . This is a feature of a commonly used source of coherent light, the laser, above lasing threshold. Here, we have assumed that the measurement time-spatial domain  $\mathbf{D}$  is sufficiently small to support  $\langle n \rangle = \eta AT \langle I(x) \rangle$ . Here  $\mathbf{D}$  is the domain of integration for the total energy collected by the detector and lies within the boundaries of  $t \in [0, T], r \in A$  and bears technical limitations of measuring apparatus. An important characteristic of the light source, stems from the relation between the mean photon number and its variance, called the Fano factor:

$$F_n(\mathbf{D}) = \frac{\text{Var}(n)}{\langle n \rangle}. \quad (4.6)$$

For coherent light  $F_n(\mathbf{D}) = 1$ , but when the intensity fluctuations rise, and the variance becomes  $\text{Var}(n) > \langle n \rangle$ , then the  $F_n(\mathbf{D}) > 1$ , and light is said to have super-

Poissonian statistics. Analogously, with  $Var(n) < \langle n \rangle$ , the  $F_n(\mathbf{D}) < 1$ , and light has sub-Poissonian statistics - a state which cannot be true within the framework of semiclassical theory (137; 139). However, this relation is admitted in the quantum theory of light. The Fano factor is shown to be related to the normalised coincidence rate  $g^{(2)}(x_1, x_2)$  in a following manner:

$$F_n(\mathbf{D}) - 1 = \frac{\langle n \rangle}{D^2} \int_D \int_D [g^{(2)}(x_1, x_2) - 1] dx_1 dx_2 \quad (4.7)$$

### 4.1.2 Non-classical photon statistics

The quantum theory of coherence treats both the photons and the interaction of the photons and detectors in a quantum sense. Now, the description of the photon has positive and negative positive and negative frequency parts of field operators  $\hat{E}^+(\mathbf{x})$  and  $\hat{E}^-(\mathbf{x})$ , when describing the amplitude and intensity correlation functions (135; 134). The first- and second-order coherence functions correspond to the expectation values

$$\begin{aligned} G^{(1)}(x_1, x_2) &= Tr\{\hat{\rho}\hat{E}^+(x_1)\hat{E}^-(x_2)\}, \\ G^{(2)}(x_1, x_2) &= Tr\{\hat{\rho}\hat{E}^-(x_1)\hat{E}^-(x_2)\hat{E}^+(x_2)\hat{E}^+(x_1)\} \end{aligned} \quad (4.8)$$

where  $\hat{\rho}$  is the field density operator. The more common normalised functions  $g^{(1)}(x_1, x_2)$  and  $g^{(2)}(x_1, x_2)$  are derived similarly to their classical counterparts. The probability distribution of photoelectron counts collected within the space-time domain  $\mathbf{D}$  in this frameworks is described as

$$p(n) = \langle : \frac{\hat{W}^n \exp(-\hat{W})}{n!} : \rangle \quad (4.9)$$

where

$$\hat{W} = \eta \int_D \hat{E}^-(x)\hat{E}^+(x)dx \quad (4.10)$$

Here,  $: :$  denotes normal and time ordering. The mean photon number as well as the Fano factor can be calculated from the coherence functions similarly to the semiclassical approach, shown in equations 4.4 and 4.7.

The difference between the correlation functions emergent from the two schools of theoretical approaches lies in the procedure of calculation and the physical interpretation. In semiclassical theory the  $g^{(2)}(x_1, x_2)$  characterises the normalised coincidence rate for joint photoevent at  $x_1$  and  $x_2$ . Yet, in the framework of quantum theory, it is no longer defined as a normalised statistical intensity correlation function. Thus, it is no longer limited by the classical constraints of equation 4.3, and can dip below unity, identifying the presence of the photon anti-bunching effect. However, the correlation function still has to be non-negative at all points (135).

## 4.2 Second-order correlation of condensate

The coherence properties of a light source is a crucial characteristic, which determines its applicability. Since the 1980s there has been pioneering work in strongly coupled microcavities, which led to the appearance of polariton condensation in a variety of different systems, with electrical and optical methods of excitation. One of the first indications of the phase transition from a classical thermal state, to a quantum-mechanical pure state of exciton-polaritons was observed in a GaAs multiple quantum well microcavity, from the decrease of the second-order coherence function (140), followed by a measurement of the second-order coherence function in a CdTe-based microcavity (141). These works, demonstrated the diversity of the obtained results, for example, the decrease of photon bunching as a function of excitation pump power in the former case, or the initial decrease and eventual growth of the bunching in the latter case, pointed towards the richness of light-matter physics. Much of the following research was aimed towards harnessing the coherence properties and photon statistics of polaritonic systems.

It is necessary to discuss here the peculiarities of different methods that have been used in order to obtain a full picture of polariton condensate second-order coherence.

Let us first look at the temporal properties of the excitation source. The correlation functions obtained from pulsed and continuous wave (CW) excitation lasers are very different. When pulsed excitation is applied, the time resolution of the modern

TCSPC detection scheme does not usually play role (unless it is longer than the time between the subsequent excitation laser pulses). The photons are emitted within a small time after pulse arrival, giving much higher coincidence rate compared to CW excitation, thus lowering the acquisition time, and consequently raising signal-to-noise ratio (141; 59). The value  $g^{(2)}(0)$  can be easily extracted from the correlation function obtained with pulsed excitation (39). However, pulsed excitation has its shortcomings as well. When photons emitted from the sample enter the HBT interferometer, they all contribute to the general photon statistics and, importantly, to the correlation value at zero-time delay, regardless of which time they originate from, the condensate build-up, the emission during the condensed state, or from the time after the pulse where the condensate is decaying. These time periods may have different statistical properties (142), which need to be accounted for when evaluating the value of the  $g^{(2)}(0)$  in the HBT scheme. CW excitation, on the other hand, continuously maintains the condensate density during excitation, and only has transient states at the rising/falling edges of a macroscopic time modulation, with, for example, AOM, which only influences the statistics in a minuscule way. Moreover, if the second-order coherence time is greater than the time resolution of detection scheme, with CW excitation, it is still possible to extract the second-order coherence time. Additionally, judging from the best-fit-function of the measured  $g^{(2)}(\tau)$  the emission line broadening mechanisms can be studied, which may be unreachable through usual spectroscopic methods (143).

As was previously discussed in Chapter 3, the profile of the excitation beam, as well as the trapping method, influences the underlying physics of polariton condensation. Besides other measurable manifestations, it reflects in the condensate coherence. Here, let us consider three distinct ways of creating a polariton condensate: excitation of a planar microcavity with a gaussian shaped pump without any confining potential; excitation of an etched microcavity with gaussian shaped pump and with spatial confining potential in the form of a pillar; and lastly, excitation of a planar microcavity with a pump profile in the shape of an annular trap.

In the first and second scenarios, the polariton condensation happens on top of the pumping spot, thus overlapping with the incoherent hot-exciton reservoir, which

leads to faster decoherence. The reported increase of the  $g^{(2)}(0)$  with pump power in planar GaAs- and CdTe-based samples, was also due to the continuous dispersion of polaritons, all of which can contribute to the condensation process and lead to mode competition, unavoidably bringing additional intensity noise and convoluted the coherence. However, if spacial confinement occurs, and it is sufficient to make polaritons condense into a single mode, the decrease of  $g^{(2)}(0)$  towards unity can be observed (60).

In the third case, the incoherent exciton reservoir, as the source of ballistically expanding polaritons, is spatially separated from the region where the condensation occurs. This excitation geometry allows for minimization of the decoherence through interaction with the reservoir (1; 121).

It was previously shown, that for a quasi-resonant excitation of polariton condensates, statistical properties are drastically different when compared to those of non-resonantly pumped condensates (144). The  $g^{(2)}(0)$  appears to be close to unity for the range of powers from below to above condensation threshold in a etched cavity pillar structure, whilst for the planar microcavity, the  $g^{(2)}(0)$  reaches values as high as 1.75 at condensation threshold, with rapid decrease to unity at higher powers.

Yet another degree of freedom that requires consideration is excitation polarization. As was discussed in the Section 3.2.3, for implemented methods of creating polariton condensates, (and was not discussed but mentioned for many other methods of condensate excitation), the pump polarization plays a crucial role in condensate formation. In the work of Sala et.al. (62), it was shown that whilst the polariton laser presents a degree of second-order coherence close to unity, the individual polarisation components might possess different photon statistics.

Using methods of correlated photon counting, the signs of a polariton blockade was recently shown for the cavity-polaritons in the semiconductor microstructures (145) and fiber-cavity polaritons (146). As authors claim, if the interaction-induced energy shift is larger than the polariton linewidth within the highly confined potential, then the system is said to be in the polariton blockade regime, manifesting itself as photon anti-bunching effect, lowering of  $g^{(2)}(\tau)$  function val-

ues for delays  $\tau$  smaller than the polariton lifetime. This modest demonstration of quantum correlations, demonstrates the possibility for polaritonic system to exhibit pure quantum behaviors.

### 4.2.1 Hanbury-Brown and Twiss interferometry of trapped polariton condensate

The scheme for the second-order coherence measurements and the full polarization tomography on photon correlations in a spinor exciton-polariton condensate is shown in Figure 4-1. The classic HBT interferometer, Figure 4-1 (a), was built to record the condensate second-order coherence function. The operation of the intensity interferometer is based on the same principal that was discussed in Section 2.1, but instead of a "start" (or "stop") electric trigger signal from the laser, a photon detection on another single photon avalanche diode (SPAD) is utilized. As such, the light emitted from the condensate goes through the detection scheme, and gets split on the 50:50 BS. Photons arriving into the BS have the same probability to be transmitted or reflected. SPADs are positioned in the reflected and transmitted paths and when a photon is detected, send an electrical pulse and, with use of the time-correlated single photon counting (TCSPC) electronics, the coincidence counting was realized. This way, the joint detection of the photon arrival on the SPADs can be plotted versus the delay time.

In order to record the photon statistics of spinor polarization projections, an advanced scheme was devised. With the replacement of the 50:50 BS with the polarizing BS (PBS), and inserting a pre-aligned HWP or QWP before the PBS, the separation between *horizontal/vertical*, *diagonal/anti-diagonal* and *right circular/left circular* polarization projections respectively can be achieved, and intensity correlations for different polarization projections were measured, as schematically presented in Figure 4-1(b). Correlators 1 and 2 are used to count time resolved coincidences of joint photon detection for pair-orthogonal spinor projections of the polariton condensate, whilst correlator 3 is utilized for the simultaneous cross-correlation measurements between the projections.

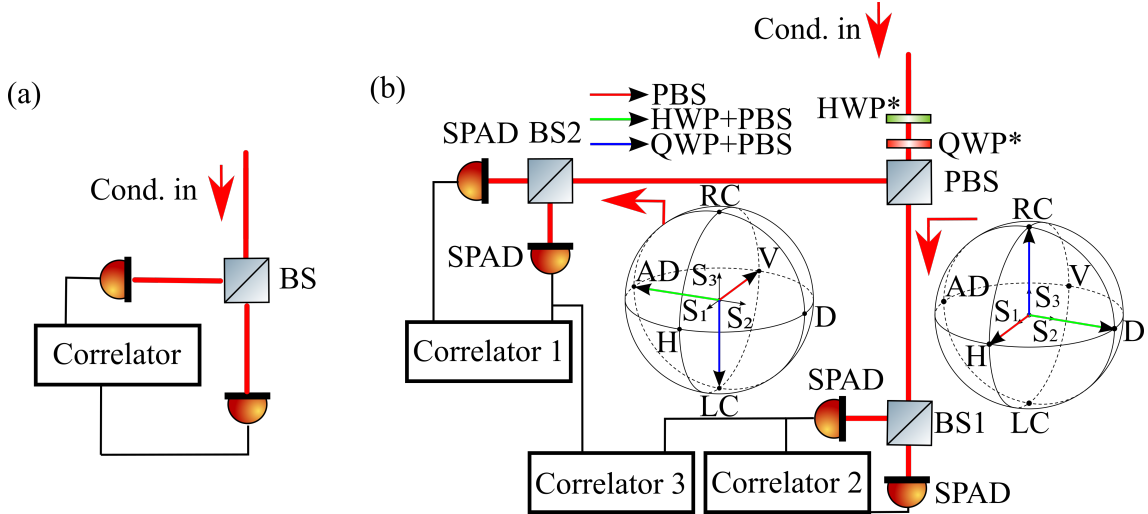


Figure 4-1: (a) Simple scheme of HBT interferometer to measure second-order coherence function of the confined polariton condensate. (b) Triple HBT interferometer setup for polarization resolved intensity correlation of pseudo-spin projection measurements as well as cross-correlation measurement.

As the condensate forms in the center of the optical trap its overlap with the photoexcited reservoir of uncondensed excitons is minimized, see bottom panel of Figure 4-2(a). During the experiments, the statistical information of the Stokes vector  $\mathbf{S} = (S_1, S_2, S_3)$  was extracted, which correspond to the horizontal-vertical ( $S_1$ ), diagonal-antidiagonal ( $S_2$ ), and right-, left-hand circular ( $S_3$ ) polarization of the emitted cavity light, as presented in Figure 4-2(b). Orthogonal polarisation components are mapped on the different pseudospin projections of the polariton condensate and defined as,

$$\mathbf{S} = \frac{1}{2} \Psi^\dagger \boldsymbol{\sigma} \Psi, \quad (4.11)$$

with  $\boldsymbol{\sigma}$  being the Pauli matrix vector. A polarization resolving Hanbury-Brown-Twiss (HBT) intensity interferometer ( $\mathcal{I}_i$ ) enables direct measurement of second-order photon auto- and cross-correlation functions,

$$g_{i,j}^{(2)}(\tau) = \frac{\langle a_i^\dagger(t) a_j^\dagger(t+\tau) a_j(t+\tau) a_i(t) \rangle}{\langle a_i^\dagger(t) a_i(t) \rangle \langle a_j^\dagger(t+\tau) a_j(t+\tau) \rangle}, \quad (4.12)$$

where  $a_i^\dagger$  and  $a_i$  are the photon creation and annihilation operators for given polar-

izations  $i, j$  denoted horizontal (H), vertical (V); diagonal (D), antidiagonal (AD); and left-circular (LC), right-circular (RC), and  $\tau$  is the time-delay between photon detection events. The angled brackets  $\langle \cdot \rangle$  indicate time-average over millions of condensate realizations (i.e., the system is ergodic). In the following, we have implemented a polarization-resolving multi-channel HBT intensity interferometer to measure second-order auto- and cross-correlations between the pseudospin projections, as schematically illustrated in Figure 4-2(c).

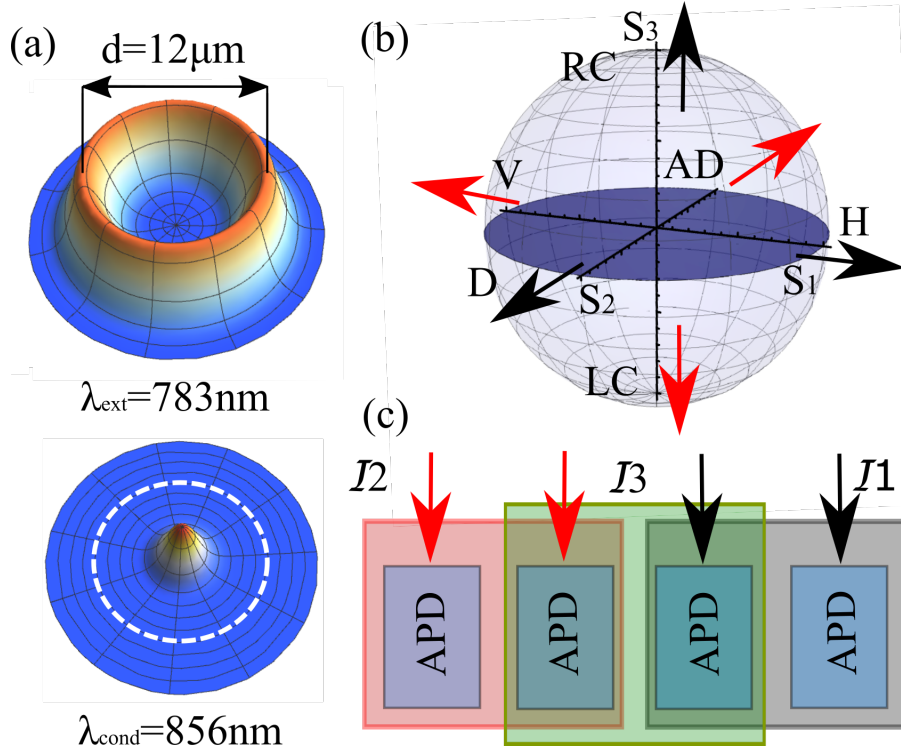


Figure 4-2: (a) Schematic presentation of the annular optical trap (upper panel) and condensate emission (lower panel). White dashed line outlines the optical trap. (b) Poincaré sphere showing three sets of the condensate pseudospin projections onto Stokes vectors. (c) HBT interferometers  $\mathcal{I}_1$  (black box) and  $\mathcal{I}_2$  (red box) are dedicated to measure intensity auto-correlation for orthogonal pseudospin projections indicated by black and red arrows respectively (e.g.  $\mathcal{I}_1$  measures  $g_{h,h}^{(2)}(\tau)$  and  $\mathcal{I}_2$  measures  $g_{v,v}^{(2)}(\tau)$ ). At the same time  $\mathcal{I}_3$  (green box) measures cross-correlation between these projections (i.e.  $g_{h,v}^{(2)}(\tau)$ ).

### 4.2.2 Pseudospin projection photon bunching

As a logical first step stemming from the known literature, the second-order coherence  $g^{(2)}(0)$  of a CW pumped, optically trapped polariton condensate was measured.

Figure 4-3(a) shows the second-order correlation function in the absence of polarization filtering, at the condensation threshold ( $P = P_{th}$ ), and above threshold ( $P = 1.31P_{th}$ ) for horizontally polarized excitation. We can see a small photon bunching  $g^{(2)}(0) \approx 1.04$  at threshold, with  $\tau_c = 220$  ps second-order correlation time derived from a Gaussian fit to the data, (blue line). Increasing the excitation density above condensation threshold drives the condensate towards a highly coherent state as evidenced by the disappearance of photon bunching on top of the shot noise level,  $g^{(2)}(0) \simeq 1$ , in agreement with previous studies (141; 39; 147). For the condensate in the ground state of the optical trap any measurable deviations from the coherent state with increasing pump power up to  $3.5P_{th}$  were not observed. Similarly, the tuning of the excitation polarization had no major effect on the photon statistics, with it staying highly coherent above the threshold with only a slight photon bunching at the threshold.

Further on, as described above the polarisation filtering was used to detect the photon statistics of the Stokes parameters. For pumping levels above condensation threshold, wherein the polariton condensate is, as was established, highly coherent,  $1.31P_{th}$ , the polarisation filtered photon statistics on the circular components,  $S_3$ , for both co-, and cross-circular detection, is Poissonian as shown in Figure 4-3(b). However, the  $S_{1,2}$  projections obey super-Poisson photon distribution,  $g_{i,i}^{(2)}(0) > 1$ , as shown for different linear polarization components in Figure 4-3(c,d). This excess noise is attributed to a random orientation of the condensate pseudospin in the equatorial plane of the Poincaré sphere, due to the spontaneous breaking of the U(1) symmetry (148; 149; 58) from realization to realization. Moreover, with no additional mechanism distinguishing between different linear polarizations of the pseudospin one can intuitively expect it to be walking randomly in the equatorial plane due to polariton-polariton interactions (150), which would lead to equal bunching amplitudes for all linear polarisations.

The observation of unequal bunching between the linear polarisation components is attributed to structural disorder induced birefringence in the microcavity, which breaks the planar symmetry (151). This leads to a linear polarization energy splitting analogous to an in-plane effective magnetic field,  $\mathbf{\Omega}_{\parallel}(\mathbf{r}) = (\Omega_x, \Omega_y)^T$ , that varies

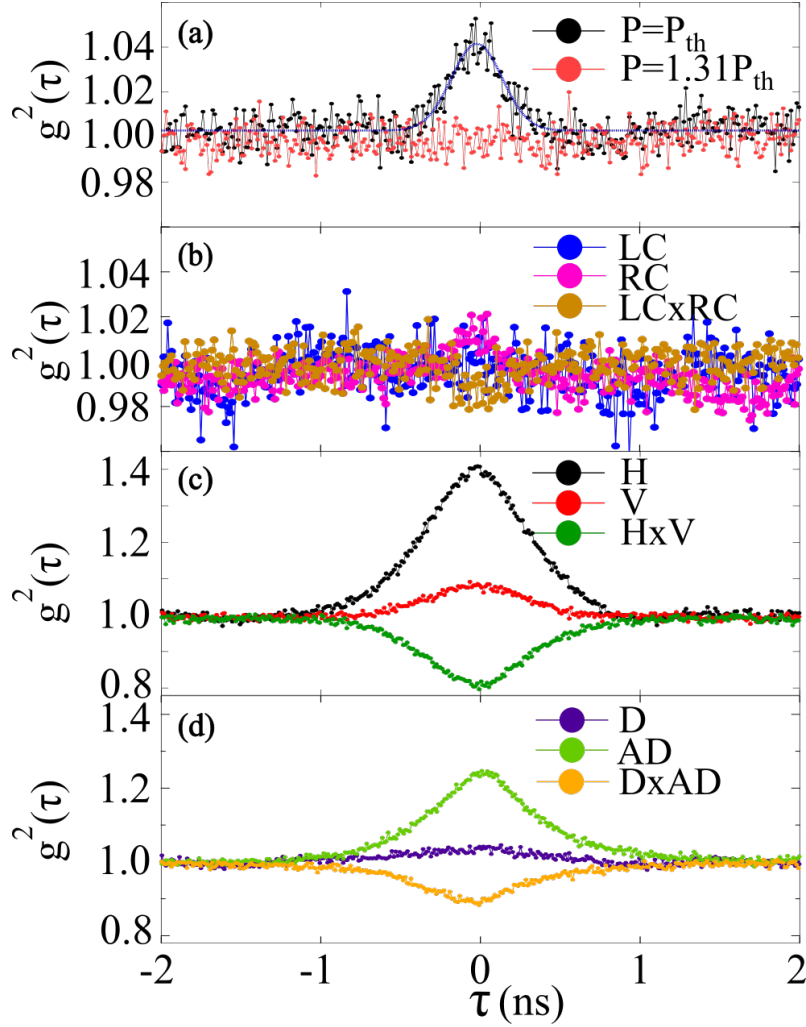


Figure 4-3: (a) second-order correlation function of the condensate, measured without polarization filtering at  $P = P_{th}$  and  $P = 1.31P_{th}$ . Blue line is a Gaussian fit. (b-d)  $g_{i,i}^{(2)}(\tau)$ ,  $g_{j,j}^{(2)}(\tau)$ , and  $g_{i,j}^{(2)}(\tau)$  at  $P = 1.31P_{th}$  for LC-RC, H-V, and D-AD polarizations respectively (letter "x" denoting cross correlation).

randomly across the sample. It was theoretically predicted that polariton-polariton interactions align (pin) the condensate pseudospin parallel to the field (33; 152; 7), which leads to the unequal bunching between the different linear polarizations,  $S_{1,2}$  observed in Figure 4-3(c,d).

Analysis of photon cross-correlations in this *pinned* regime gives important insight into the complex dynamics of the pseudospin. Panels (c,d) in Figure 4-3 reveal anti-correlated photon fluctuations between orthogonal projections. This means that fluctuations in one projection inevitably induce fluctuations in the orthogonal one. Namely, the anti-correlated behavior  $g_{i,j}^{(2)}(0) < 1$  corresponds to temporal

switching of the pseudospin direction in the equatorial plane from being parallel to anti-parallel with  $\mathbf{\Omega}_{\parallel}(\mathbf{r})$ . Such switching events can be understood as mode competition between two fixed point attractors in the pseudospin phase space, with the pinned  $\mathbf{S} \parallel \mathbf{\Omega}_{\parallel}$  attractor being much stronger than the anti-parallel  $-\mathbf{S} \parallel \mathbf{\Omega}_{\parallel}$  attractor (153). In later section 4.2.4, we have show that the switching between parallel and anti-parallel alignment of the pseudospin occurs randomly in time. The switching strongly affects the photon statistics of the linearly polarized projections, especially those which are orthogonal to the pinning field. Indeed, we can observe the highest value of  $g_{i,i}^{(2)}(0)$  in Figure 4-3(c,d) for horizontal and anti-diagonal projections. For the chosen sample location, corresponding to the data in Figure 4-3,  $\mathbf{\Omega}_{\parallel}(\mathbf{r})$  causes the pseudospin to become pinned between the diagonal and vertical projections.

These experiments show a significant effect of nonlinear dynamics on the photon statistics, which can be controlled through the power of the optical excitation. Here lets note that the photon auto-correlation  $g_{i,i}^{(2)}(0)$  at zero time delay relates directly to the variance  $\sigma_i^2$  and mean value  $\bar{n}_i$  of the photon distribution according to

$$g_{i,i}^{(2)}(0) = 1 + \frac{\sigma_i^2 - \bar{n}_i}{\bar{n}_i^2}. \quad (4.13)$$

Figure 4-4(a) shows that with increasing pump power we can observe an increase of  $g_{H,H}^{(2)}(0)$  (black circles) that corresponds to photon distribution broadening (not shown). While the horizontal component experiences very strong photon number fluctuations with  $g_{H,H}^{(2)}(0) \approx 1.9$  at  $P \approx 1.5P_{th}$ , approximating the statistics of thermal light,  $g^{(2)}(0) = 2$ , the vertical component is in a highly coherent state,  $g_{V,V}^{(2)}(0) \approx 1.02$ , as shown by the red circles of Figure 4-4(a). This dependence originates from the large difference in populations between H and V projections and the stochastic switching of the pseudospin, as schematically shown in Figure 4-4(b). The interdependence of the H and V projections is evidenced by their cross-correlation measurement,  $g_{H,V}^{(2)}(0)$ , which exhibits an anti-correlation with the V projection, as shown by the green circles of Figure 4-4(a).

Evolution of the pseudospin and corresponding intensity fluctuations are quali-

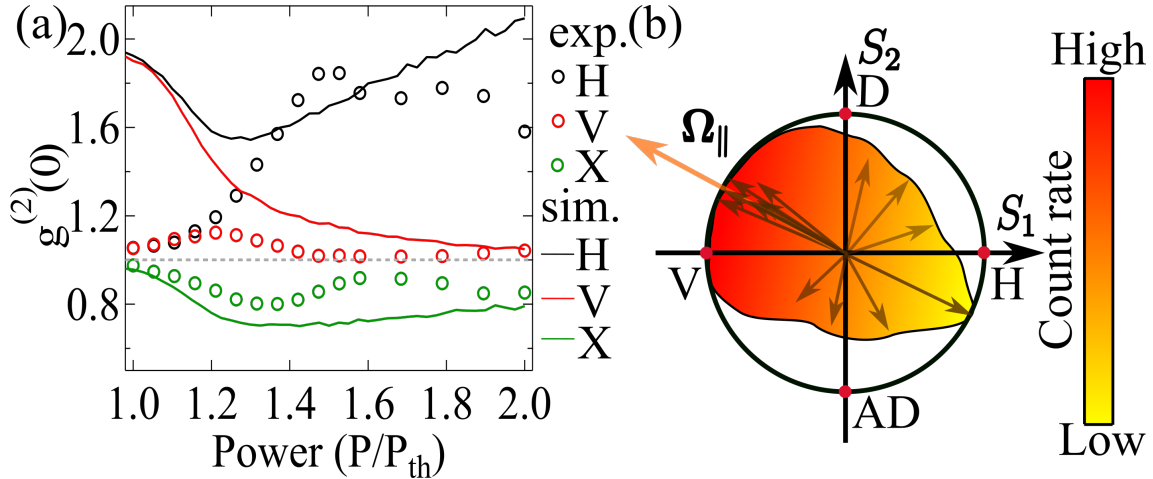


Figure 4-4: (a) Measured (circles) and theoretical (solid lines)  $g_{H,H}^{(2)}(0)$  (black),  $g_{V,V}^{(2)}(0)$  (red) and  $g_{H,V}^{(2)}(0)$  (green) power dependencies for linearly polarized excitation. Error bars for the experimental data are smaller than the size of the circled markers. (b) Schematic representation of the in-plane magnetic field (orange arrow denoted as  $\Omega_{\parallel}$ ) and the polarization of different photon occurrences (black transparent arrows). When pinned, the pseudospin is dominantly orientated parallel  $\Omega_{\parallel}$  (indicated by big number of co-oriented arrows) whereas random *switching* events change the pseudospin to anti-parallel direction (indicated as few anti-parallel arrows), corresponding to anticorrelated event between linear polarization components. Color scale represents total correlation photon count rate.

tatively reproduced by a stochastic generalized Gross-Pitaevskii mean-field model in the truncated Wigner approximation (154; 33) as shown with solid lines in Figure 4-4(a). Note that near the condensation threshold, where time resolution severely limits correlation measurements, such standard mean-field theories fail to describe high-order correlations (155; 156). At higher powers the calculated  $g_{H,H}^{(2)}(0)$  exceeds the experimental values due to the monotonic increase of the vertically polarized condensate population. This overestimation in modeling can be countered by including small polarization ellipticity in the beam as detailed in a later section.

### 4.2.3 Self-induced Larmor precession

In this section, we will see the results of investigation into how the pseudospin dynamics under elliptically polarized pumping affect the photon statistics. In this case, the exciton reservoir which provides gain to the condensate becomes spin-imbalanced (optically oriented) and follows the laser circular polarization to some

degree. The stimulated nature of polariton scattering into the condensate preserves the exciton spin resulting in a condensate that is co-circularly polarized with the laser (157; 158). Due to strong anisotropic particle interactions, such spin population imbalance in both the condensate and the reservoir results in a nonlinear effective out-of-plane magnetic field  $\mathbf{\Omega}_\perp = \Omega_z \hat{\mathbf{z}}$  that gives rise to self-induced Larmor precession (159; 160; 161; 150; 162; 163) driving self-sustained periodic orbitals in the dynamical equations of motion. This field can be written as  $\Omega_z \propto \alpha S_3 + g(X_+ - X_-)$ , where  $\alpha$  denotes the polariton-polariton interaction strength,  $g$  the polariton-exciton interaction strength, and  $X_\pm$  are the exciton reservoir spin populations. Excitation of the reservoirs in the unbalanced fashion, with elliptically polarized pumping, provides more gain to one of the spins, and effectively splits the energy of the system for  $\sigma_\pm$ , as if there is an effective magnetic field present. The sign and the magnitude of  $\Omega_z$  can be controlled through the polarisation ellipticity  $\epsilon$  of the pump laser (164; 7).

Figure 4-5 shows  $g_{H,H}^{(2)}(\tau)$  at  $P = 3.5P_{th}$  for excitation polarization ellipticity varying from 0 (top) to 0.361 (bottom). Under linearly polarized excitation ( $\epsilon = 0$ ) horizontal pseudospin projection gives  $g_{H,H}^{(2)}(0) \approx 2.4$  with correlation time  $\tau_c = 9.2$  ns. We would like to point out that the data presented in Figure 4-5 was obtained at a different sample location than those in Figs. 4-3 and 4-4, which results to quantitative differences due to different strengths and direction of the effective fields  $\mathbf{\Omega}_\parallel(\mathbf{r}_1) \neq \mathbf{\Omega}_\parallel(\mathbf{r}_2)$ . For ellipticities  $\epsilon \geq 0.021$  we have observed an oscillatory behavior in the photon correlations, evidencing the self-sustained Larmor precession of the pseudospin due to the combined effects of the nonlinear field  $\mathbf{\Omega}_\perp$  and the linear birefringent field  $\mathbf{\Omega}_\parallel$ . The Larmor precession drives harmonic photon number oscillations between the orthogonal components in antiphase, which is evidenced by the photon cross-correlations  $g_{H,V}^{(2)}$  in the bottom panel of Figure 4-6(a). To illustrate these dynamics, the simulation of the condensate pseudospin trajectories for the case of  $\epsilon = 0.028$ . Figure 4-6(b) shows the trajectory of the pseudospin on the Poincaré sphere. Assuming that the in-plane birefringent field is weak compared to the out-of-plane field (i.e.,  $|\mathbf{\Omega}_\perp| > |\mathbf{\Omega}_\parallel|$ ) the precession frequency of the pseudospin is approximately dictated by the population imbalance of excitons and polaritons (163). In Figure 4-6(c) we plot the oscillation frequency from  $g_{H,H}^{(2)}(\tau)$

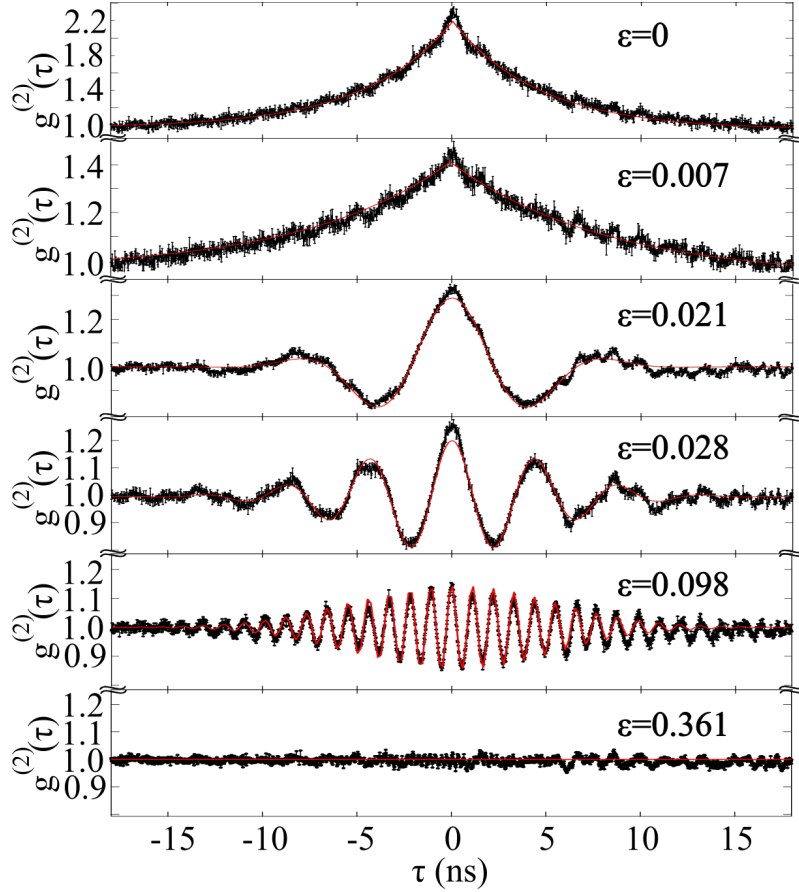


Figure 4-5: Photon statistics engineering with excitation ellipticity.  $g_{H,H}^{(2)}(\tau)$  at pump power  $P = 3.5P_{th}$  for a range of ellipticities  $\epsilon$ . Data for  $\epsilon = 0$  and 0.007 are fitted by an exponential function (red line)  $g_{H,H}^{(2)}(\tau) = 1 + (g_{H,H}^{(2)}(0) - 1)e^{-2|\tau|/\tau_c}$ , data for higher ellipticity are fitted with a product of a Gaussian function and a cosine function  $g_{H,H}^{(2)}(\tau) = 1 + \cos(\omega\tau)(g_{H,H}^{(2)}(0) - 1)e^{-\pi(\tau/\tau_c)^2}$  where  $\tau_c$  is correlation (i.e., dephasing) time.

and the experimentally measured energy splitting between the two counter-circular polarisation components. Our numerical simulations of the splitting show excellent agreement with the experiment.

While the frequency of the  $g_{H,H}^{(2)}(\tau)$  oscillations is increasing linearly with the pump ellipticity their amplitude drops to zero at high ellipticity as the pseudospin becomes predominantly aligned towards circular projections (i.e.,  $|\mathbf{S}| \approx |S_3|$ ) converging to a stable fixed point solution close to the poles of the Poincaré sphere. Thus, the effective out-of-plane magnetic field  $\mathbf{\Omega}_\perp$  mitigates the role of the in-plane effective field  $\mathbf{\Omega}_\parallel$  leading to the suppression of photon noise in the horizontal projection. Figure 4-5 demonstrates the effect of gradual decrease in  $g_{H,H}^{(2)}(0)$  with

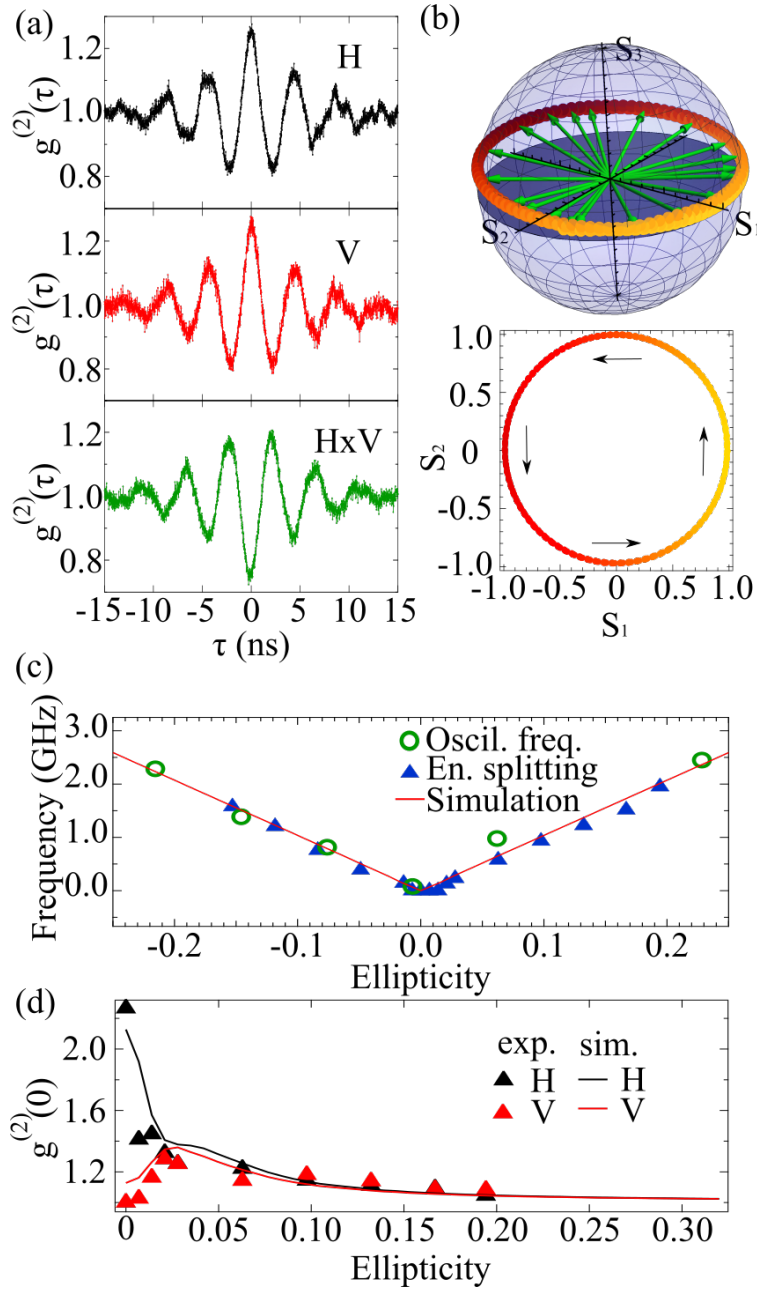


Figure 4-6: (a)  $g_{H,H}^{(2)}(\tau)$  (black),  $g_{V,V}^{(2)}(\tau)$  (red), and  $g_{H,V}^{(2)}(\tau)$  (green) at  $P = 3.5P_{th}$ ,  $\epsilon = 0.028$ . (b) Calculated normalized pseudospin precession trajectory and its projection into equatorial plane of the Poincaré sphere. (c) Oscillation frequency of  $g_{i,j}^{(2)}(\tau)$  (blue triangles) plotted alongside with energy splitting (green circles) between LC and RC polarized condensate. Solid red line represent simulated results. (d) Experimental (triangles) and simulated (solid line)  $g_{H,H}^{(2)}(0)$  (black) and  $g_{V,V}^{(2)}(0)$  (red) for different pump ellipticities.

increasing ellipticity. In Figure 4-6(d) we plot  $g_{H,H}^{(2)}(0)$  and  $g_{V,V}^{(2)}(0)$  and observe that the photon bunching is approaching unity with increasing ellipticity. Therefore a

delicate control over the exciton and polariton spin-imbalance offers a full range of tuneability in photon statistics spanning from super-thermal at  $\epsilon \sim 0$  to super-Poissonian distributions, and highly coherent states at large  $\epsilon > 0.2$ . Lets note here that in the presence of a finite  $|\Omega_{\parallel}|$ , we have always observed the reported behavior of the correlation functions.

As one can imagine, we can manipulate the exciton reservoir spin population  $X_{\pm}$  not only by changing the pump ellipticity, but also by varying the excitation pump power. With increasing pump density the discrepancy between reservoir population becomes gradually more significant even in the case of slight ellipticity of pump polarization. This effect leads to an increase of the effective out-of-plane magnetic field  $\Omega_{\perp}$  and acceleration of Larmor precessions as evidenced in Fig 4-7. Here, with a set initial pump polarization ellipticity, we can observe the change of correlation function oscillation frequency with excitation density.

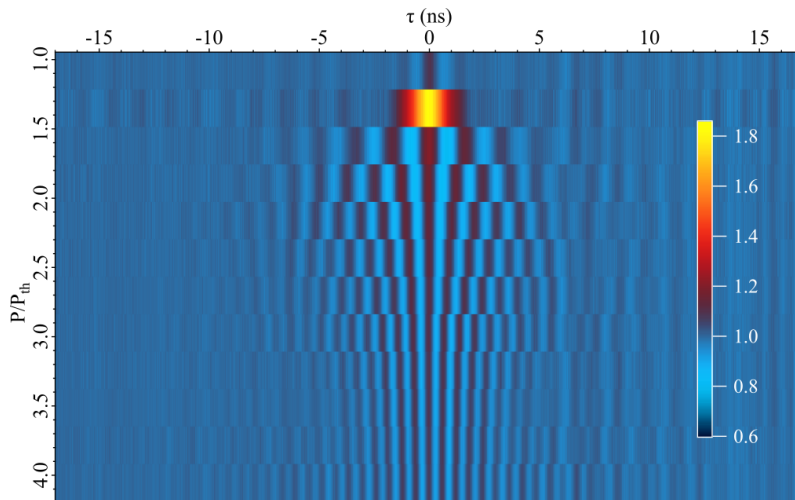


Figure 4-7: Condensate  $g_{H,H}^{(2)}(0)$  with the respect to excitation power. With the presence of small ellipticity, the imbalance between the reservoirs becomes higher with increasing pump power, giving rise to accelerating precessions.

#### 4.2.4 Polarization switching and pinning

In Figure 4-8 we have shown the polarization resolved  $1 \mu s$  long time series of condensate emission at  $P = 1.6P_{th}$ . While the mean condensate polarization is dominantly pinned to the vertical projection, we have observed abrupt and completely random in time condensate emission polarization switching events (indicated by green shaded

areas). This type of behavior is present in many instances (not shown here) and the number of switching events is random within the pulse.

As discussed before, emergence of finite cavity birefringence and the effective in-plane magnetic field  $\Omega_{\parallel}$  is location sensitive. Hence, in Figure 4-9 we have presented  $g_{H,H}^{(2)}(\tau)$ ,  $g_{V,V}^{(2)}(\tau)$  and  $g_{H,V}^{(2)}(\tau)$  data taken from the different point on the sample at  $P = 1.48P_{th}$ . One may notice that the amplitude of the bunching,  $g_{i,i}^{(2)}(0)$ , is different from what is presented in the Figure 4-4(a) for the same power. In Figure 4-10(a) we have shown power dependence for the  $g_{H,H}^{(2)}(0)$  and  $g_{V,V}^{(2)}(0)$ , similar to what we have presented in Figure 4-4(a). We would note here that the measurements in Figs. 4-9 and 4-10 are performed at a different sample location than those in Figs. 4-3,4-4 and 4-5,4-6 which is the reason for some quantitative, but not qualitative differences.

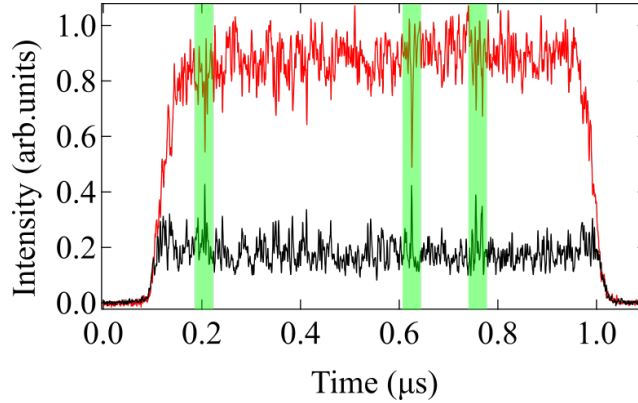


Figure 4-8: Measured time series (1  $\mu\text{s}$  excitation pulse) for condensate H (black) and V (red) polarized emission. Here, we have observed switching (highlighted with pale green rectangles) of intensity between the polarizations which contribute to the large values of  $g_{H,H}^{(2)}(0)$ .

As long as a finite birefringent field exists  $\Omega_{\parallel}$  then one can expect the nonlinearity of the condensate dynamics to pin the pseudospin parallel to this field. The results in Figure 4-10(a) indicate the expected behavior with power, i.e. decrease of  $g_{V,V}^{(2)}(0)$  (red circles) to unity for  $P > 1.35P_{th}$  as more polaritons in the condensate become vertically polarized while  $g_{H,H}^{(2)}(0)$  (black circles) increases. Imposed onto the plot, in green triangles, is the  $S_1$  Stokes component power dependence which shows how one of the polarizations (vertical, in our case) becomes dominant in the system. From the measured DOP in Figure 4-10(b) we can see that the emitted condensate light, right after the condensation threshold, is unpolarized and starts to become polarized

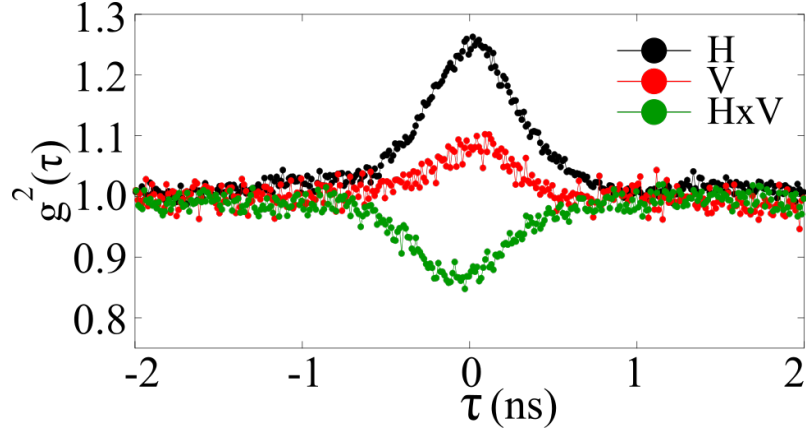


Figure 4-9: Second-order correlation function of the condensate, measured with polarization filtering at  $P = 1.48P_{th}$ .  $g_{H,H}^{(2)}(\tau)$  (black),  $g_{V,V}^{(2)}(\tau)$  (red), and  $g_{H,V}^{(2)}(\tau)$  (green).

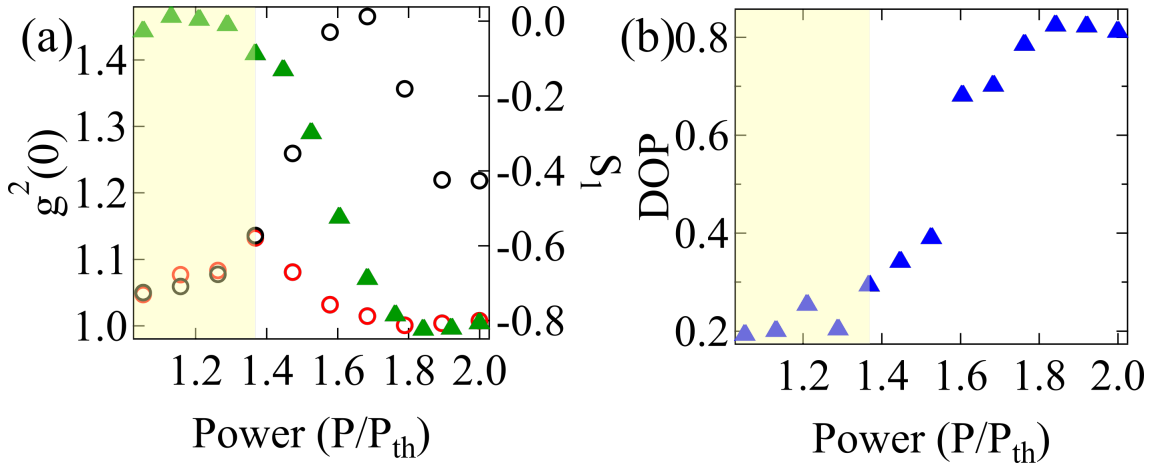


Figure 4-10: (a) Experimentally measured  $g_{H,H}^{(2)}(0)$  (black circles) and  $g_{V,V}^{(2)}(0)$  (red circles) power dependence and corresponding time-integrated  $S_1$  component (green triangles). (b) Corresponding power dependence of the condensate DOP. Pale yellow background highlights the pump power range without polarization pinning (low DOP).

after  $P = 1.35P_{th}$  when the pinning effect kicks in (7).

#### 4.2.5 Dynamical mean field equations

The dynamics of the spinor polariton condensate order parameter is modeled through a set of stochastic driven-dissipative Gross-Pitaevskii equations (Langevin type equations) coupled to spin-polarized rate equations describing excitonic reservoirs  $X_{\pm}$  feeding the two spin components  $\psi_{\pm}$  of the condensate. The stochastic part of our model ( $\theta_{\pm}$ ) was formulated in Refs. (33; 154) in the truncated Wigner approxima-

tion, which becomes valid above condensation threshold with large particle numbers in the condensate  $\langle n \rangle \gg 1$ , such that stimulated effects dominate over spontaneous scattering events. We would point out that a more accurate treatment of dissipative many-body quantum systems involves writing a density matrix for the polariton field governed by appropriate master equations (165). This approach is beyond the scope of this work where our modeling concerns the limit of large particle numbers, where we show that complex nonlinear mean-field forces have quite dramatic effects on the emitted photon statistics. The model reads:

$$i \frac{d\psi_\sigma}{dt} = \frac{1}{2} \left[ \nu V_\sigma + i (R_1 X_\sigma + R_2 X_{-\sigma} - \Gamma) \right] \psi_\sigma - \nu \frac{\Omega_x}{2} \psi_{-\sigma} + \theta_\sigma(t), \quad (4.14a)$$

$$\frac{dX_\sigma}{dt} = - \left[ \Gamma_R + R_1 (|\psi_\sigma|^2 + 1) + R_2 (|\psi_{-\sigma}|^2 + 1) \right] X_\sigma + \Gamma_s (X_{-\sigma} - X_\sigma) + P_\sigma, \quad (4.14b)$$

$$V_\sigma = \alpha_1 |\psi_\sigma|^2 + \alpha_2 |\psi_{-\sigma}|^2 + g_1 \left( X_\sigma + \frac{P_\sigma}{W} \right) + g_2 \left( X_{-\sigma} + \frac{P_{-\sigma}}{W} \right). \quad (4.14c)$$

Here,  $\sigma \in \{+, -\}$  are the two spin indices,  $\alpha_{1,2}$  denotes the same-spin (triplet) and opposite-spin (singlet) polariton-polariton interaction strengths and  $g_{1,2}$  are the corresponding interactions with the reservoir,  $R_{1,2}$  is the rate of stimulated same-spin and opposite-spin scattering of polaritons into the condensate, and  $\Gamma$  is the polariton decay rate,  $\Gamma_R$  and  $\Gamma_s$  describe the decay rate and spin relaxation of reservoir excitons. In principle, scattering from the reservoirs to the condensate should be dominantly spin-preserving ( $R_1$ ) but in the presence of a (effective) magnetic field ( $\Omega_x$ ) one needs to account for the possibility that particles from the opposite-spin reservoir can scatter ( $R_2$ ) into the condensate (150; 166). Some studies work under the approximation that in optical traps the condensate is so well separated from the background reservoir and that blueshift coming from polariton-exciton interactions can be discarded, but recent studies (167) have shown that the reservoir is actually not so distant from the condensate and therefore additional polariton condensate blueshift coming from this background reservoir ( $g_{1,2}$ ) should be taken into account. For all results presented, we have chosen  $\alpha_2 = -0.2\alpha_1$  and  $g_2 = -0.2g_1$  (168). We also include an energy dampening parameter  $\nu = 1 - i\nu'$  according to the Landau-Khalatnikov approach (33). Finally, spin-mixing (spin-relaxation) between the reser-

voirs ( $\Gamma_s$ ) should be taken into account as it can be evidenced as depolarization in the cavity photoluminescence below condensation threshold (169; 170; 58; 164; 171; 172). It is naturally quite challenging to understand the full picture of which parameters contribute to different observed effects in experiment and thus we attempt at being as inclusive as possible of different physical mechanisms.

Although the experiment deals with a birefringent field  $\mathbf{\Omega}_{\parallel} = (\Omega_x, \Omega_y)^T$  at a specific angle we will, without any loss of generality, take the splitting to be between horizontal  $\psi_H = (\psi_+ + \psi_-)/\sqrt{2}$  and vertical  $\psi_V = (\psi_+ - \psi_-)/\sqrt{2}$  polarized modes represented by  $\Omega_x > 0$  and  $\Omega_y = 0$ . The strength of the white complex-valued noise  $\theta_{\sigma}(t)$  is determined by the scattering rate of polaritons into the condensate,

$$\langle \theta_{\sigma}(t)\theta_{\sigma'}(t') \rangle = 0, \quad \langle \theta_{\sigma}(t)\theta_{\sigma'}^*(t') \rangle = \frac{R_1 X_{\sigma} + R_2 X_{-\sigma}}{2} \delta_{\sigma\sigma'} \delta(t - t'). \quad (4.15)$$

The active reservoir  $X_{\sigma}$ , which feeds the condensate with particles, is driven by a background of high momentum *inactive* excitons  $P_{\sigma}$  which do not satisfy energy-momentum conservation rules to scatter into the condensate. Assuming the simplest type of rate equation describing the conversion of optical excitation power into an inactive reservoir in the continuous wave regime we write:

$$\frac{dP_{\sigma}}{dt} = -(W + \Gamma_I)P_{\sigma} + \Gamma_s(P_{-\sigma} - P_{\sigma}) + L_{\sigma}. \quad (4.16)$$

Here,  $W$  is a phenomenological spin-conserving redistribution rate of inactive excitons into active excitons and  $\Gamma_I$  is the nonradiative exciton decay rate. Since these inactive excitons also experience spin relaxation  $\Gamma_s$  the polarization of  $P_{\sigma}$  will not coincide with that of the incident optical excitation. As the experiment is performed in the continuous-wave regime we can immediately solve the steady state solution of Eq. (4.16) and plug it into Eqs. (4.14). For optical excitation parameterized as  $\mathbf{L} = L(\cos^2(\Theta), \sin^2(\Theta))^T$  where  $L$  is the power of the optical excitation and  $\Theta$  can be understood as a quarter waveplate angle in the experimental setup which determines the polarization of the incident light, since depending on the QWP orientation the polarisation ellipticity of the excitation beam can be tuned, effectively changing the pumping power for  $X_{\sigma}$  reservoirs, we can write the background inactive reservoir

as,

$$\begin{pmatrix} P_+ \\ P_- \end{pmatrix} = \frac{L}{W + 2\Gamma_s} \begin{pmatrix} W \cos^2(\Theta) + \Gamma_s \\ W \sin^2(\Theta) + \Gamma_s \end{pmatrix}. \quad (4.17)$$

Here, we have neglected  $\Gamma_I$  since we assume nonradiative losses are much slower than the redistribution rate of excitons  $W \gg \Gamma_I$ .

Determining the parameters of Eq. (4.14) poses a challenge since they will depend in a complicated way on both sample and excitation properties. To overcome this, we implement a random walk algorithm which, in each step, calculates the root-mean-square-error between the data from experiment and simulation. The algorithm starts from a random set of parameters (appropriately bounded to remain physical) and repeatedly takes a random step forward in parameter space which is kept if the error is lowered. If the error rises, the step is discarded (go back to previous step) and a new random step is tested. Performing 500 random initializations in the parameter space, with each taking 300 random steps, we determine a set of parameters best fitting the experimental results. The parameters used throughout the manuscript are given in units of  $\Gamma$  except of  $\nu'$  which is dimensionless:  $\Gamma_R = 1.6$ ;  $\Gamma_s = 0.19$ ;  $W = 0.156$ ;  $R_1 = 0.0032$ ;  $R_2 = 0.0027$ ;  $\alpha_1 = 0.00015$ ;  $g_1 = 0.00097$ ;  $\nu' = 0.077$ . For Figure 4-4(a) and 4-6(c,d) we have set  $\Omega_x = -0.057$  and  $-0.0072$  respectively as they correspond to different sample locations. This set of parameters are of the typical values for our sample, and has been used for our previous works in which they nicely matched the theoretical predictions with the observed experimental results. The theoretical pump threshold value for linearly polarized excitation corresponds to a threshold laser power  $L$  defined as  $P_{th} = P_{\pm}(L_{th})$ ,

$$L_{th} = \frac{2\Gamma\Gamma_R}{R_1 + R_2 + \nu'(g_1 + g_2)(1 + \Gamma_R/W)}. \quad (4.18)$$

*Disclaimer: the author contributed in developing the mathematical model for the simulation discussed above by discussion with the Helgi Sigurdsson and providing experimental data to check the simulation performance.*

### 4.2.6 Influence of residual ellipticity

In this section we investigate the effects of small detrimental ellipticity in the excitation laser, and how it affects our results presented in Figure 4-4. In Figure 4-11(a) we show the calculated zero time delay second-order correlation functions between the linear polarization components (horizontal and vertical specifically) averaged over 100 different realizations of the condensate (i.e., Monte-Carlo sampling) where each realization is integrated over 10 ns. The whole lines are the same as in Figure 4-4(a) corresponding to a linearly polarized excitation  $\Theta = 45^\circ$  whereas the dashed lines represent simulation with a slight ellipticity  $\Theta = 46^\circ$  (or alternatively, QWP angle of  $1^\circ$ ). The circle markers are experimental data. In Figure 4-11(b) we show the corresponding time-integrated pseudospin components. As expected, for a finite ellipticity we see that circular polarization builds up with growing power due to the power-dependent spin imbalance increasing in the reservoirs which provides differential gain and blueshift to the spins  $\psi_\pm$ . The increase of the condensate circular polarization  $S_3$  is accompanied by a decrease in the vertical linear polarization (i.e.,  $S_1$  becomes less negative) which results in reduction of the  $g_{H,H}^{(2)}(0)$  as evident from the black dashed line in Figure 4-11(a).

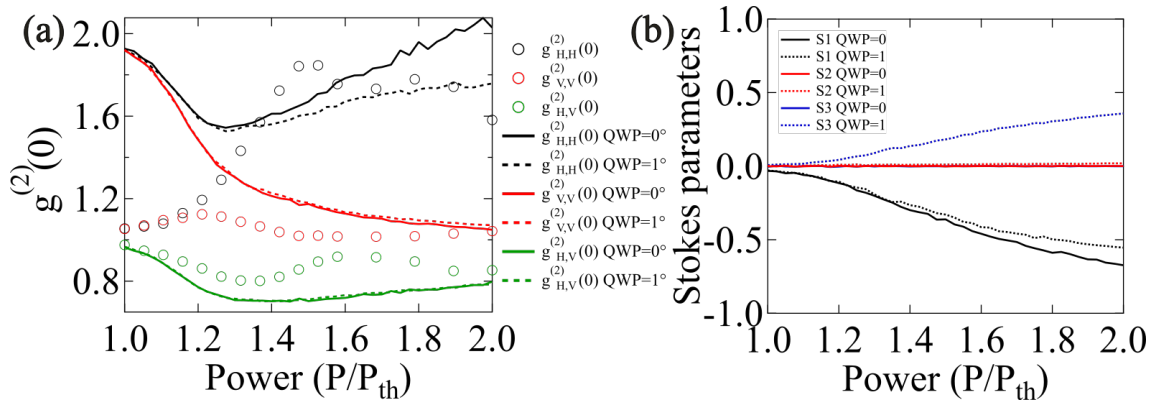


Figure 4-11: (a)  $g_{H,H}^{(2)}(0)$  (black),  $g_{V,V}^{(2)}(0)$  (red) and  $g_{H,V}^{(2)}(0)$  (green) power dependencies. Experimentally measured (circles) and theoretically obtained data with purely linearly polarized excitation (solid line) and with slightly elliptically polarized excitation (dashed line). (b) Theoretically obtained time integrated pseudospin parameters with purely linearly (solid line) polarized excitation and slightly elliptical (dashed line) excitation polarization.

### 4.2.7 Single mode laser vs Polariton condensate

Comparison between the polarization resolved photon statistics of an optically trapped polariton condensate versus a single mode laser (in our case M-squared Ti-Sapphire laser with  $< 50$  kHz linewidth when cavity locked) is a great way to show the principal difference between these light sources. Polarization resolved HBT measurements for light from a single mode laser with horizontal polarization was conducted. The results are shown in Figure 4-12. Above threshold, the total condensate intensity follows Poissonian statistics, see Figure 4-3(a) similar to what is known for single mode lasers. However, when we compare polarization resolved photon statistics of a single mode laser to the condensate statistics presented, we see a clear difference. Photon statistics for the laser do not depend on which polarization basis we resolve it, contrary to the case with the optically trapped polariton condensate. This indicates that the condensate spinor has rich dynamics, whilst single mode laser spinor is stationary.

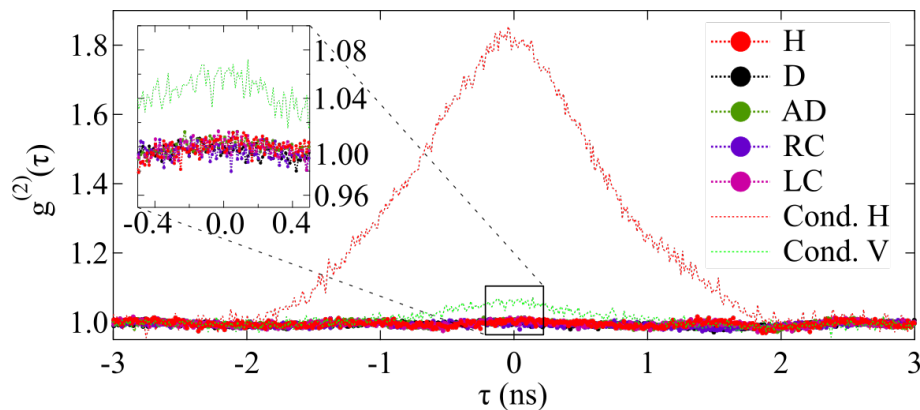


Figure 4-12: Comparison between experimentally measured polarization resolved  $g_{i,i}^{(2)}(\tau)$  for (H - horizontal, V - vertical, D - diagonal, AD - anti-diagonal, RC - right circular, LC - left circular) polarization projections of a horizontally polarized single mode laser (dashed lines with markers). The laser correlation results are compared against the condensate  $g_{H,H}^{(2)}(\tau)$  and  $g_{V,V}^{(2)}(\tau)$  pumped also with a linearly polarized laser at  $P = 1.5P_{th}$  (dashed lines).

### 4.2.8 Effect of the trap geometry

It was found out, that another way to manipulate the photon statistics is to change the optical trapping potential. Furthermore, we can break U(1) symmetry by mak-

ing the optical trap elongated in some direction. If we would avoid sample locations with structural strains, as can be judged by looking at integrated polarimetry measurements, which shows us elevated DOP, and find the place on the sample where the internal strain is small when pumped linearly, meaning that integrated  $DOP \approx 0$ , we can observe the change within the photon statistics by changing the symmetry of the optical trap. Figure 4-13 shows change in the photon statistics  $g_{H,H}^{(2)}(\tau)$ , for traps schematically illustrated in the insets. By mere rotation of the elongated trap, we show control of the photon noise present in the system. The direction of linear polarization seems to follow the minor axis of the elliptical trapping potential. This effect can be caused by photonic TE-TM splitting influencing trapped polaritons, which results in fine splitting in the potential trap transverse modes (2). The developed model describes the effective magnetic field, emerged from TE-TM splitting acting on the polariton pseudospin and for the trap ground state reads as:

$$\mathbf{\Omega}_{\text{trap}} \simeq -\frac{\hbar m |\Delta| \delta\omega}{2} \begin{pmatrix} \cos(2\theta_{\text{min}}) \\ \sin(2\theta_{\text{min}}) \\ 0 \end{pmatrix}. \quad (4.19)$$

Here,  $m$  is polariton effective mass,  $\theta_{\text{min}}$  is the angle of the trap minor axis from the horizontal, and  $\delta\omega = |\omega_x - \omega_y| \propto |a^{-1} - b^{-1}|$  is the absolute difference between the trap oscillator frequencies along the major and the minor axis. It is necessary to point out that the minus sign in Eq. (4.19) is written explicitly because the splitting  $\Delta < 0$  in our sample (173).

### 4.2.9 The correlation function decay curve

The second-order correlation function for the thermal light sources with Lorentzian or Gaussian spectra can be calculated with following equations

$$\begin{aligned} g^{(2)}(\tau) &= 1 + (g^{(2)}(0) - 1)e^{-2\tau/\tau_c}, \\ g^{(2)}(\tau) &= 1 + (g^{(2)}(0) - 1)e^{-\pi(\tau/\tau_c)^2}, \end{aligned} \quad (4.20)$$

where  $\tau_c$  is correlation time. The different shape of the coherence decay function is attributed to the variety of the line broadening mechanisms. In our experiment we

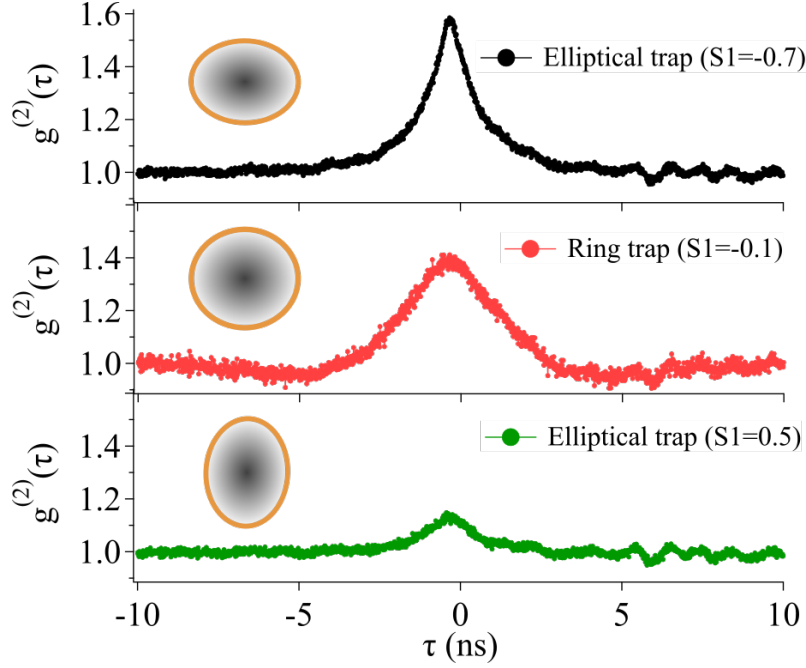


Figure 4-13: Control over the photon statistics by changing the trap geometry. In the middle panel (red)  $g_{H,H}^{(2)}(0)$  when optical potential is a symmetric ring. In the top panel,  $g_{H,H}^{(2)}(0)$  of condensate excited with horizontally elongated optical trap. In the bottom panel,  $g_{H,H}^{(2)}(0)$  trap is rotated orthogonal to the case of the top panel.

observe the transition of second-order coherence function curvature with the respect to pump power, as shown in figure 4-14. Just above condensation threshold  $g^2(\tau)$  decays exponentially with  $\tau_c$ , indicating Lorentzian spectral line shape emission. With increased polariton density, we observe change of the  $g^2(\tau)$  decay to Gaussian. Previous studies (174; 175) describe the transition to a Gaussian decay. With the introduction of a polariton-polariton interaction term, two limiting cases of weakly- and strongly-interacting regimes were described. In weakly-interacting regime used theoretical fit boils down to Schawlow-Townes formula, with exponential decay of  $g^2(\tau)$ . In strongly-interacting regime polariton-polariton interactions along with shot noise of condensate brings in Gaussian broadening into the system (39). In our experiment, we look at  $g_{h,h}^2(\tau)$  for horizontally polarized light, which as previously discussed strongly bunched due to the pinning of vertical component, and the transition to Gaussian decay happens at  $P = 1.135P_{th}$  without bringing a decrease in correlation time for this non-pinned polarization component. In addition, we see resurgence of strictly exponential decay after pump power reaches  $P = 1.4P_{th}$  and

reappearance of Gaussian decay after  $P = 2.43P_{th}$ . The decrease in coherence time happens at around  $P = 1.95P_{th}$  mark, as shown in Figure 4-14(e). The results of the  $\chi^2$  test for the fit certainty is shown in the Figure 4-14(f). The theoretical modeling for this data was not yet done, thus here we present only the results of experimental data analysis.

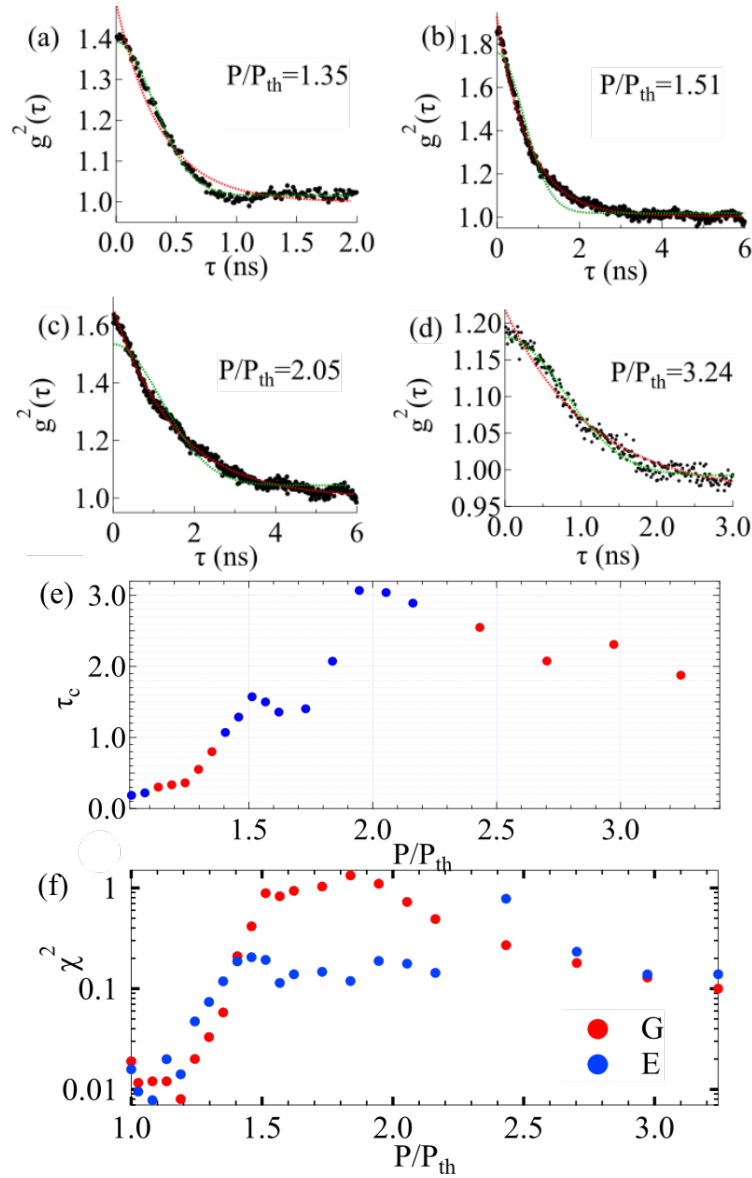


Figure 4-14: (a-d)  $g_{h,h}^2(\tau)$  is fitted with exponential (red) and Gaussian (green) functions for pump powers  $P = 1.35P_{th}$ ,  $P = 1.51P_{th}$ ,  $P = 2.05P_{th}$  and  $P = 3.24P_{th}$  respectively. (e) Correlation time power dependence extracted from  $g_{h,h}^2(\tau)$  function best-fit function. Blue points represent exponential and red points Gaussian fit. (f)  $\chi^2$ -test results to determine the best-fit function.

### 4.2.10 Conclusion

In summary, it was shown that whilst trapped polariton condensate PL above condensation threshold obeys a coherent photon statistics, its spinor projections may demonstrate a statistical bunching of photons. Demonstrated spinor precessions and spontaneous polarization switching regimes depending on the excitation parameters. Influence of the optical trap geometry on the photon statistics is shown as well. The variety of achievable photon statistical regimes encourage to explore the properties of trapped polariton condensate further, bringing us to the next chapter, where we explore Hong-Ou-Mandel effect of such condensates.

# Chapter 5

## Hong-Ou-Mandel effect

A great advance in physics which signaled a new discrete jump in the understanding of nature was the observation of two-photon interference. Although several groups in the late 1980s (176; 177; 178) were competing to prove, arguably, the most quantum phenomena, in the literature, the works of Chung Ki Hong, Zheyu Ou and Leonard Mandels are commonly recognized (179). The essence of their findings can be described as following: if two indistinguishable photons enter a lossless 50:50 beam splitter simultaneously at the two input ports, they will always leave the beam splitter jointly from one, or the other output port. This results in the so-called "HOM dip" in the measured intensity correlation function between the two output ports of the beam splitter.

In this chapter a brief theoretical introduction to the Hong-Ou-Mandel (HOM) effect will be given, followed by a comparison of the effect for non-classical and classical light sources. Next, an outline of the experimental procedure for HOM detection in polariton condensates will be given. Concluding the chapter, we will discuss the observations seen in the experimental data taken for the polariton condensate in the HOM interferometer, in different regimes of photon on statistics.

## 5.1 Theory of Hong-Ou-Mandel effect

### 5.1.1 Beam splitter action

A seemingly simple optical device - the optical beam splitter (BS) - is an essential element for observing the HOM effect. It is a device with two inputs ( $a$  and  $b$ ), and two outputs ( $c$  and  $d$ ). When light enters a BS, it will be split into a transmitted and reflected path, depending on the transmittance  $t$  and reflectance  $r$  complex parameters. Here we should note that a real BS will have some absorption, but for the sake of simplicity we consider it to be lossless here. Taking initially a classical approach, the 50:50 BS, which we are going to consider from now on, has  $|t| = |r| = 1/\sqrt{2}$ . For this type of BS the electric field at output ports  $c$  and  $d$  can be described as with electric field in input ports  $a$  and  $b$ , such that

$$\begin{aligned} E_c &= (E_a + E_b)/\sqrt{2}, \\ E_d &= (E_a - E_b)/\sqrt{2}. \end{aligned} \tag{5.1}$$

Note that here we have a phase relation between transmitted and reflected beam, resulting in  $\pm\pi/2$  phase shift between them, stemming from energy conservation for such optical device.

The quantum description of light passing through the BS is done with bosonic creation and annihilation operators ( $\hat{a}^\dagger$  and  $\hat{a}$ ). These operators obey the commutation relations  $[\hat{a}_i, \hat{a}_j^\dagger] = \delta_{ij}$  and describe the electromagnetic fields in mode  $i$ , where  $\delta_{ij}$  is the Kronecker delta. The creation operator acting on the vacuum in this case can be represented as follows

$$(\hat{a}_i^\dagger)^n |0\rangle = \sqrt{n!} |n\rangle_i. \tag{5.2}$$

Here  $|0\rangle$  and  $|n\rangle_i$  represent the vacuum and  $n$ -photon in mode  $i$  states, respec-

tively. Accordingly, the 50:50 BS action in terms of these operators will be

$$\begin{cases} \hat{a} = \frac{1}{\sqrt{2}}(\hat{c} + \hat{d}) \\ \hat{b} = \frac{1}{\sqrt{2}}(\hat{c} - \hat{d}), \end{cases} \quad (5.3)$$

which is a back transformation in which we present input annihilation operators with output annihilation operators.

### 5.1.2 Two-photon interference

Let's assume two photons enter the system, one at each input of the 50:50 BS, and these photons are distinguishable from each other. The distinguishability may come from various characteristics, such as energy, polarization, temporal incidence, or spacial mode overlap. We can write down the initial state as

$$|\psi_{in}\rangle = |1\rangle_{a,H}|1\rangle_{b,V} = |H\rangle_a|V\rangle_b = \hat{a}_H^\dagger \hat{b}_V^\dagger |0\rangle. \quad (5.4)$$

Here we consider the situation where we have horizontally polarized light present at port  $a$ ,  $|H\rangle_a$  and vertically polarized light at port  $b$ ,  $|V\rangle_b$ . Incorporating this into equation 5.3, we get the following result

$$\hat{a}_H^\dagger \hat{b}_V^\dagger |0\rangle \xrightarrow{\text{BS}} \frac{1}{2}(\hat{c}_H^\dagger + \hat{d}_H^\dagger)(\hat{c}_V^\dagger - \hat{d}_V^\dagger)|0\rangle = \frac{1}{2}(\hat{c}_H^\dagger \hat{c}_V^\dagger - \hat{c}_H^\dagger \hat{d}_V^\dagger + \hat{c}_V^\dagger \hat{d}_H^\dagger - \hat{d}_H^\dagger \hat{d}_V^\dagger)|0\rangle. \quad (5.5)$$

From equation 5.5, an intuitive result is evident, which explains where photons entering from different inputs will exit the system. When both photons leave the BS from the same port pertain to the first and fourth terms, whilst when the two photons exit from different exits corresponds to the second and third terms.

Now when light has the same polarization, for example *Horizontal*. We can rewrite Eq. 5.5 with just index  $H$ , or omit this index completely. The equation now reads

$$\hat{a}^\dagger \hat{b}^\dagger |0\rangle \xrightarrow{\text{BS}} \frac{1}{2} (\hat{c}^\dagger \hat{c}^\dagger - \hat{e}^\dagger \hat{d}^\dagger + \hat{e}^\dagger \hat{d}^\dagger - \hat{d}^\dagger \hat{d}^\dagger) |0\rangle = \frac{1}{\sqrt{2}} (|2\rangle_c - |2\rangle_d). \quad (5.6)$$

This gives destructive interference for the two photons exiting from different ports and constructive interference for them exiting from the same port, and is the essence of the two-photon interference of indistinguishable photons. As a side note, if we run the similar analysis for the fermions, e.g. electrons, , we find that that  $|1\rangle_a |1\rangle_b \xrightarrow{\text{BS}} |1\rangle_c |1\rangle_d$ , meaning that we will have particles exiting different ports rather than the same one.

### 5.1.3 HOM of non-classical and classical light

The effect of two photon interference is most pronounced for non-classical, quantum light sources. A visibility of the "HOM dip", which can be defined as

$$V_{HOM} = 1 - \frac{P_{coin}}{P_{det1} P_{det2}}, \quad (5.7)$$

where,  $P_{coin}$  is the total coincidence probability corresponding to the joint photon detection on both detectors, whilst  $P_{det1}$  and  $P_{det2}$  are the total probabilities of SPADs register the photon detection (180). We can relate we values on intensity correlation function, which are obtained through the measurements, by normalizing the function on the count values corresponding to the delay times  $\tau \gg 0$ . This delay,  $\tau$ , should be long enough so that the correlation function comes to a plateau, indicating absence of any correlations. This way we obtain a function of normalized coincidence counts, which value at  $\tau = 0$  is effectively equal to  $1 - V_{HOM}$ .

The visibility of HOM dip  $V_{HOM} = 100\%$ , was shown for a variety of single photon sources. However, the theoretical prediction of the HOM dip visibility for laser light has been shown to be  $V_{HOM} = 50\%$  (181), verified by experiments exploring two photon interference for the classical light sources (182; 183). However, in order to observe the ‘‘HOM dip’’, the lasers entering port  $a$  and  $b$  of the BS have to be phase

unrelated. This requirement stems from the nature of the “HOM dip” dynamics, which are dictated by the mutual phase coherence between paths  $a$  and  $b$ ; therefore, if the coherence is too high, the “dip” becomes incredibly broad and the dynamics are too slow to be observed, as shown in Ref. (182; 184). This simplest solution is to use two independent lasers (185; 186; 183), and alternative is to split the laser into two paths and introduce dephasing into one or both of the paths (184; 182). It was shown for the case of single laser, that the dynamics of HOM slope is too long to be visible with standard intensity correlation measurements however, by controlling the added phase noise for the beam at one of the entrance ports, the dip became resolvable through the experiment. In these experiments, the photons entering the beam splitter were sharing the same characteristics - laser frequency stabilization, spacial matching, and polarization filtering ensured that the degree of indistinguishability was as high as possible. However, due to the Poissonian statistics that the laser obeys, random correlations lead to an increase in coincidence counts at zero-time delay, resulting in decreased visibility of the HOM dip.

The use of the laser HOM interference shown to be a potential tool for applications in quantum communication systems and measurement device independent quantum key distribution (MDI-QKD) protocols (187; 188; 189). The two photon interference with classical light were also performed using two statistically dissimilar photon sources (190; 191).

## 5.2 Experimental results

In order to study polariton condensate photon indistinguishably, an optical setup depicted in Figure 5-1, was realized. Condensate emission was collected in transmission geometry, from the substrate side of the sample was sent into the HOM interferometer and was initially split into two paths: Path 1 couples directly into the single mode fiber leading to input 1 of the fiber 50:50 BS, whilst Path 2 passes through an optical delay before being coupled into input 2 of the fiber 50:50 BS. The fibre BS the has two outputs coupled into single mode fibres leading to SPADs. The SPADs are once again connected to the TCSPC electronics to detect joint photon

arrival. It is useful to note here, that by blocking one of the entrances to the fiber BS, we effectively obtain a scheme of HBT interferometry with polarization filtering.

To ensure photon indistinguishability was as high as possible, co-orientated polarisers (P) were installed before the fibre inputs on both paths to ensure that the light entering each port had the same polarisation. However, due to the non-polarisation maintaining structure of the single mode fibers, this was not enough to ensure that on the BS, the polarisation of light from both paths would be identical. Therefore, an additional set of polarisation optics (HWP and QWP) were installed after the prealigned polarizer in Path 1. The polarisation matching of both paths was measured by coupling light from the fibre BS into the Stokes polarimeter, previously shown in Figure 3-7, which revealed that the light polarisation was altering in the fibre. To correctly tune the polarisation, we first record the Stokes parameters from Path 2, from one of the outputs. Then, the HWP and QWP were iteratively adjusted on Path 1 to match the Stokes vector from Path 2, thus ensuring the polarisation of the light is identical at the BS from both paths. Due to the both outputs being common to both inputs, it is only necessary to perform this procedure for one of either output.

### 5.2.1 Laser HOM effect

Our previous investigation of polariton condensate polarization properties using the polarimeter and time integrated Stokes parameters measuring techniques (7) showed that in parameter space near condensation threshold and with nearly linearly polarized excitation condensate appears to be emitting unpolarized light  $DOP \approx 0$ . There are two explanations for this phenomena. On one hand, light can have a  $DOP \approx 1$  but due to rapid and spontaneous change of the polarization direction we cannot resolve the exact polarization due to integrating nature of the measurement averaging the true values. On the other hand, condensate can truly emit unpolarized light, with some parts of it emit photons differently, similarly to what we would have for a hot-body. To determine this effect and to study indistinguishability of condensate emitted photons in general, the scheme described in 5-1 was developed.

As discussed in Chapter 4, a starting point for an experiment involving a purely

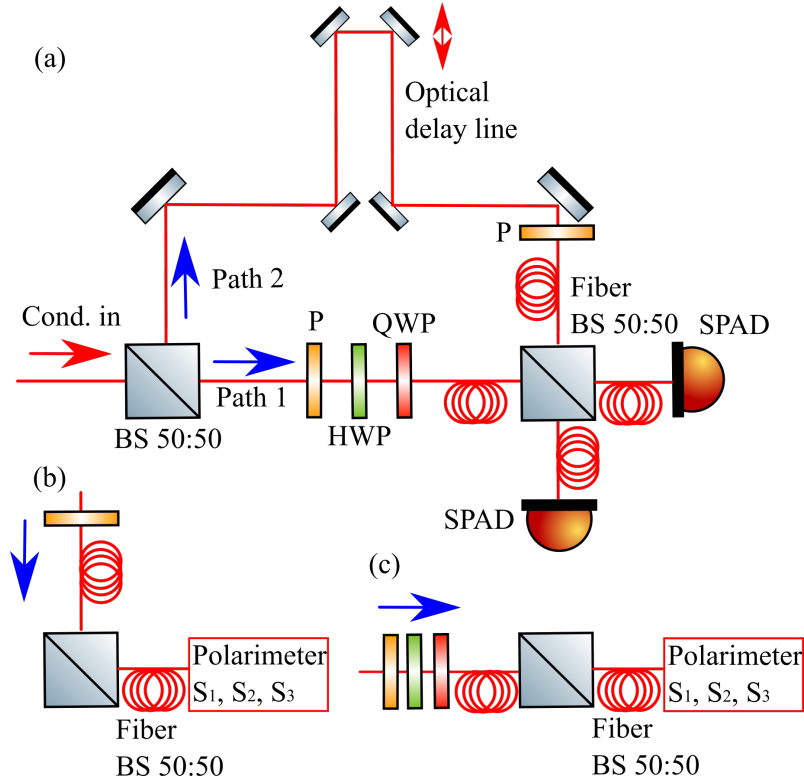


Figure 5-1: (a) Scheme for measuring HOM of optically confined polariton condensates. (b-c) Calibration of the setup through polarimeter to compensate for polarization drifting within the fibres leading to fiber BS.

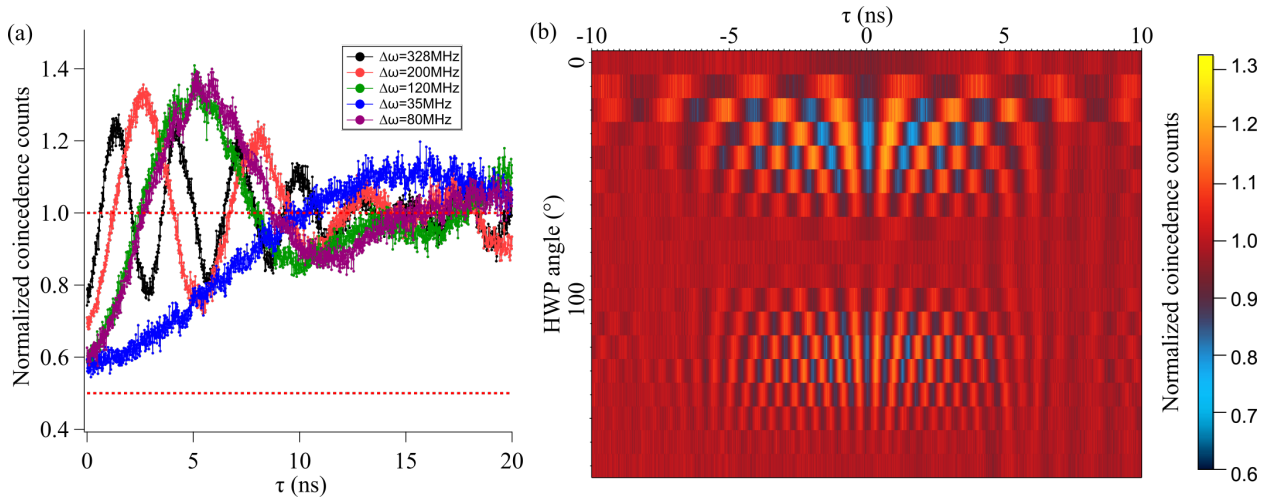


Figure 5-2: Hong-Ou-Mandel effect measured for two independent lasers. (a) Shows the normalized coincidences and dynamics of the HOM effect, for different laser detunings  $\Delta\omega$ , caused by thermal drift of the laser cavities. (b) The effect of the polarization degree of freedom on the "HOM dip" visibility. When polarization of two lasers become orthogonal to each other visibility become  $V_{HOM} \approx 0$ .

quantum effect, is to establish whether the experimental setup works as intended. For that matter, as a method of setup calibration a known from the literature result was obtained. The Hong-Ou-Mandel effect for two classical sources: two independent Ti:Sapphire CW lasers, coupled into the fiber BS, was measured and is shown in Figure 5-2(a). The observed result was photon anti-correlation, as was expected from reference (185). The result when lasers had the smallest frequency difference (blue, 35 MHz) shows a visibility of  $V_{HOM} \approx 40\%$ , and the longest time dynamics, as seen but the width of the dip. The visible oscillations in the correlation function in the Figure 5-2(a) correspond to the evolving energy shift between the lasers. For incoming photons with detuned frequencies, the effect on the HOM dip visibility and shape has already been observed and discussed in the literature. It manifests itself as a lower visibility at the  $\tau = 0$ , a narrower dip in time, and oscillations within the envelope of the HOM dip with the frequency equal to the photon frequency difference. The frequency drift in this experiment is unavoidable and happens due to the thermal expansion of one of the laser cavities.

The experimental observation of the HOM effect can be affected by variety of parameters and factors (180). As such, in order to have the polarisation parameter controlled, a pair of co-oriented polarizers were setup before each of the coupling inputs into the fiber BS. The data acquired from the HOM interferometer as a function of polarisation mis-match is shown in Figure 5-2(b). For this measurement an additional HWP was introduced, allowing for rotation of the linear polarisation of one of the lasers prior to coupling into the BS. Through the rotation of the HWP, we were effectively changing the distinguishability of the photons through polarisation state, which affected the visibility of the dip in zero-time delay. As the result, the HOM dip becomes barely visible when the light entering the BS inputs is orthogonally polarised, and had the highest visibility when the light entering the BS inputs is co-polarised. The oscillations that are present in the map shown in Figure 5-2(b) are once again, due to the evolving energy shift between the two laser sources.

## 5.2.2 Condensate HOM effect

In Chapter 4, it was discussed that the condensate photon statistics can differ greatly to the photon statistics of a laser, especially when polarization filtering takes place in the detection scheme. For this reason, to establish a base level experiment for the condensate, the initial measurement was prepared with strictly circularly polarized excitation, and with the pump power shortly above the condensation threshold at  $P = 1.1P_{th}$ . In this regime, the condensate emits mostly co-circularly polarized light as evidenced from our previous investigations (7) and from the literature (192; 125), and additionally it seems to follow Poissonian photon statistics. Taking this into consideration with other properties, such as, the seemingly single mode emission, and the extended first-order spatial and temporal coherence; it would appear the ground state condensate emits light which has similar properties to a laser. Now, as was mentioned above, we have used two phase independent lasers to calibrate the setup and achieve a reasonable HOM dip visibility. However, in similar fashion a single laser can be implemented, if the phase uncertainty between the two paths is achieved. For the condensate, the phase becomes uncertain outside this first-order coherence time  $\tau_c^{(1)} \approx 200ps$ , which is much shorter than for a single mode CW laser. For that reason, we use the delay-line in one of the paths (Path 2), in order to implement a time delay between the two paths at the fibre BS and access statistics outside of the phase coherence time. The dependence of the dip visibility as a function of the optical delay between Path 1 and Path 2 of the interferometer setup, is shown in Figure 5-3(a). It was observed, that the dip starts to emerge once the time delay is greater than the coherence time of the condensate.

In Fig 5-3(b), the profile of correlation function value at  $\tau = 0$  is presented, giving a maximum dip visibility of only  $V \approx 15\%$ . To understand the dependence of "HOM dip" versus the optical delay between the paths, a first order coherence measurement was performed using the a time-delay Michelson interferometer equipped with a retro reflector on the time-delayed arm, the result of which is shown in Figure 5-3(c). The first-order coherence function here is extracted by analyzing the fringe pattern visibility of condensate interfering with itself. The value at zero-time delay is lower than unity is due to the fact, that within the region of interest of the

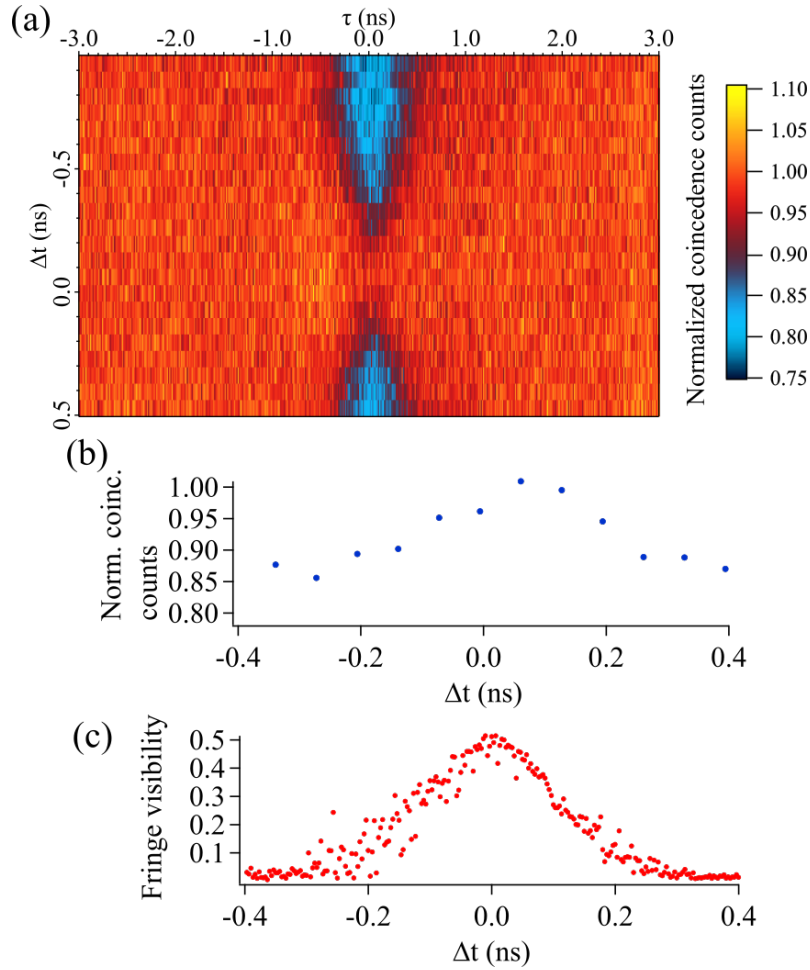


Figure 5-3: (a) Normalized correlation function map with the respect to optical delay  $\Delta t$  and electrical delay  $\tau$  for the condensate PL excited with circularly polarized pump at  $P = 1.1P_{th}$ . (b) Extracted normalized coincidence counts at  $\tau = 0$  versus optical time delay  $\Delta t$ . (c) Corresponding visibility of first order coherence fringes of the condensate interfering with itself with the respect to  $\Delta t$ .

interference pattern, the fringe visibility is different at the central area and outer area of the observed pattern. Due to the outer parts of the pattern contribute with lower visibility of the fringes, the coherence function value gets artificially lowered. However, it does not play a significant role for this investigation. We note here, that HOM dip for the condensate is not visible at the zero-time delay between two paths, where the phase coherence is maximum. From the analogy for the laser light we would expect to observe relatively broad HOM dip at this point, which becomes narrower as we move out of the temporal coherence region through the process of scanning of the delay line.

An example of a HOM dip, measured with the delay line in path 2 positioned

way out of the condensate coherence time ( $P = 1.1P_{th}$ , circularly polarized excitation), is shown in Figure 5-4(a) (red markers). The black markers display the HBT measurement for the same parameter space, and was done by blocking one of the entrance ports to the fiber BS. Since all discussed properties of the condensate are very similar to that of the single mode laser, the low visibility of the HOM dip is unique for the condensate. If we consider the random spatial-mode fluctuation of polariton condensates, whilst it would contribute randomly to the photon statistics in  $g^{(2)}(\tau)$  HBT measurements, without delivering any particular features into the intensity correlation function; for the measurement of the HOM effect, it can be seen as imperfect spatial mode matching condition, and contribute to the elevated coincidences at zero-time delay, and therefore, lowering the effective dip visibility.

Figs. 5-4(b-d) represent how the dip dynamics differ with the respect to the diameter of the condensate trapping potential. Here, the condensate is still in the ground state for all the different trap sizes, however, it is known that as the trap size increases, polaritons tend to condense into the excited states, which brings more complex dynamics for the consideration (193). This effect provides an upper limit for the size of the optical confinement, in order to remain within the same regime of condensate in the ground state. The visible difference of temporal slope, along the  $\tau$  axis here can be attributed to the change of mutual linewidth of the light entering the fiber BS with the variation of the trapping potential size, as was shown for first-order coherence for optically trapped condensates (121).

However, and interesting evolution of this effect was observed, for the same conditions as in Figure 5-4(a), but when the condensate being excited with linearly polarised light. Again, selecting a part of the sample where strain induced birefringence causes emission predominantly in the direction of effective in-plane magnetic field  $\Omega_{\parallel}$ , similarly to top panel of Figure 4-5, the photon statistics get significantly more affected by the presence of HOM effect. In Figs. 5-5 we show the photon statistics measured in the HBT configuration of the setup (one path blocked) with black line, whilst red line indicates correlations measured for the HOM interferometer configuration. The value of the correlation function at  $\tau = 0$  gets significantly lowered in the HOM configuration. This effect is visibly more enhanced, affecting the photon

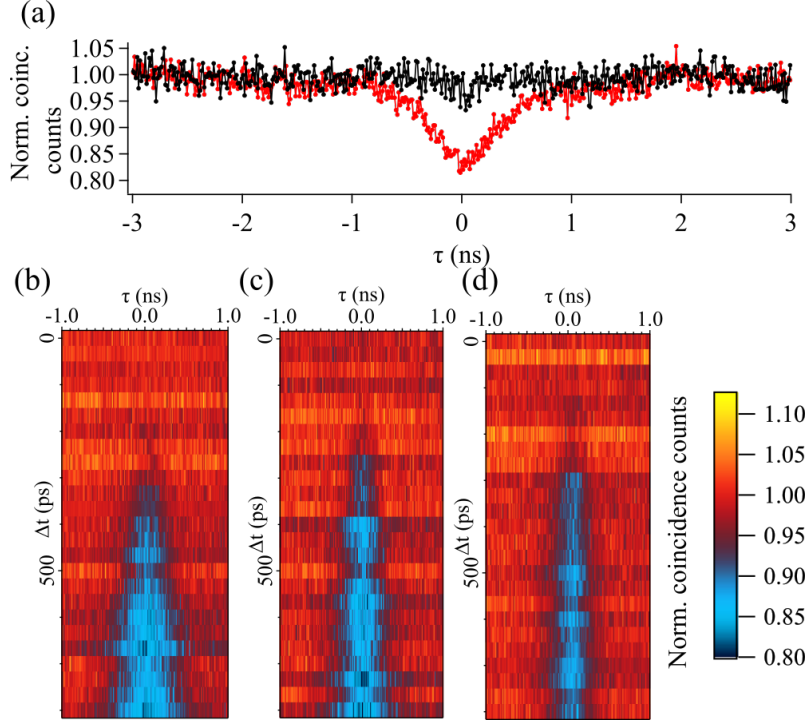


Figure 5-4: "HOM dip" for circularly excited polariton condensate at  $P = 1.1P_{th}$ . (a) Example HOM dip (red), outside of the condensate coherence time and condensate HBT (black). (b-d) "HOM dip" with the respect to optical delay  $\Delta t$  and electrical delay  $\tau$  for traps of different sizes,  $14\mu\text{m}$ ,  $10\mu\text{m}$  and  $9\mu\text{m}$  respectively.

statistics of super-bunched light comparably stronger, then what we see for the light with Poissonian photon statistics, when we pump the sample with circular light.

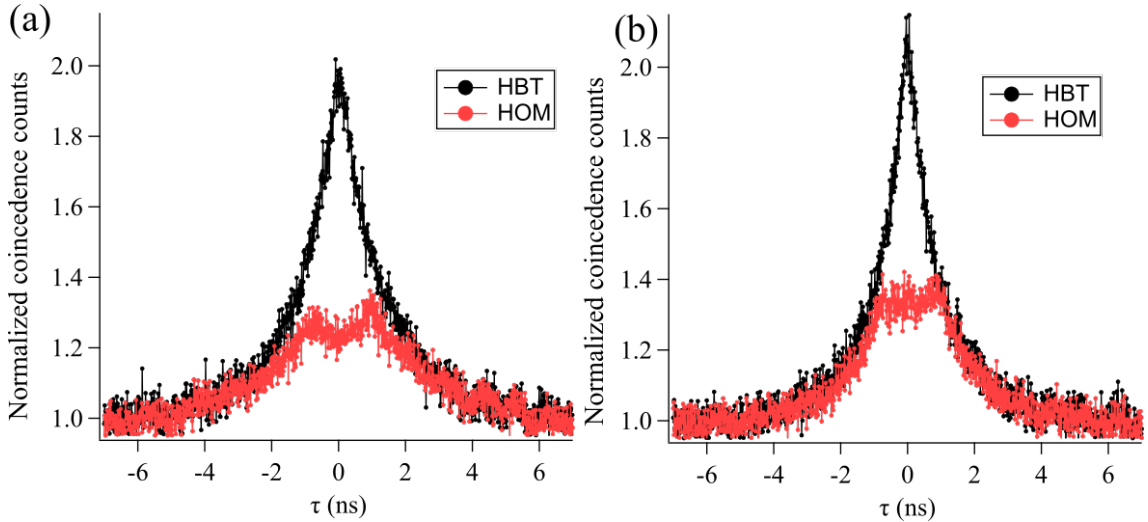


Figure 5-5: Correlation functions measured in the HBT (black) and HOM (red) interferometer configurations. Difference between correlation function values at  $\tau = 0$  are  $\delta = 0.76$  and  $\delta = 0.74$  with excitation polarization ellipticity  $\epsilon \approx 0.01$  (left) and  $\epsilon \approx 0$  (right) respectively.

Let us now consider the case, when the cavity is pumped with elliptically polarized light, and the emergent out-of plane magnetic field  $\Omega_{\perp}$  is enough to send the condensate pseudospin into precession. For this case, we have observed the periodic revival of the HOM effect, when delay line is scanned. Due to the inherent oscillating photon statistics present within the condensate as the spin processes, the process of scanning the delay on one of the paths effectively bring the oscillations in and out of phase on the fiber BS. A similar effect was observed through the macroscopic modulation of the CW signal with square pulses, when the HOM effect for a laser light source was studied (194). Figure 5-6 shows example maps with the HOM revival. As expected the frequency of the revivals were affected by the frequency of the pseudospin precessions, which increases in frequency from figure (a), to (c). In the same way as before, the precession frequency is set through the variation of the pump polarization ellipticity.

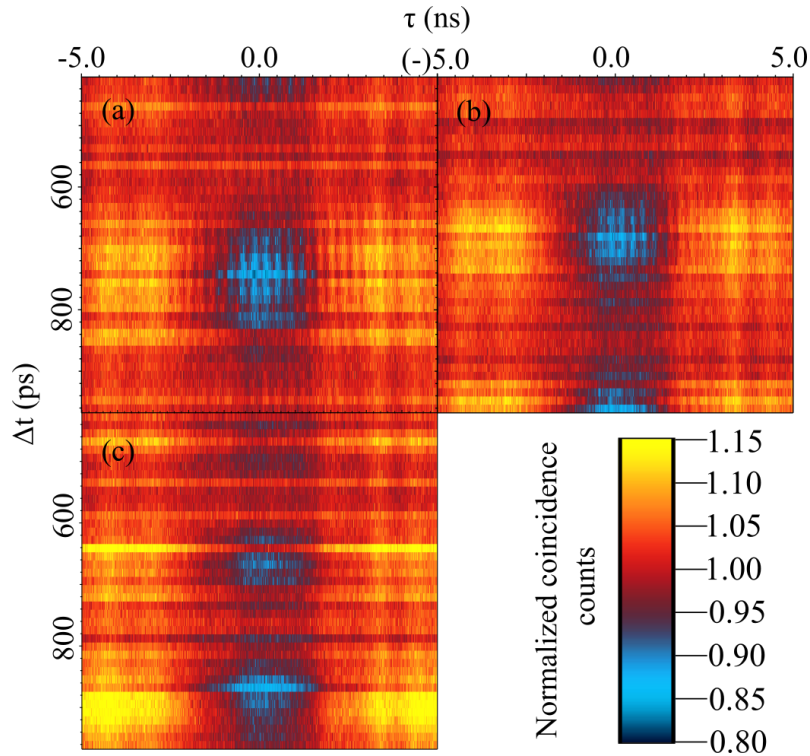


Figure 5-6: The revival of HOM dip visibility. The intensity oscillations in two paths of the HOM interferometer induced by the pseudospin precession come in phase and out of phase with the scanning of the optical delay  $\Delta t$ . This causes the periodic change of HOM visibility  $V_{HOM}$  through-out the scanning process. (a-c) Maps corresponding to the cases when precession period is  $\approx 354$ ,  $305$  and  $200ps$ , induced by different excitation polarization ellipticities, respectively.

Figure 5-7 shows how one of the maps HOM dip revival period corresponds to the fast oscillations of the condensate pseudospin. In Figure 5-7(c) the extracted period of precessions yields  $T = 300ps$ , and this value directly corresponds to the half period of dip revival that can be extracted from the map, and seen in Figure 5-7(b). Moreover, due to the high precision of the delay line, through the revival of the HOM dip, it becomes possible to observe the high frequency precession intensity fluctuations which can no longer be extracted with the HBT setup due to limited time resolution. This is demonstrated from the data recorded in Figure 5-6(c). While for the other maps in this figure, HBT measurements still provide us with the extractable oscillation data, the same measurements done in the regime of panel (c) are limited by the TCSPC time resolution, thus the oscillations are not detectable above the noise level. However, from the maps we can still indirectly tell that the precession period is  $T \approx 200ps$ .

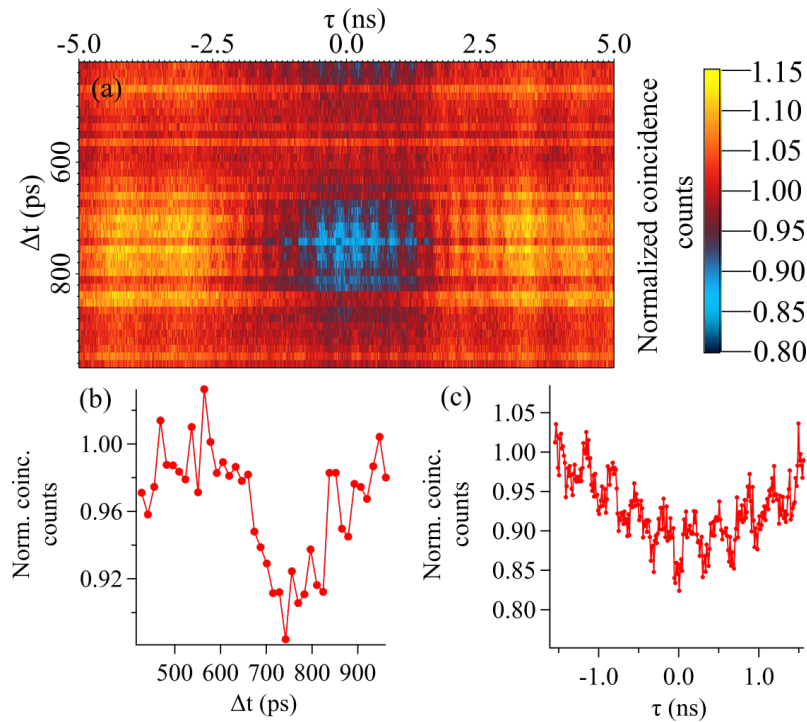


Figure 5-7: HOM dip revival period corresponds to the pseudospin precession frequency. (a) HOM revival map, with the (b) extracted along  $\tau = 0$  revival half-period of  $\approx 150ps$ . It corresponds to the pseudospin full cycle period of  $300ps$ , revealed through HBT measurements at the same regime, although, it is also visible in HOM scheme as a ripple in the revival map, with (c) showing example zoomed slice of the map.

### 5.2.3 Conclusion

The HOM effect observed for the classical light source - a single mode laser, yielding the intensity correlation function dip visibility approaching  $V_{HOM} \approx 50\%$ , is in a stark difference to the results obtained for the optically trapped polariton condensate, prepared in the most close to a laser regime, giving visibility of  $V_{HOM} \approx 15\%$ . With flexible tuning of the condensate excitation parameters, a superthermal photon statistics of polariton condensate PL can be reached. For this regime a significantly enhanced, when compared to the case of coherent photon statistics, HOM effect is observed, drastically decreasing the intensity correlation function magnitude. Putting the condensate into spinor precession regime reveal periodic revivals of the HOM effect, allowing to observe the spinor precession on the frequencies for which TCSPC time resolution is not enough. The theoretical framework as well as publications regarding these new observations of HOM effect in trapped polariton condensates is under preparation at the moment.

# Chapter 6

## Concluding Remarks And Future Perspectives

For the investigation into polyynes chains, we have shown that the sharp peaks emerging at low temperatures in the PL spectra of gold-stabilized carbon chains are indicative of the exciton and trion transitions, based on the edge electronic states in the chains. The triplet fine structure, that is very well seen at cryogenic temperature, is essentially independent of the length of the chain, whilst the absolute energies of the transitions increase for shorter chains. This observation demonstrates a potential within of synthesized polyynes chains for optoelectronic applications, especially in nanolasing and single photon emitters. Single molecule single photon sources are of high interest (68) however, the initial data for the intensity correlation function did not provide the characteristic photon anti-bunching. Further improvement of sample deposition could potentially allow for extraction of oriented chains of specific length, or tweezing out a singular chain could prove to be a step towards realizing a quantum emitter.

In the work for optically trapped polariton condensates we have realized multi-dimensional photon correlation tomography of spinor polariton condensate across its full polarization basis. The findings demonstrate extremely long spinor dephasing time of  $\tau_c = 9.2$  ns and the unique nonlinear mean field dynamics of the condensate pseudospin on the photon statistics with tunable crossover from super-thermal photon distribution to a coherent state. Such long dephasing time,  $10^3$  more than

the polariton lifetime, allows the observed photon statistics to become influenced by the nonlinear dynamical timescales of the coherent (mean-field) condensate. We identify stochastic linear polarization switching due to the inherent cavity birefringence resulting in polarisation sensitive photon bunching, and self-induced Larmor precessions in the GHz frequency range visible as oscillations in the linear polarised photon  $g_{i,j}^{(2)}(\tau)$  persistent for more than 10 ns. Our findings allow for the evaluation of the noise characteristics of spin-polarised polariton lasers, as well as, pave the way towards exploiting nonlinear mean-field dynamics of strongly non-equilibrium bosonic systems to fine control their photon statistics.

Trapped polariton condensates, in this sense, are a promising platform to study the quantum effects of light sources with non-trivial and controllable photon statistics. The experiments on the visibility of the Hong-Ou-Mandel effect revealed yet new differences between the a polariton condensate, or polariton laser, and traditional laser light. Low visibility of the HOM dip raises the question of the condensate spatial stability, whilst the increased effectiveness for the super-bunched light point towards a high dependence on the photon temporal correlation. The revivals of the HOM effect show an exciting way to further increase the frequency range of intensity oscillation research. The theoretical modeling of the shown results, would reveal the underlining physics for the photon statistical properties of the trapped condensates.

Many of the research results in this thesis can be explored further. Studying these effects for polaritons in the trapped excited states (195), assessing a system of multiple trapped polariton condensates could reveal exciting new properties to study (196). The realization of the feedback, into spontaneously emergent polarization modes can be interesting to research system chaotical behavior (26).

# Bibliography

- [1] S. Baryshev, A. Zasedatelev, H. Sigurdsson, I. Gnusov, J. D. Töpfer, A. Askitopoulos, and P. G. Lagoudakis, “Engineering photon statistics in a spinor polariton condensate,” *Phys. Rev. Lett.*, vol. 128, p. 087402, Feb 2022.
- [2] I. Gnusov, H. Sigurdsson, J. Töpfer, S. Baryshev, S. Alyatkin, and P. Lagoudakis, “All-optical linear-polarization engineering in single and coupled exciton-polariton condensates,” *Phys. Rev. Applied*, vol. 16, p. 034014, Sep 2021.
- [3] S. Kutrovszkaya, S. Demirchyan, A. Osipov, S. Baryshev, A. Zasedatelev, P. Lagoudakis, and A. Kavokin, “Exciton energy spectra in polyyne chains,” *Phys. Rev. Research*, vol. 3, p. 013071, Jan 2021.
- [4] S. Kutrovszkaya, A. Osipov, S. Baryshev, A. Zasedatelev, V. Samyshkin, S. Demirchyan, O. Pulci, D. Grassano, L. Gontrani, R. R. Hartmann, M. E. Portnoi, A. Kucherik, P. G. Lagoudakis, and A. Kavokin, “Excitonic fine structure in emission of linear carbon chains,” *Nano Letters*, vol. 20, no. 9, pp. 6502–6509, 2020. PMID: 32787174.
- [5] S. Kutrovszkaya, S. Demirchyan, A. Osipov, S. Baryshev, A. Zasedatelev, P. Lagoudakis, and A. Kavokin, “Exciton radiative lifetime in a monoatomic carbon chain,” *New Journal of Physics*, vol. 23, p. 033007, mar 2021.
- [6] I. Gnusov, H. Sigurdsson, S. Baryshev, A. Askitopoulos, and P. G. Lagoudakis, “Pseudo-spin destabilization in optically confined exciton-polariton condensates,” in *Frontiers in Optics / Laser Science*, p. FTu2D.4, Optica Publishing Group, 2020.
- [7] I. Gnusov, H. Sigurdsson, S. Baryshev, T. Ermatov, A. Askitopoulos, and P. G. Lagoudakis, “Optical orientation, polarization pinning, and depolarization dynamics in optically confined polariton condensates,” *Phys. Rev. B*, vol. 102, p. 125419, Sep 2020.
- [8] Y. Segawa, H. Ito, and K. Itami, “Structurally uniform and atomically precise carbon nanostructures,” *Nature Reviews Materials*, vol. 1, p. 15002, Jan 2016.
- [9] A. E. Goresy and G. Donnay, “A new allotropic form of carbon from the ries crater,” *Science*, vol. 161, no. 3839, pp. 363–364, 1968.
- [10] A. Whittaker, “Carbon: Occurrence of carbyne forms of carbon in natural graphite,” *Carbon*, vol. 17, no. 1, pp. 21–24, 1979.

- [11] X.-Y. Chuan, Z. Zheng, and J. Chen, “Flakes of natural carbyne in a diamond mine,” *Carbon*, vol. 41, no. 10, pp. 1877–1880, 2003.
- [12] L. LANDAU and E. LIFSHITZ, “Chapter i - the fundamental principles of statistical physics,” in *Statistical Physics (Third Edition)* (L. LANDAU and E. LIFSHITZ, eds.), pp. 1–33, Oxford: Butterworth-Heinemann, third edition ed., 1980.
- [13] T. GIBTNER, F. HAMPPEL, J.-P. GISELBRECHT, and A. HIRSCH, “End-cap stabilized oligoynes: Model compounds for the linear sp carbon allotrope carbyne,” *Chemistry – A European Journal*, vol. 8, no. 2, pp. 408–432, 2002.
- [14] R. KHANNA, M. IKRAM-UL-HAQ, A. RAWAL, R. RAJARAO, V. SAHAJWALLA, R. CAYUMIL, and P. S. MUKHERJEE, “Formation of carbyne-like materials during low temperature pyrolysis of lignocellulosic biomass: A natural resource of linear sp carbons,” *Scientific Reports*, vol. 7, p. 16832, Dec 2017.
- [15] M. LIU, V. I. ARTYUKHOV, H. LEE, F. XU, and B. I. YAKOBSON, “Carbyne from first principles: Chain of c atoms, a nanorod or a nanorope,” *ACS Nano*, vol. 7, pp. 10075–10082, Nov 2013.
- [16] A. H. SAFAVI-NAEINI, J. CHAN, J. T. HILL, S. GRÖBLACHER, H. MIAO, Y. CHEN, M. ASPELMEYER, and O. PAINTER, “Laser noise in cavity-optomechanical cooling and thermometry,” *New Journal of Physics*, vol. 15, p. 035007, mar 2013.
- [17] C. M. CAVES, “Quantum-mechanical noise in an interferometer,” *Phys. Rev. D*, vol. 23, pp. 1693–1708, Apr 1981.
- [18] K. BANASZEK, L. KUNZ, M. JACHURA, and M. JARZYNA, “Quantum limits in optical communications,” *J. Lightwave Technol.*, vol. 38, pp. 2741–2754, May 2020.
- [19] J. WIERSIG, C. GIES, F. JAHNKE, M. AßMANN, T. BERSTERMANN, M. BAYER, C. KISTNER, S. REITZENSTEIN, C. SCHNEIDER, S. HÖFFLING, A. FORCHEL, C. KRUSE, J. KALDEN, and D. HOMMEL, “Direct observation of correlations between individual photon emission events of a microcavity laser,” *Nature*, vol. 460, pp. 245–249, Jul 2009.
- [20] M. AßMANN, J.-S. TEMPEL, F. VEIT, M. BAYER, A. RAHIMI-IMAN, A. LÖFFLER, S. HÖFFLING, S. REITZENSTEIN, L. WORSCHER, and A. FORCHEL, “From polariton condensates to highly photonic quantum degenerate states of bosonic matter,” *Proceedings of the National Academy of Sciences*, vol. 108, no. 5, pp. 1804–1809, 2011.
- [21] A. PERRIN, R. BÜCKER, S. MANZ, T. BETZ, C. KOLLER, T. PLISSON, T. SCHUMM, and J. SCHMIEDMAYER, “Hanbury Brown and Twiss correlations across the Bose-Einstein condensation threshold,” *Nature Physics*, vol. 8, pp. 195–198, Mar 2012.
- [22] B. T. WALKER, J. D. RODRIGUES, H. S. DHAR, R. F. OULTON, F. MINTERT, and R. A. NYMAN, “Non-stationary statistics and formation jitter in transient photon condensation,” *Nature Communications*, vol. 11, p. 1390, Mar 2020.

- [23] M. B. Willemsen, M. P. van Exter, and J. P. Woerdman, “Anatomy of a polarization switch of a vertical-cavity semiconductor laser,” *Phys. Rev. Lett.*, vol. 84, pp. 4337–4340, May 2000.
- [24] H. A. M. Leymann, C. Hopfmann, F. Albert, A. Foerster, M. Khanbekyan, C. Schneider, S. Höfling, A. Forchel, M. Kamp, J. Wiersig, and S. Reitzenstein, “Intensity fluctuations in bimodal micropillar lasers enhanced by quantum-dot gain competition,” *Phys. Rev. A*, vol. 87, p. 053819, May 2013.
- [25] C. Redlich, B. Lingnau, S. Holzinger, E. Schlottmann, S. Kreinberg, C. Schneider, M. Kamp, S. Höfling, J. Wolters, S. Reitzenstein, and K. Lüdge, “Mode-switching induced super-thermal bunching in quantum-dot microlasers,” *New Journal of Physics*, vol. 18, p. 063011, jun 2016.
- [26] F. Albert, C. Hopfmann, S. Reitzenstein, C. Schneider, S. Höfling, M. Kamp, W. Kinzel, A. Forchel, and I. Kanter, “Observing chaos for quantum-dot microlasers with external feedback,” *Nature communications*, vol. 2, p. 366, 06 2011.
- [27] P. Ryczkowski, M. Barbier, A. T. Friberg, J. M. Dudley, and G. Genty, “Ghost imaging in the time domain,” *Nature Photonics*, vol. 10, pp. 167–170, Mar 2016.
- [28] A. Jechow, M. Seefeldt, H. Kurzke, A. Heuer, and R. Menzel, “Enhanced two-photon excited fluorescence from imaging agents using true thermal light,” *Nature Photonics*, vol. 7, pp. 973–976, Dec 2013.
- [29] M. Lindemann, G. Xu, T. Pusch, R. Michalzik, M. Hofmann, I. Žutić, and N. Gerhardt, “Ultrafast spin-lasers,” *Nature*, vol. 568, pp. 1–4, 04 2019.
- [30] C. Weisbuch, M. Nishioka, A. Ishikawa, and Y. Arakawa, “Observation of the coupled exciton-photon mode splitting in a semiconductor quantum microcavity,” *Phys. Rev. Lett.*, vol. 69, pp. 3314–3317, Dec 1992.
- [31] J. Kasprzak, M. Richard, S. Kundermann, A. Baas, P. Jeambrun, J. Keeling, F. M. Marchetti, M. Szymańska, R. André, J. Staehli, V. Savona, P. Littlewood, B. Deveaud, and D. Le Si, “Bose–Einstein condensation of exciton polaritons,” *Nature*, vol. 443, pp. 409–14, 10 2006.
- [32] N. C. Gerhardt and M. R. Hofmann, “Spin-controlled vertical-cavity surface-emitting lasers,” *Advances in Optical Technologies*, vol. 2012, p. 268949, Mar 2012.
- [33] D. Read, T. C. H. Liew, Y. G. Rubo, and A. V. Kavokin, “Stochastic polarization formation in exciton-polariton Bose-Einstein condensates,” *Phys. Rev. B*, vol. 80, p. 195309, Nov 2009.
- [34] T. Liew, I. Shelykh, and G. Malpuech, “Polaritonic devices,” *Physica E: Low-dimensional Systems and Nanostructures*, vol. 43, no. 9, pp. 1543 – 1568, 2011.

- [35] A. Delteil, T. Fink, A. Schade, S. Höfling, C. Schneider, and A. İmamoğlu, “Towards polariton blockade of confined exciton–polaritons,” *Nature Materials*, vol. 18, pp. 219–222, March 2019.
- [36] G. Muñoz-Matutano, A. Wood, M. Johnsson, X. Vidal, B. Baragiola, A. Reinhard, A. Lemaître, J. Bloch, A. Amo, G. Nogues, B. Besga, M. Richard, and T. Volz, “Emergence of quantum correlations from interacting fibre-cavity polaritons,” *Nature Materials*, vol. 18, p. 213, 03 2019.
- [37] A. Amo, D. Sanvitto, F. P. Laussy, D. Ballarini, E. d. Valle, M. D. Martin, A. Lemaître, J. Bloch, D. N. Krizhanovskii, M. S. Skolnick, C. Tejedor, and L. Viña, “Collective fluid dynamics of a polariton condensate in a semiconductor microcavity,” *Nature*, vol. 457, pp. 291–295, Jan 2009.
- [38] A. Amo, J. Lefrère, S. Pigeon, C. Adrados, C. Ciuti, I. Carusotto, R. Houdré, E. Giacobino, and A. Bramati, “Superfluidity of polaritons in semiconductor microcavities,” *Nature Physics*, vol. 5, pp. 805–810, November 2009.
- [39] S. Kim, B. Zhang, Z. Wang, J. Fischer, S. Brodbeck, M. Kamp, C. Schneider, S. Höfling, and H. Deng, “Coherent polariton laser,” *Phys. Rev. X*, vol. 6, p. 011026, Mar 2016.
- [40] J. D. Töpfer, I. Chatzopoulos, H. Sigurdsson, T. Cookson, Y. G. Rubo, and P. G. Lagoudakis, “Engineering spatial coherence in lattices of polariton condensates,” *Optica*, vol. 8, pp. 106–113, Jan 2021.
- [41] P. G. Savvidis, J. J. Baumberg, R. M. Stevenson, M. S. Skolnick, D. M. Whittaker, and J. S. Roberts, “Angle-resonant stimulated polariton amplifier,” *Phys. Rev. Lett.*, vol. 84, pp. 1547–1550, Feb 2000.
- [42] M. Saba, C. Ciuti, J. Bloch, V. Thierry-Mieg, R. André, D. Le Si, S. Kundermann, A. Mura, G. Bongiovanni, J. Staehli, and B. Deveaud, “High-temperature ultrafast polariton parametric amplification in semiconductor microcavities,” *Nature*, vol. 414, pp. 731–5, 01 2002.
- [43] D. Ballarini, M. De Giorgi, E. Cancellieri, R. Houdré, E. Giacobino, R. Cingolani, G. Gigli, and D. Sanvitto, “All-optical polariton transistor,” *Nature communications*, vol. 4, p. 1778, 04 2013.
- [44] C. Antón, T. C. H. Liew, G. Tosi, M. D. Martín, T. Gao, Z. Hatzopoulos, P. S. Eldridge, P. G. Savvidis, and L. Viña, “Dynamics of a polariton condensate transistor switch,” *Applied Physics Letters*, vol. 101, no. 26, p. 261116, 2012.
- [45] A. Zasedatelev, A. Baranikov, D. Urbonas, F. Scafirimuto, U. Scherf, T. Stöferle, R. Mahrt, and P. Lagoudakis, “A room-temperature organic polariton transistor,” *Nature Photonics*, vol. 13, pp. 1–6, 06 2019.
- [46] H. S. Nguyen, D. Vishnevsky, C. Sturm, D. Tanese, D. Solnyshkov, E. Galopin, A. Lemaître, I. Sagnes, A. Amo, G. Malpuech, and J. Bloch, “Realization of a double-barrier resonant tunneling diode for cavity polaritons,” *Phys. Rev. Lett.*, vol. 110, p. 236601, Jun 2013.

- [47] M. Klaas, J. Beierlein, E. Rozas, S. Klembt, H. Suchomel, T. Harder, K. Winkler, M. Emmerling, H. Flayac, M. Martin, L. Vina, S. Höfling, and C. Schneider, “Counter-directional polariton coupler,” *Applied Physics Letters*, vol. 114, p. 061102, 02 2019.
- [48] F. Marsault, H. S. Nguyen, D. Tanese, A. Lemaître, E. Galopin, I. Sagnes, A. Amo, and J. Bloch, “Realization of an all optical exciton-polariton router,” *Applied Physics Letters*, vol. 107, no. 20, p. 201115, 2015.
- [49] T. Gao, C. Antón, T. C. H. Liew, M. D. Martín, Z. Hatzopoulos, L. Viña, P. S. Eldridge, and P. G. Savvidis, “Spin selective filtering of polariton condensate flow,” *Applied Physics Letters*, vol. 107, no. 1, p. 011106, 2015.
- [50] C. Sturm, D. Tanese, H. S. Nguyen, H. Flayac, E. Galopin, A. Lemaître, I. Sagnes, D. Solnyshkov, A. Amo, G. Malpuech, and J. Bloch, “All-optical phase modulation in a cavity-polariton Mach-Zehnder interferometer,” *Nature communications*, vol. 5, p. 3278, 02 2014.
- [51] S. Klembt, T. H. Harder, O. A. Egorov, K. Winkler, R. Ge, M. A. Bandres, M. Emmerling, L. Worschech, T. C. H. Liew, M. Segev, C. Schneider, and S. Höfling, “Exciton-polariton topological insulator,” *Nature*, vol. 562, pp. 552–556, Oct 2018.
- [52] A. Amo, T. Liew, C. Adrados, R. Houdré, E. Giacobino, and A. Kavokin, “Exciton-polariton spin switches,” *Nature Photonics*, vol. 4, pp. 361–366, 04 2010.
- [53] T. Gao, P. S. Eldridge, T. C. H. Liew, S. I. Tsintzos, G. Stavrinidis, G. Deligeorgis, Z. Hatzopoulos, and P. G. Savvidis, “Polariton condensate transistor switch,” *Phys. Rev. B*, vol. 85, p. 235102, Jun 2012.
- [54] C. Antón, T. C. H. Liew, D. Sarkar, M. D. Martín, Z. Hatzopoulos, P. S. Eldridge, P. G. Savvidis, and L. Viña, “Operation speed of polariton condensate switches gated by excitons,” *Phys. Rev. B*, vol. 89, p. 235312, Jun 2014.
- [55] R. Cerna, Y. Léger, T. K. Paraíso, M. Wouters, F. Morier-Genoud, M. T. Portella-Oberli, and B. Deveaud, “Ultrafast tristable spin memory of a coherent polariton gas,” *Nature Communications*, vol. 4, p. 2008, Jun 2013.
- [56] R. Spano, J. Cuadra, C. Lingg, D. Sanvitto, M. D. Martin, P. R. Eastham, M. van der Poel, J. M. Hvam, and L. V. na, “Build up of off-diagonal long-range order in microcavity exciton-polaritons across the parametric threshold,” *Opt. Express*, vol. 21, pp. 10792–10800, May 2013.
- [57] G. Nardin, K. G. Lagoudakis, M. Wouters, M. Richard, A. Baas, R. André, L. S. Dang, B. Pietka, and B. Deveaud-Plédran, “Dynamics of long-range ordering in an exciton-polariton condensate,” *Phys. Rev. Lett.*, vol. 103, p. 256402, Dec 2009.

- [58] H. Ohadi, E. Kammann, T. C. H. Liew, K. G. Lagoudakis, A. V. Kavokin, and P. G. Lagoudakis, “Spontaneous symmetry breaking in a polariton and photon laser,” *Phys. Rev. Lett.*, vol. 109, p. 016404, Jul 2012.
- [59] T. Horikiri, P. Schwendimann, A. Quattropani, S. Höfling, A. Forchel, and Y. Yamamoto, “Higher order coherence of exciton-polariton condensates,” *Phys. Rev. B*, vol. 81, p. 033307, Jan 2010.
- [60] M. Klaas, H. Flayac, M. Amthor, I. G. Savenko, S. Brodbeck, T. Ala-Nissila, S. Klemmt, C. Schneider, and S. Höfling, “Evolution of temporal coherence in confined exciton-polariton condensates,” *Phys. Rev. Lett.*, vol. 120, p. 017401, Jan 2018.
- [61] H. Ohadi, A. Dreismann, Y. G. Rubo, F. Pinsker, Y. del Valle-Inclan Redondo, S. I. Tsintzos, Z. Hatzopoulos, P. G. Savvidis, and J. J. Baumberg, “Spontaneous spin bifurcations and ferromagnetic phase transitions in a spinor exciton-polariton condensate,” *Phys. Rev. X*, vol. 5, p. 031002, Jul 2015.
- [62] V. G. Sala, F. Marsault, M. Wouters, E. Galopin, I. Sagnes, A. Lemaître, J. Bloch, and A. Amo, “Stochastic precession of the polarization in a polariton laser,” *Phys. Rev. B*, vol. 93, p. 115313, Mar 2016.
- [63] R. Kaltenbaek, B. Blauensteiner, M. Żukowski, M. Aspelmeyer, and A. Zeilinger, “Experimental interference of independent photons,” *Phys. Rev. Lett.*, vol. 96, p. 240502, Jun 2006.
- [64] P. J. Mosley, J. S. Lundeen, B. J. Smith, P. Wasylczyk, A. B. U’Ren, C. Silberhorn, and I. A. Walmsley, “Heralded generation of ultrafast single photons in pure quantum states,” *Phys. Rev. Lett.*, vol. 100, p. 133601, Apr 2008.
- [65] K. Sanaka, A. Pawlis, T. D. Ladd, K. Lischka, and Y. Yamamoto, “Indistinguishable photons from independent semiconductor nanostructures,” *Phys. Rev. Lett.*, vol. 103, p. 053601, Jul 2009.
- [66] H. Bernien, L. Childress, L. Robledo, M. Markham, D. Twitchen, and R. Hanson, “Two-photon quantum interference from separate nitrogen vacancy centers in diamond,” *Phys. Rev. Lett.*, vol. 108, p. 043604, Jan 2012.
- [67] P. Maunz, D. L. Moehring, S. Olmschenk, K. C. Younge, D. N. Matsukevich, and C. Monroe, “Quantum interference of photon pairs from two remote trapped atomic ions,” *Nature Physics*, vol. 3, pp. 538–541, Aug 2007.
- [68] A. Kiraz, M. Ehrl, T. Hellerer, O. E. Müstecaplıoğlu, C. Bräuchle, and A. Zumbusch, “Indistinguishable photons from a single molecule,” *Phys. Rev. Lett.*, vol. 94, p. 223602, Jun 2005.
- [69] A. Lyons, G. C. Knee, E. Bolduc, T. Roger, J. Leach, E. M. Gauger, and D. Faccio, “Attosecond-resolution hong-ou-mandel interferometry,” *Science Advances*, vol. 4, no. 5, p. eaap9416, 2018.

- [70] Y. Chen, M. Fink, F. Steinlechner, J. P. Torres, and R. Ursin, “Hong-ou-mandel interferometry on a biphoton beat note,” *npj Quantum Information*, vol. 5, p. 43, May 2019.
- [71] W. P. Grice, “Arbitrarily complete bell-state measurement using only linear optical elements,” *Phys. Rev. A*, vol. 84, p. 042331, Oct 2011.
- [72] S. L. Braunstein and S. Pirandola, “Side-channel-free quantum key distribution,” *Phys. Rev. Lett.*, vol. 108, p. 130502, Mar 2012.
- [73] J.-Y. Guan, Z. Cao, Y. Liu, G.-L. Shen-Tu, J. S. Pelc, M. M. Fejer, C.-Z. Peng, X. Ma, Q. Zhang, and J.-W. Pan, “Experimental passive round-robin differential phase-shift quantum key distribution,” *Phys. Rev. Lett.*, vol. 114, p. 180502, May 2015.
- [74] T.-M. Zhao, H. Zhang, J. Yang, Z.-R. Sang, X. Jiang, X.-H. Bao, and J.-W. Pan, “Entangling different-color photons via time-resolved measurement and active feed forward,” *Phys. Rev. Lett.*, vol. 112, p. 103602, Mar 2014.
- [75] T. C. Ralph, A. G. White, W. J. Munro, and G. J. Milburn, “Simple scheme for efficient linear optics quantum gates,” *Phys. Rev. A*, vol. 65, p. 012314, Dec 2001.
- [76] X. Zou, K. Pahlke, and W. Mathis, “Teleportation implementation of nondeterministic quantum logic operations by using linear optical elements,” *Phys. Rev. A*, vol. 65, p. 064305, Jun 2002.
- [77] S. Scheel, J. Pachos, E. A. Hinds, and P. L. Knight, “Quantum gates and decoherence,” 2004.
- [78] H. Ollivier, S. E. Thomas, S. C. Wein, I. M. de Buy Wenniger, N. Coste, J. C. Loredó, N. Somaschi, A. Harouri, A. Lemaitre, I. Sagnes, L. Lanco, C. Simon, C. Anton, O. Krebs, and P. Senellart, “Hong-ou-mandel interference with imperfect single photon sources,” *Phys. Rev. Lett.*, vol. 126, p. 063602, Feb 2021.
- [79] H. W. Kroto, J. R. Heath, S. C. O’Brien, R. F. Curl, and R. E. Smalley, “C60: Buckminsterfullerene,” *Nature*, vol. 318, pp. 162–163, Nov 1985.
- [80] R. Haddon, L. Brus, and K. Raghavachari, “Electronic structure and bonding in icosahedral c60,” *Chemical Physics Letters*, vol. 125, no. 5, pp. 459–464, 1986.
- [81] S. Iijima and T. Ichihashi, “Single-shell carbon nanotubes of 1-nm diameter,” *Nature*, vol. 363, pp. 603–605, Jun 1993.
- [82] K. S. Novoselov, A. K. Geim, S. V. Morozov, D. Jiang, Y. Zhang, S. V. Dubonos, I. V. Grigorieva, and A. A. Firsov, “Electric field effect in atomically thin carbon films,” *Science*, vol. 306, no. 5696, pp. 666–669, 2004.

- [83] C. S. Casari, M. Tommasini, R. R. Tykwinski, and A. Milani, "Carbon-atom wires: 1-d systems with tunable properties," *Nanoscale*, vol. 8, pp. 4414–4435, 2016.
- [84] V. I. Artyukhov, M. Liu, and B. I. Yakobson, "Mechanically induced metal–insulator transition in carbyne," *Nano Letters*, vol. 14, no. 8, pp. 4224–4229, 2014. PMID: 24991984.
- [85] W. Meiling and F. Stary, *Nanosecond Pulse Techniques*. Gordon and Breach, 1968.
- [86] J. Yguerabide, "Nanosecond fluorescence spectroscopy of macromolecules," in *Enzyme Structure, Part C*, vol. 26 of *Methods in Enzymology*, pp. 498–578, Academic Press, 1972.
- [87] W. Becker, *The bh TCSPC handbook*. Becker - Hickl GmbH Nahmitzer Damm 30 12277, Berlin (2021), 2021.
- [88] B. Pan, J. Xiao, J. Li, P. Liu, C. Wang, and G. Yang, "Carbyne with finite length: The one-dimensional sp carbon," *Science Advances*, vol. 1, no. 9, p. e1500857, 2015.
- [89] A. Kucherik, S. Arakelian, T. Vartanyan, S. Kutrovskaya, A. Osipov, A. Povolotskaya, A. Povolotskii, and A. Man'shina, "Laser-induced synthesis of metal–carbon materials for implementing surface-enhanced raman scattering," *Optics and Spectroscopy*, vol. 121, pp. 263–270, Aug 2016.
- [90] A. O. Kucherik, S. M. Arakelian, S. V. Garnov, S. V. Kutrovskaya, D. S. Nogtev, A. V. Osipov, and K. S. Khor'kov, "Two-stage laser-induced synthesis of linear carbon chains," *Quantum Electronics*, vol. 46, pp. 627–633, jul 2016.
- [91] O. V. Yazyev and A. Pasquarello, "Effect of metal elements in catalytic growth of carbon nanotubes," *Phys. Rev. Lett.*, vol. 100, p. 156102, Apr 2008.
- [92] G. Frens, "Controlled nucleation for the regulation of the particle size in monodisperse gold suspensions," *Nature Physical Science*, vol. 241, pp. 20–22, Jan. 1973.
- [93] J. Turkevich, P. C. Stevenson, and J. Hillier, "A study of the nucleation and growth processes in the synthesis of colloidal gold," *Discuss. Faraday Soc.*, vol. 11, pp. 55–75, 1951.
- [94] L. Liu and A. Corma, "Metal catalysts for heterogeneous catalysis: From single atoms to nanoclusters and nanoparticles," *Chemical Reviews*, vol. 118, no. 10, pp. 4981–5079, 2018. PMID: 29658707.
- [95] K. J. Taylor, C. L. Pettiette-Hall, O. Cheshnovsky, and R. E. Smalley, "Ultraviolet photoelectron spectra of coinage metal clusters," *The Journal of Chemical Physics*, vol. 96, no. 4, pp. 3319–3329, 1992.

- [96] D. Buceta, Y. Piñeiro, C. Vázquez-Vázquez, J. Rivas, and M. A. López-Quintela, “Metallic clusters: Theoretical background, properties and synthesis in microemulsions,” *Catalysts*, vol. 4, no. 4, pp. 356–374, 2014.
- [97] L. F. Cótica, I. A. Santos, E. M. Giroto, E. V. Ferri, and A. A. Coelho, “Surface spin disorder effects in magnetite and poly(thiophene)-coated magnetite nanoparticles,” *Journal of Applied Physics*, vol. 108, no. 6, p. 064325, 2010.
- [98] S. Kutrovskaia, I. Chestnov, A. Osipov, V. Samyshkin, I. Sapegina, A. Kavokin, and A. Kucherik, “Electric field assisted alignment of monoatomic carbon chains,” *Scientific Reports*, vol. 10, p. 9709, Jun 2020.
- [99] F. Cataldo, “Synthesis of polyynes in a submerged electric arc in organic solvents,” *Carbon*, vol. 42, no. 1, pp. 129–142, 2004.
- [100] A. R. Amori, Z. Hou, and T. D. Krauss, “Excitons in single-walled carbon nanotubes and their dynamics,” *Annual Review of Physical Chemistry*, vol. 69, no. 1, pp. 81–99, 2018. PMID: 29401037.
- [101] E. Mostaani, B. Monserrat, N. D. Drummond, and C. J. Lambert, “Quasiparticle and excitonic gaps of one-dimensional carbon chains,” *Phys. Chem. Chem. Phys.*, vol. 18, pp. 14810–14821, 2016.
- [102] G. M. Alexey Kavokin, Jeremy J. Baumberg and F. P. Laussy, *Semiconductor Optics*. Oxford University Press Inc., New York 2007, 2007.
- [103] C. F. Klingshirn, *Semiconductor Optics*. Springer-Verlag Berlin Heidelberg 2012, 2012.
- [104] M. H. Anderson, J. R. Ensher, M. R. Matthews, C. E. Wieman, and E. A. Cornell, “Observation of bose-einstein condensation in a dilute atomic vapor,” *Science*, vol. 269, no. 5221, pp. 198–201, 1995.
- [105] K. B. Davis, M. O. Mewes, M. R. Andrews, N. J. van Druten, D. S. Durfee, D. M. Kurn, and W. Ketterle, “Bose-einstein condensation in a gas of sodium atoms,” *Phys. Rev. Lett.*, vol. 75, pp. 3969–3973, Nov 1995.
- [106] P. Kapitza, “Viscosity of liquid helium below the  $\lambda$  – point,” *Nature*, vol. 141, p. 74, Jan.1938.
- [107] J. F. Allen and A. D. Misener, “Flow of liquid helium ii,” *Nature*, vol. 141, p. 75, Jan. 1938.
- [108] O. Penrose and L. Onsager, “Bose-einstein condensation and liquid helium,” *Phys. Rev.*, vol. 104, pp. 576–584, Nov 1956.
- [109] C. N. Yang, “Concept of off-diagonal long-range order and the quantum phases of liquid he and of superconductors,” *Rev. Mod. Phys.*, vol. 34, pp. 694–704, Oct 1962.
- [110] Y. Sun, P. Wen, Y. Yoon, G. Liu, M. Steger, L. N. Pfeiffer, K. West, D. W. Snoke, and K. A. Nelson, “Bose-einstein condensation of long-lifetime polaritons in thermal equilibrium,” *Phys. Rev. Lett.*, vol. 118, p. 016602, Jan 2017.

- [111] L. V. Butov, “A polariton laser,” *Nature*, vol. 447, pp. 540–541, May 2007.
- [112] L. V. Butov and A. V. Kavokin, “The behaviour of exciton–polaritons,” *Nature Photonics*, vol. 6, pp. 2–2, Jan 2012.
- [113] B. Deveaud-Plédran, “The behaviour of exciton–polaritons,” *Nature Photonics*, vol. 6, pp. 205–205, Apr 2012.
- [114] T. Byrnes, N. Y. Kim, and Y. Yamamoto, “Exciton–polariton condensates,” *Nature Physics*, vol. 10, pp. 803–813, Nov 2014.
- [115] J. Toepfer, *Coherent networks of polariton condensates in microcavities*. PhD thesis, University of Southampton, October 2021.
- [116] C. Schneider, K. Winkler, M. D. Fraser, M. Kamp, Y. Yamamoto, E. A. Ostrovskaya, and S. Höfling, “Exciton-polariton trapping and potential landscape engineering,” *Reports on Progress in Physics*, vol. 80, p. 016503, nov 2016.
- [117] G. Roumpos, W. H. Nitsche, S. Höfling, A. Forchel, and Y. Yamamoto, “Gain-induced trapping of microcavity exciton polariton condensates,” *Phys. Rev. Lett.*, vol. 104, p. 126403, Mar 2010.
- [118] N. Y. Kim, K. Kusudo, C. Wu, N. Masumoto, A. Löffler, S. Höfling, N. Kumada, L. Worschech, A. Forchel, and Y. Yamamoto, “Dynamical d-wave condensation of exciton–polaritons in a two-dimensional square-lattice potential,” *Nature Physics*, vol. 7, pp. 681–686, Sep 2011.
- [119] A. Askitopoulos, H. Ohadi, A. V. Kavokin, Z. Hatzopoulos, P. G. Savvidis, and P. G. Lagoudakis, “Polariton condensation in an optically induced two-dimensional potential,” *Phys. Rev. B*, vol. 88, p. 041308, Jul 2013.
- [120] A. Verger, C. Ciuti, and I. Carusotto, “Polariton quantum blockade in a photonic dot,” *Phys. Rev. B*, vol. 73, p. 193306, May 2006.
- [121] A. Askitopoulos, L. Pickup, S. Alyatkin, A. Zasedatelev, K. G. Lagoudakis, W. Langbein, and P. G. Lagoudakis, “Giant increase of temporal coherence in optically trapped polariton condensate,” 2019.
- [122] K. V. Kavokin, I. A. Shelykh, A. V. Kavokin, G. Malpuech, and P. Bigenwald, “Quantum theory of spin dynamics of exciton-polaritons in microcavities,” *Phys. Rev. Lett.*, vol. 92, p. 017401, Jan 2004.
- [123] J.-i. Inoue, T. Brandes, and A. Shimizu, “Renormalized bosonic interaction of excitons,” *Phys. Rev. B*, vol. 61, pp. 2863–2873, Jan 2000.
- [124] M. Vladimirova, S. Cronenberger, D. Scalbert, K. V. Kavokin, A. Miard, A. Lemaître, J. Bloch, D. Solnyshkov, G. Malpuech, and A. V. Kavokin, “Polariton-polariton interaction constants in microcavities,” *Phys. Rev. B*, vol. 82, p. 075301, Aug 2010.

- [125] P. G. Lagoudakis, P. G. Savvidis, J. J. Baumberg, D. M. Whittaker, P. R. Eastham, M. S. Skolnick, and J. S. Roberts, “Stimulated spin dynamics of polaritons in semiconductor microcavities,” *Phys. Rev. B*, vol. 65, p. 161310, Apr 2002.
- [126] A. Kavokin, P. G. Lagoudakis, G. Malpuech, and J. J. Baumberg, “Polarization rotation in parametric scattering of polaritons in semiconductor microcavities,” *Phys. Rev. B*, vol. 67, p. 195321, May 2003.
- [127] P. Cilibrizzi, A. Askitopoulos, M. Silva, F. Bastiman, E. Clarke, J. M. Zajac, W. Langbein, and P. G. Lagoudakis, “Polariton condensation in a strain-compensated planar microcavity with InGaAs quantum wells,” *Applied Physics Letters*, vol. 105, no. 19, p. 191118, 2014.
- [128] P. Cristofolini, A. Dreismann, G. Christmann, G. Franchetti, N. G. Berloff, P. Tsotsis, Z. Hatzopoulos, P. G. Savvidis, and J. J. Baumberg, “Optical superfluid phase transitions and trapping of polariton condensates,” *Phys. Rev. Lett.*, vol. 110, p. 186403, May 2013.
- [129] R. H. Brown and R. Q. Twiss, “Correlation between photons in two coherent beams of light,” *Nature*, vol. 177, pp. 27–29, 1956.
- [130] R. H. Brown and R. Q. Twiss, “A test of a new type of stellar interferometer on sirius,” *Nature*, vol. 178, pp. 1046–1048, 1956.
- [131] A. L. Schawlow and C. H. Townes, “Infrared and optical masers,” *Phys. Rev.*, vol. 112, pp. 1940–1949, Dec 1958.
- [132] L. Mandel, “Fluctuations of photon beams: The distribution of the photo-electrons,” *Proceedings of the Physical Society*, vol. 74, pp. 233–243, sep 1959.
- [133] L. Mandel, “V fluctuations of light beams,” vol. 2 of *Progress in Optics*, pp. 181–248, Elsevier, 1963.
- [134] R. J. Glauber, “The quantum theory of optical coherence,” *Phys. Rev.*, vol. 130, pp. 2529–2539, Jun 1963.
- [135] R. J. Glauber, “Coherent and incoherent states of the radiation field,” *Phys. Rev.*, vol. 131, pp. 2766–2788, Sep 1963.
- [136] M. C. Teich and B. E. Saleh, “I photon bunching and antibunching\*\*this work was supported by the joint services electronics program at columbia university and by the national science foundation.,” vol. 26 of *Progress in Optics*, pp. 1–104, Elsevier, 1988.
- [137] B. Saleh, *Photoelectron Statistics*. Springer Series in Optical Sciences.
- [138] M. Teich and B. Saleh, *Photon Bunching and Antibunching*, vol. XXVI, pp. 1–104. 12 1988.
- [139] L. Mandel, “Fluctuations of photon beams and their correlations,” *Proceedings of the Physical Society*, vol. 72, pp. 1037–1048, dec 1958.

- [140] H. Deng, G. Weihs, C. Santori, J. Bloch, and Y. Yamamoto, “Condensation of semiconductor microcavity exciton polaritons,” *Science*, vol. 298, no. 5591, pp. 199–202, 2002.
- [141] J. Kasprzak, M. Richard, A. Baas, B. Deveaud, R. André, J.-P. Poizat, and L. S. Dang, “Second-order time correlations within a polariton bose-einstein condensate in a cdte microcavity,” *Phys. Rev. Lett.*, vol. 100, p. 067402, Feb 2008.
- [142] M. Aßmann, F. Veit, J.-S. Tempel, T. Berstermann, H. Stolz, M. van der Poel, J. M. Hvam, and M. Bayer, “Measuring the dynamics of second-order photon correlation functions inside a pulse with picosecond time resolution,” *Opt. Express*, vol. 18, pp. 20229–20241, Sep 2010.
- [143] P. Loudon and R. Loudon, *The Quantum Theory of Light*. Oxford science publications, Clarendon Press, 1983.
- [144] C. E. Whittaker, B. Dzurak, O. A. Egorov, G. Buonaiuto, P. M. Walker, E. Cancellieri, D. M. Whittaker, E. Clarke, S. S. Gavrilov, M. S. Skolnick, and D. N. Krizhanovskii, “Polariton pattern formation and photon statistics of the associated emission,” *Phys. Rev. X*, vol. 7, p. 031033, Aug 2017.
- [145] A. Delteil, T. Fink, A. Schade, S. Höfling, C. Schneider, and A. İmamoglu, “Towards polariton blockade of confined exciton–polaritons,” *Nature Materials*, vol. 18, pp. 219–222, Mar 2019.
- [146] G. Muñoz-Matutano, A. Wood, M. Johnsson, X. Vidal, B. Q. Baragiola, A. Reinhard, A. Lemaître, J. Bloch, A. Amo, G. Nogues, B. Besga, M. Richard, and T. Volz, “Emergence of quantum correlations from interacting fibre-cavity polaritons,” *Nature Materials*, vol. 18, pp. 213–218, Mar 2019.
- [147] A. F. Adiyatullin, M. D. Anderson, P. V. Busi, H. Abbaspour, R. André, M. T. Portella-Oberli, and B. Deveaud, “Temporally resolved second-order photon correlations of exciton-polariton Bose-Einstein condensate formation,” *Applied Physics Letters*, vol. 107, no. 22, p. 221107, 2015.
- [148] I. A. Shelykh, Y. G. Rubo, G. Malpuech, D. D. Solnyshkov, and A. Kavokin, “Polarization and propagation of polariton condensates,” *Phys. Rev. Lett.*, vol. 97, p. 066402, Aug 2006.
- [149] J. J. Baumberg, A. V. Kavokin, S. Christopoulos, A. J. D. Grundy, R. Butté, G. Christmann, D. D. Solnyshkov, G. Malpuech, G. Baldassarri Höger von Högersthal, E. Feltn, J.-F. Carlin, and N. Grandjean, “Spontaneous polarization buildup in a room-temperature polariton laser,” *Phys. Rev. Lett.*, vol. 101, p. 136409, Sep 2008.
- [150] D. D. Solnyshkov, I. A. Shelykh, M. M. Glazov, G. Malpuech, T. Amand, P. Renucci, X. Marie, and A. V. Kavokin, “Nonlinear effects in spin relaxation of cavity polaritons,” *Semiconductors*, vol. 41, pp. 1080–1091, Sep 2007.

- [151] Ł. Kłopotowski, M. Martín, A. Amo, L. Viña, I. Shelykh, M. Glazov, G. Malpuech, A. Kavokin, and R. André, “Optical anisotropy and pinning of the linear polarization of light in semiconductor microcavities,” *Solid State Communications*, vol. 139, no. 10, pp. 511 – 515, 2006.
- [152] J. Kasprzak, R. André, L. S. Dang, I. A. Shelykh, A. V. Kavokin, Y. G. Rubo, K. V. Kavokin, and G. Malpuech, “Build up and pinning of linear polarization in the Bose condensates of exciton polaritons,” *Phys. Rev. B*, vol. 75, p. 045326, Jan 2007.
- [153] H. Sigurdsson, “Hysteresis in linearly polarized nonresonantly driven exciton-polariton condensates,” *Phys. Rev. Research*, vol. 2, p. 023323, Jun 2020.
- [154] M. Wouters and V. Savona, “Stochastic classical field model for polariton condensates,” *Phys. Rev. B*, vol. 79, p. 165302, Apr 2009.
- [155] H. J. Carmichael, *Statistical methods in quantum optics 1: master equations and Fokker-Planck equations*. Springer Science & Business Media, 2013.
- [156] D. Witthaut, F. Trimborn, H. Hennig, G. Kordas, T. Geisel, and S. Wimberger, “Beyond mean-field dynamics in open Bose-Hubbard chains,” *Phys. Rev. A*, vol. 83, p. 063608, Jun 2011.
- [157] C. Antón, S. Morina, T. Gao, P. S. Eldridge, T. C. H. Liew, M. D. Martín, Z. Hatzopoulos, P. G. Savvidis, I. A. Shelykh, and L. Viña, “Optical control of spin textures in quasi-one-dimensional polariton condensates,” *Phys. Rev. B*, vol. 91, p. 075305, Feb 2015.
- [158] A. Askitopoulos, K. Kalinin, T. C. H. Liew, P. Cilibrizzi, Z. Hatzopoulos, P. G. Savvidis, N. G. Berloff, and P. G. Lagoudakis, “Nonresonant optical control of a spinor polariton condensate,” *Phys. Rev. B*, vol. 93, p. 205307, May 2016.
- [159] M. D. Martín, G. Aichmayr, L. Viña, and R. André, “Polarization control of the nonlinear emission of semiconductor microcavities,” *Phys. Rev. Lett.*, vol. 89, p. 077402, Jul 2002.
- [160] I. Shelykh, G. Malpuech, K. V. Kavokin, A. V. Kavokin, and P. Bigenwald, “Spin dynamics of interacting exciton polaritons in microcavities,” *Phys. Rev. B*, vol. 70, p. 115301, Sep 2004.
- [161] D. N. Krizhanovskii, D. Sanvitto, I. A. Shelykh, M. M. Glazov, G. Malpuech, D. D. Solnyshkov, A. Kavokin, S. Ceccarelli, M. S. Skolnick, and J. S. Roberts, “Rotation of the plane of polarization of light in a semiconductor microcavity,” *Phys. Rev. B*, vol. 73, p. 073303, Feb 2006.
- [162] I. I. Ryzhov, V. O. Kozlov, N. S. Kuznetsov, I. Y. Chestnov, A. V. Kavokin, A. Tzimis, Z. Hatzopoulos, P. G. Savvidis, G. G. Kozlov, and V. S. Zapasskii, “Spin noise signatures of the self-induced Larmor precession,” *Phys. Rev. Research*, vol. 2, p. 022064, Jun 2020.

- [163] A. Askitopoulos, H. Sigurdsson, I. Gnusov, S. Alyatkin, L. Pickup, N. A. Gippius, and P. G. Lagoudakis, “Coherence revivals of a spinor polariton condensate from self-induced Larmor precession,” 2020.
- [164] Y. del Valle-Inclan Redondo, H. Sigurdsson, H. Ohadi, I. A. Shelykh, Y. G. Rubo, Z. Hatzopoulos, P. G. Savvidis, and J. J. Baumberg, “Observation of inversion, hysteresis, and collapse of spin in optically trapped polariton condensates,” *Phys. Rev. B*, vol. 99, p. 165311, Apr 2019.
- [165] E. del Valle Reboul, *Microcavity Quantum Electrodynamics*. Springer Series in Optical Sciences, Saarbrücken VDM Verlag Dr. Muller 2010, 2010.
- [166] Y. del Valle-Inclan Redondo, H. Ohadi, Y. G. Rubo, O. Beer, A. J. Ramsay, S. I. Tsintzos, Z. Hatzopoulos, P. G. Savvidis, and J. J. Baumberg, “Stochastic spin flips in polariton condensates: nonlinear tuning from GHz to sub-hz,” *New Journal of Physics*, vol. 20, p. 075008, jul 2018.
- [167] M. Boozarjmehr, M. Steger, K. West, L. N. Pfeiffer, D. W. Snoke, A. G. Truscott, E. A. Ostrovskaya, and M. Pieczarka, “Spatial distribution of an optically induced excitonic reservoir below exciton-polariton condensation threshold,” 2019.
- [168] C. Ciuti, V. Savona, C. Piermarocchi, A. Quattropani, and P. Schwendimann, “Role of the exchange of carriers in elastic exciton-exciton scattering in quantum wells,” *Phys. Rev. B*, vol. 58, pp. 7926–7933, Sep 1998.
- [169] M. Z. Maialle, E. A. de Andrada e Silva, and L. J. Sham, “Exciton spin dynamics in quantum wells,” *Phys. Rev. B*, vol. 47, pp. 15776–15788, Jun 1993.
- [170] L. Viña, “Spin relaxation in low-dimensional systems,” *Journal of Physics: Condensed Matter*, vol. 11, pp. 5929–5952, jul 1999.
- [171] M. Klaas, O. A. Egorov, T. C. H. Liew, A. Nalitov, V. Marković, H. Suchomel, T. H. Harder, S. Betzold, E. A. Ostrovskaya, A. Kavokin, S. Klembt, S. Höfling, and C. Schneider, “Nonresonant spin selection methods and polarization control in exciton-polariton condensates,” *Phys. Rev. B*, vol. 99, p. 115303, Mar 2019.
- [172] L. Pickup, J. D. Töpfer, H. Sigurdsson, and P. G. Lagoudakis, “Polariton spin jets through optical control,” *Phys. Rev. B*, vol. 103, p. 155302, Apr 2021.
- [173] M. Maragkou, C. E. Richards, T. Ostatnický, A. J. D. Grundy, J. Zajac, M. Hugues, W. Langbein, and P. G. Lagoudakis, “Optical analogue of the spin hall effect in a photonic cavity,” *Opt. Lett.*, vol. 36, pp. 1095–1097, Apr 2011.
- [174] D. M. Whittaker and P. R. Eastham, “Coherence properties of the microcavity polariton condensate,” *EPL (Europhysics Letters)*, vol. 87, p. 27002, jul 2009.
- [175] A. P. D. Love, D. N. Krizhanovskii, D. M. Whittaker, R. Bouchekioua, D. Sanvitto, S. A. Rizeiqi, R. Bradley, M. S. Skolnick, P. R. Eastham, R. André, and L. S. Dang, “Intrinsic decoherence mechanisms in the microcavity polariton condensate,” *Phys. Rev. Lett.*, vol. 101, p. 067404, Aug 2008.

- [176] S. Prasad, M. O. Scully, and W. Martienssen, “A quantum description of the beam splitter,” *Optics Communications*, vol. 62, no. 3, pp. 139–145, 1987.
- [177] Z. Ou, C. Hong, and L. Mandel, “Relation between input and output states for a beam splitter,” *Optics Communications*, vol. 63, no. 2, pp. 118–122, 1987.
- [178] H. Fearn and R. Loudon, “Quantum theory of the lossless beam splitter,” *Optics Communications*, vol. 64, no. 6, pp. 485–490, 1987.
- [179] C. K. Hong, Z. Y. Ou, and L. Mandel, “Measurement of subpicosecond time intervals between two photons by interference,” *Phys. Rev. Lett.*, vol. 59, pp. 2044–2046, Nov 1987.
- [180] E. Moschandreou, J. I. Garcia, B. J. Rollick, B. Qi, R. Pooser, and G. Siopsis, “Experimental study of hong–ou–mandel interference using independent phase randomized weak coherent states,” *J. Lightwave Technol.*, vol. 36, pp. 3752–3759, Sep 2018.
- [181] H. Paul, “Interference between independent photons,” *Rev. Mod. Phys.*, vol. 58, pp. 209–231, Jan 1986.
- [182] Y.-S. Kim, O. Slattery, P. S. Kuo, and X. Tang, “Two-photon interference with continuous-wave multi-mode coherent light,” *Opt. Express*, vol. 22, pp. 3611–3620, Feb 2014.
- [183] J. Liu, D. Wei, H. Chen, Y. Zhou, H. Zheng, H. Gao, F.-L. Li, and Z. Xu, “Second-order interference of two independent and tunable single-mode continuous-wave lasers,” *Chinese Physics B*, vol. 25, p. 034203, mar 2016.
- [184] H. Kim, O. Kwon, and H. S. Moon, “Time-resolved two-photon interference of weak coherent pulses,” *Applied Physics Letters*, vol. 118, p. 244001, jun 2021.
- [185] H. Kim, D. Kim, J. Park, and H. S. Moon, “Hong–ou–mandel interference of two independent continuous-wave coherent photons,” *Photon. Res.*, vol. 8, pp. 1491–1495, Sep 2020.
- [186] J. Liu, M. Le, B. Bai, W. Wang, H. Chen, Y. Zhou, F. li Li, and Z. Xu, “The second-order interference of two independent single-mode he–ne lasers,” *Optics Communications*, vol. 350, pp. 196–201, 2015.
- [187] C. Agnesi, B. D. Lio, D. Cozzolino, L. Cardi, B. B. Bakir, K. Hassan, A. D. Frera, A. Ruggeri, A. Giudice, G. Vallone, P. Villoresi, A. Tosi, K. Rottwitt, Y. Ding, and D. Bacco, “Hong–ou–mandel interference between independent iii–v on silicon waveguide integrated lasers,” *Opt. Lett.*, vol. 44, pp. 271–274, Jan 2019.
- [188] Z. L. Yuan, M. Lucamarini, J. F. Dynes, B. Fröhlich, M. B. Ward, and A. J. Shields, “Interference of short optical pulses from independent gain-switched laser diodes for quantum secure communications,” *Phys. Rev. Applied*, vol. 2, p. 064006, Dec 2014.
- [189] H.-K. Lo, M. Curty, and B. Qi, “Measurement-device-independent quantum key distribution,” *Phys. Rev. Lett.*, vol. 108, p. 130503, Mar 2012.

- [190] J. Liu, Y. Zhou, F. li Li, and Z. Xu, “The second-order interference between laser and thermal light,” *EPL (Europhysics Letters)*, vol. 105, p. 64007, mar 2014.
- [191] J. Liu, H. Zheng, H. Chen, Y. Zhou, F. li Li, and Z. Xu, “The first- and second-order temporal interference between thermal and laser light,” *Opt. Express*, vol. 23, pp. 11868–11878, May 2015.
- [192] J. Kasprzak, R. André, L. S. Dang, I. A. Shelykh, A. V. Kavokin, Y. G. Rubo, K. V. Kavokin, and G. Malpuech, “Build up and pinning of linear polarization in the bose condensates of exciton polaritons,” *Phys. Rev. B*, vol. 75, p. 045326, Jan 2007.
- [193] E. D. Cherotchenko, H. Sigurdsson, A. Askitopoulos, and A. V. Nalitov, “Optically controlled polariton condensate molecules,” *Phys. Rev. B*, vol. 103, p. 115309, Mar 2021.
- [194] S. Agne, J. Jin, K. B. Kuntz, F. M. Miatto, J.-P. Bourgoïn, and T. Jennewein, “Hong-ou-mandel interference of unconventional temporal laser modes,” *Opt. Express*, vol. 28, pp. 20943–20953, Jul 2020.
- [195] J. D. Töpfer, H. Sigurdsson, S. Alyatkin, and P. G. Lagoudakis, “Lotka-volterra population dynamics in coherent and tunable oscillators of trapped polariton condensates,” *Phys. Rev. B*, vol. 102, p. 195428, Nov 2020.
- [196] S. L. Harrison, H. Sigurdsson, and P. G. Lagoudakis, “Synchronization in optically trapped polariton stuart-landau networks,” *Phys. Rev. B*, vol. 101, p. 155402, Apr 2020.